NUREG/CR-6195
TMI V(92)EG10
EGG-2732

Examination of Relocated Fuel Debris Adjacent to the Lower Head of the TMI-2 Reactor Vessel

Manuscript Completed: February 1994
Date Published: March 1994

Prepared by
D. W. Akers, S. M. Jensen, B. K. Schuetz

Idaho National Engineering Laboratory
Managed by the U.S. Department of Energy

EG&G Idaho, Inc.
Idaho Falls, ID 83415

Prepared for
Division of Systems Research
Office of Nuclear Regulatory Research
U.S. Nuclear Regulatory Commission
Washington, DC 20555-0001
NRC FIN L1004
Under DOE Contract No. DE-AC07-76ID01570

ABSTRACT

As part of the Three Mile Island Unit 2 (TMI-2) Vessel Investigation Project, funded by the Organization for Economic Cooperation and Development, physical, metallurgical, and radiochemical examinations were performed on samples of previously molten material that had relocated to the lower plenum of the TMI-2 reactor during the accident of 28 March 1979. This report presents the results of those examinations and some limited analysis of these results as required for the interpretation of the data. Principal conclusions of the examinations are that the bulk lower head debris is homogeneous and composed primarily of $(U,Zr)O_2$. This molten material reached temperatures greater than 2,600°C and probably reached the lower head as a liquid or slurry at temperatures below the peak temperature. A debris bed was formed, which was composed of particulate debris above a monolithic melt that solidified on the lower head.

CONTENTS

LIST OF FIGURES

LIST OF TABLES

EXECUTIVE SUMMARY

As part of the Three Mile Island Unit 2 (TMI-2) Vessel Investigation Project (VIP), examinations of samples of fuel debris from near the lower head of the reactor vessel have been performed to (a) assess the physical, metallurgical, and radiochemical properties of the materials that were in contact with the lower vessel head (i.e., companion samples), (b) assess the potential for interactions between the molten core material and the lower head, and (c) provide information needed to develop models to assess the margin to failure of the lower head. A complete analysis and interpretation of the companion sample examination results will be reported in the VIP integration report.

Nondestructive examinations of the companion samples included visual examination, photography, sample weight, bulk sample density, and individual particle density. Bulk sample densities were similar and ranged from 8.2 to 9.4 g/cm^3. The measured porosities were quite variable for individual samples (5.7–32%), but the average porosity was 18 ± 11%. Comparisons between the bulk composition and theoretical densities indicate that a relatively accurate, accurate porosity value was obtained.

All samples consisted primarily of previously molten $(U,Zr)O_2$. The pores in some samples formed in stratified layers and were surrounded by microporosity and two-phase structures consisting of $(U,Zr)O_2$ and $(Zr,U)O_2$. It has been suggested that the stratified layers were actually gas bubbles (steam or metal vapors) that froze in place as the bubbles rose through the cooling core material.

The presence of two-phase $(U,Zr)O_2$ and $(Zr,U)O_2$ structures indicates that these samples were not rapidly quenched, but underwent a gradual cooldown. The propensity for these two-phase regions to exist around pores is also an indication that these were the last areas to solidify and that the single-phase regions solidified first. The microstructure is indicative of a solidified $(U,Zr)O_2$ ceramic melt, which had an overall composition rich in uranium. Also, the examinations indicate that the companion samples were fully oxidized, which suggests the presence of sufficient steam to oxidize all available zirconium.

The bulk elemental composition data for the companion samples indicate that the debris bed is homogeneous and that it is composed primarily of fuel element components with relatively small amounts of other structural components. The elemental analysis results indicate that the debris was composed of about 70 wt% U, 13.75 wt% Zr, and 13 wt% O. This composition accounts for about 97 wt% of the debris. The elemental constituents of the stainless steel and inconel core components make up the remaining 3 wt%.

The radiochemical examinations indicate that much of the volatile radionuclide content of the debris (noble gases, cesium, and iodine) had volatilized out of the molten fuel, leaving the medium- and low-volatile radionuclides in the debris bed. Decay heat calculations were performed to determine the amount of available heat present in the debris bed during the relocation event (224 minutes after reactor shutdown) and at 600 minutes. These calculations indicate that the available heat was about 0.13 watts/g of debris at 224 minutes and 0.096 watts/g of debris at 600 minutes. These data indicate a relatively constant source of heat available to maintain the debris bed in a molten condition.

Comparisons with examinations of the loose debris layer (DOE Accident Evaluation Program) above the companion samples indicate that the loose debris layer has a slightly lower average uranium content (~65 wt%), is more porous, and contains higher concentrations of iron, chromium, and other constituents of stainless steel and inconel than do the companion samples. The examination results presented in this report will be subjected to further analysis and interpretation in the VIP integration report.

FOREWORD

The contents of this report were developed as part of the Three Mile Island Unit 2 Vessel Investigation Project. This project is jointly sponsored by eleven countries under the auspices of the Nuclear Energy Agency of the Organization for Economic Cooperation and Development. The twelve sponsoring organizations are:

* The Centre d'Etudes d'Energie Nucléaires of Belgium,
* The Säteilyturvakeskus of Finland,
* The Institute de Protection et de Sûreté Nucléaire of the Commissariat à l'Energie Atomique of France,
* The Gesellschaft für Reaktorsicherheit mbH of Germany,
* The Comitato Nazionale per La Ricerca e per Lo Sviluppo Dell' Energia Nucleare e Delle Energie Alternative of Italy,
* The Japan Atomic Energy Research Institute,
* The Consejo de Seguridad Nuclear of Spain,
* The Statens Kärnkraftinspektion of Sweden,
* The Office Fédéral de l'Energie of Switzerland,
* AEA Technology of the United Kingdom,
* The United States Nuclear Regulatory Commission, and
* The Electric Power Research Institute.

The primary objectives of the Nuclear Energy Agency (NEA) are to promote cooperation between its Member governments on the safety and regulatory aspects of nuclear development, and on assessing the future role of nuclear energy as a contributor to economic progress.

This is achieved by:

- encouraging harmonisation of governments' regulatory policies and practices in the nuclear field, with particular reference to the safety of nuclear installations, protection of man against ionising radiation and preservation of the environment, radioactive waste management, and nuclear third party liability and insurance;

- keeping under review the technical and economic characteristics of nuclear power growth and of the nuclear fuel cycle, and assessing demand and supply for the different phases of the nuclear fuel cycle and the potential future contribution of nuclear power to overall energy demand;

- developing exchanges of scientific and technical information on nuclear energy, particularly through participation in common services;

- setting up international research and development programmes and undertakings jointly organized and operated by OECD countries.

In these and related tasks, NEA works in close collaboration with the International Atomic Energy Agency in Vienna, with which it has concluded a Cooperation Agreement, as well as with other international organizations in the nuclear field.

Examination of Relocated Fuel Debris Adjacent to the Lower Head of the TMI-2 Reactor Vessel

1. INTRODUCTION

The accident at the Three Mile Island Unit 2 (TMI-2) reactor resulted in the relocation of about 19,000 kg of molten core material to the lower head of the reactor vessel. This relocation occurred at about 224 minutes after the reactor scrammed and lasted for about 2 minutes. Extensive video examinations of the lower plenum were conducted in 1985[1] and again during the core bore operations in 1986[2] to assess the extent of damage to the lower head. However, before core boring was begun, samples of fuel debris were removed from the surface of the debris on the lower head.[3] These debris samples, which had not been contaminated with debris from the upper part of the reactor core, were examined under the auspices of the U.S. Department of Energy (DOE) Accident Evaluation Program, sponsored by the General Public Utilities Nuclear Corporation (owner/operator of TMI), the Electric Power Research Institute, and the U.S. Nuclear Regulatory Commission (NRC). At the conclusion of this program, the Organization for Economic Cooperation and Development (OECD) TMI-2 Vessel Investigation Project (VIP) was begun to assess the damage to the lower head of the reactor vessel and to develop an understanding of the potential for failure of the lower head. Lower head sample examinations were focused on two areas: companion debris samples from locations adjacent to the lower head, and nozzle and guide tube samples from the vessel and the flow distributor, respectively.

As part of the VIP, examinations of companion samples were performed to (a) assess the physical, metallurgical, and radiochemical properties of the debris adjacent to the lower vessel head, (b) assess the potential for interactions between the molten core materials and the lower head, and (c) provide information needed to develop models to assess the margin to failure of the lower head of the TMI-2 reactor vessel.

This report presents results of the physical, metallurgical, and radiochemical examinations performed on the companion samples and limited analysis of these results as required for the interpretation of the data. Section 2 of this report describes how the companion samples were acquired from the lower head of the reactor vessel, their approximate locations in the debris bed,

and sample designations. The results of the nondestructive companion sample examinations (visual examinations, photo-documentation, density, and porosity) are presented in Section 3, and the results of the destructive examinations [optical metallography, scanning electron microscopy (SEM), and radiochemical analyses] are presented in Section 4. Section 5 presents comparisons with the DOE lower head debris analyses, Section 6 discusses the specific data requirements for the lower head failure analysis, and the summary and conclusions of this work are presented in Section 7.

2. SAMPLE ACQUISITION

From initial probing examinations performed on 15 February 1989,[4] the distribution of loose debris on the lower head was determined (see Figure 1). Following these probing examinations, core boring of the upper core was performed. This activity deposited additional loose debris on the lower head. All loose debris was then removed from the lower head, revealing a variable topography of solidified debris (the companion material) on the lower head, with depths ranging from less than 5 cm up to 45 cm in the southwest quadrant (see Figure 2). The locations with the greatest depth (i.e., ~45 cm) were H9, H10, I9, and I10 in the central part of the lower head, as indicated by General Public Utilities defueling data. Outside of this central region (75–85 cm from the periphery of the core), the solidified debris was up to 26 cm deep. Consequently, the companion samples came from within 30 cm of the lower head for all samples and may have come from within 15 cm if obtained from near the periphery of the molten pool.

The solidified layer was broken up by a 300-lb (136-kg) slide hammer, which was dropped from an elevation of 20 ft (6.1 m). The resulting debris appeared to be homogeneous; no obvious metallic layer was present.

Bulk companion samples were acquired from the southeast, southwest, and northeast quadrants of the reactor vessel (see Figure 3). Most examination work has focused on these samples, which appear to be representative of the debris bed. Almost no debris was obtained, however, from the northwest quadrant of the reactor vessel because once the loose debris was removed from this part of the lower head, little attached debris remained. In fact, defueling equipment (a large clamshell) was able to recover only very small amounts of debris. Because the northwest sample is small and may not be representative of the debris bed, observations based on this sample are questionable.

3. NONDESTRUCTIVE EXAMINATIONS

Nondestructive examinations of the lower plenum samples included visual examinations, photography, sample weights, bulk density, and individual particle density. Figures 4 through 7 show the bulk companion samples from which individual particles were selected for examination. All companion samples were composed of large pieces of broken-up debris except companion sample 1-10 from the northwest quadrant. This sample was composed of fine particulate debris and was not considered to be representative of the companion sample material. It was probably a mixture of loose debris and material that was deposited on the lower head during the core boring operations discussed in Section 2.

Density measurements were performed on both companion samples and individual particles using the standard immersion method. Table 1 lists the location, the total weight, and the density of each companion sample. The companion sample with the highest density (9.4 g/cm^3) was from the southeast quadrant. The low density of the sample taken from the northwest quadrant was excluded from the average density (8.7 g/cm^3) of the debris bed due to the small sample size. The densities of the two remaining companion samples were 8.2 and 8.6 g/cm^3. Examination of the elemental analysis results, to be discussed, indicates that the composition of all samples is similar. This indicates that the differences in density are primarily due to differences in the porosity of the debris bed.

Representative photographs of selected individual particle samples are shown in Figures 8 through 13. Visual examinations indicate that the rocks were composed primarily of previously molten ceramic material, and possibly included small amounts of metallic material (as suggested by the bright areas in the photographs). The samples were generally dull grey in appearance, although some areas were yellow (lighter areas in photographs).

Table 2 shows the weight and density of each individual particle sample. Densities ranged from 7.45 to 9.40 g/cm^3, which is consistent with samples composed primarily of $(U,Zr)O_2$ with a large proportion of UO_2 and varying amounts of porosity. The densities of intact UO_2 pellets and ZrO_2 are about 10.4 and 5.6 g/cm^3, respectively. The average density of the debris bed is assessed in Section 6.

Table 1. TMI-2 bulk sample weights and densities.

Sample Number	Location (quadrant)	Weight (g)	Density (g/cm^3)
1-9	Southeast	2436	9.4
1-10	Northwest	0.50	6.9
1-11	Southwest	1214	8.6
1-12	Northeast	2700	8.2

Table 2. TMI-2 lower plenum individual sample weights and densities.

Sample	Weight (g)	Density (g/cm^3)
1-9	51.81	9.40
1-9-F	14.90	7.45
1-9-G	12.10	8.07
1-11	52.23	8.62
1-11-C	49.50	8.39
1-11-D	76.40	8.30
1-12	47.16	8.18
1-12-C	45.50	9.29
1-12-D	15.20	7.60

Table 3 lists porosity data for individual particle samples from the three quadrants of the lower head where most of the debris was obtained. The porosity was determined using optical methods on polished metallographic specimens. The approximate average porosities of samples from the southeast (sample 1-9), southwest (sample 1-11), and northeast (sample 1-12) quadrants are 20.8 ± 7%, 18 ± 14%, and 17 ± 9%, respectively. However, these data can be quite misleading and biased due to several high values and the range of porosities observed. The overall porosity of all samples is 18 ± 11%, which suggests a very broad range of porosities in the debris. Additional samples would have to be analyzed to improve this estimate. Further analysis of the average porosity of the debris bed and the effect on the density of the bulk debris is presented in Section 5. Also, these results are compared with the porosity and density results for the samples obtained from the surface of the debris bed that were acquired as part of the DOE Accident Evaluation Program.

Table 3. TMI-2 lower plenum sample porosities.

Sample	Figure Number	Porosity (%)	Remarks
1-9-A	Figure 29	29.2	Holes/cracks
1-9-B1	Figure 30	10.8	Holes/cracks
1-9-B2	Figure 31	19.5	Holes/cracks
1-9-F	Figure 33	27.0	Holes/halftone[a]
1-9-G	Figure 34	17.3	Original macro
1-11-C	Figure 47	7.6	Holes/halftone
1-11-D-A	Figure 48	20.5	Original photo
1-11-L	Figure 45	21	Fine holes not resolved
1-11-T	Figure 19	7.0	Low magnification (halftone)
1-11-T	Figure 46	5.7	Large holes only
1-11-D-B	Figure 49	47.5	Mottled stringers not included
1-12	Figure 20	9.5	Low magnification (halftone)
1-12	Figure 51	19.8	Halftone
1-12	Figure 51	22.0	Original photo
1-12-C	Figure 52	5.7	Stringers
1-12-D	Figure 53	31.7	Original photo

a. Halftones are report-quality photographs that may not contain the level of detail of the original photographs. Some smaller porosity may not be apparent from the optical analysis. Comparisons indicate that the difference in porosity between halftones and originals is 1-2%.

4. DESTRUCTIVE EXAMINATIONS

Eleven individual particle samples from the lower plenum were selected for destructive examinations. The examinations that were performed included optical metallography, SEM (scanning electron microscopy) analysis with EDX (energy dispersive x-ray) and WDS (wavelength dispersive x-ray) analysis, bulk elemental analysis, and radionuclide content. The companion samples were sectioned so that specific faces could be examined. Also, some samples were broken into pieces during handling in the hot cells. Consequently, a total of 14 surfaces were actually examined. The samples were placed into two large mounts (12.5 cm in diameter), epoxy was added, and the samples were polished for metallographic examination. Five of the 11 samples were from the primary relocation pathway in the southeast quadrant of the reactor (samples 1-9-A, 1-9-B, 1-9-C, 1-9-F, and 1-9-G). Three samples were from the principal damage region in the southwest quadrant of the reactor (samples 1-11, 1-11-C, and 1-11-D), and the remaining three samples were from the northeast quadrant of the reactor vessel head (samples 1-12, 1-12-C, and 1-12-D). These samples were sectioned and prepared for metallographic examination, after which representative samples were obtained for SEM/microprobe examinations and radiochemical analysis.

4.1 Metallurgical Examinations

Figure 14 shows the first epoxied and polished mount. Sample 1-9-B was broken in half during handling, and the two pieces were subsequently designated 1-9-B1 and 1-9-B2. Sample 1-11 was sectioned to provide longitudinal and transverse cross-sectional views through the rock, and these were designated 1-11-L and 1-11-T. Higher magnification photographs of each of the polished sample surfaces are shown in Figures 15 through 20. Figures 18 and 19 show two views of sample 1-11. In Figure 18, there is evidence of striation or interconnected porosity in the debris, whereas in Figure 19, the porosity is circular and more uniform. Interconnected porosity is present in most samples (e.g., Figure 20) and may be due to bubbling of steam or structural material vapors through the molten pool. The presence of this interconnected porosity in the companion samples suggests that the debris was liquid while on the lower head and that it remained liquid for a sufficient period of time to allow bubble formation.

Figure 21 shows the second epoxied and polished mount. Sample 1-11-D-A was broken into two pieces after sectioning. Higher magnification photographs of each of the polished sample

surfaces are shown in Figures 22 through 28. The metallic objects in the mount were used simply to assist in identifying samples and for orientation during metallographic examinations.

Based on the initial metallographic examinations, all samples appear to consist primarily of previously molten $(U,Zr)O_2$. Droplets of metallic melt were found only in samples 1-11-L, 1-11-T, and 1-11-D-A. The pores in some of the samples were formed in stratified layers and were surrounded by microporosity and two-phase structures consisting of $(U,Zr)O_2$ and $(Zr,U)O_2$. This two-phase morphology suggests that these samples were gradually cooled and not quenched. Details of sample examinations are described below in Section 4.2.

4.2 Sample Examinations by Quadrant

4.2.1 Samples from the Southeast Quadrant (Sample 1-9)

Figures 29 through 34 are photocomposites of the typical microstructures through samples 1-9-A, 1-9-B1, 1-9-B2, 1-9-C, 1-9-F, and 1-9-G. Figure 35 is a higher magnification photograph that shows the typical microstructure in the light and dark areas in the photomosaics. It shows that the darker areas in the photomosaics are composed of microporosity and a secondary phase (grey areas), which are different from the clear single-phase regions (white areas). Stratified layers of pores surrounded by microporosity and the secondary phase material were present in samples 1-9-A, 1-9-B1, and 1-9-B2. The morphology of the material surrounding the pores was discernable only on the scanning electron microscope, and Figures 36 and 37 show that this material was actually composed of two phases, a light, uranium-rich $(U,Zr)O_2$ phase and a dark, zirconium-rich $(Zr,U)O_2$ phase. Away from the porous regions, the single-phase regions consisted of uranium-rich $(U,Zr)O_2$, as shown in Figures 38 through 42. Sample 1-9-C was primarily the single-phase $(U,Zr)O_2$ structure with only minor amounts of two-phase material along some of the cracks and some of the pores. Regions of very porous melt structure were present in some of these samples, as shown in greater detail in Figure 43.

The presence of two-phase $(U,Zr)O_2$ and $(Zr,U)O_2$ structures indicates that these samples were not rapidly quenched, but underwent a gradual cooldown. As shown in the UO_2-ZrO_2 pseudobinary phase diagram in Figure 44, these two-phase structures could have formed only if the samples were cooled slowly through the two-phase region shown on the phase diagram.

4.2.2 Samples from the Southwest Quadrant (Sample 1-11)

Figures 45 through 49 are photocomposites of the typical microstructures observed in the samples from the southwest quadrant. These samples were composed primarily of previously molten $(U,Zr)O_2$, and the basic microstructures were very similar to those found in other regions of the lower plenum; however, small differences were found. Small amounts of metallic melt were found in samples 1-11-L, 1-11-T, and 1-11-D-A; no metallic melts were found in any of the other samples. These metallic melts and the surrounding microstructure are shown in more detail in Figure 50. SEM/microprobe examinations indicate that these melts are silver and indium. A secondary ceramic phase was also present within the $(U,Zr)O_2$ matrix of sample 1-11-T (see Figure 46). SEM/microprobe examinations of this ceramic phase indicate that it was composed primarily of Cr-oxide.

4.2.3 Samples from the Northeast Quadrant (Sample 1-12)

Figures 51 through 53 are photocomposites of typical microstructures in samples from the northeast quadrant. They all show predominantly single-phase $(U,Zr)O_2$ with relatively small amounts of two-phase material and associated microporosity. The overall porosity in these samples varied from little porosity (sample 1-12-C) to medium porosity (sample 1-12) to high porosity (sample 1-12-D).

4.3 Scanning Electron Microscopy Analysis

In-depth SEM analyses were performed to characterize the composition of companion samples 1-11-T, 1-9-A, and 1-9-B, which appeared to be representative of the debris bed. EDX analyses were performed and WDX dot maps were developed to assess the composition of specific phases within the samples. Dot maps were generated for the following core constituents: U, O, Zr, Ag, Al, Cd, Cr, Fe, In, Mg, Mn, Mo, Nb, Ni, Sn, and some fission products. Appendix A presents a discussion of the regions examined and shows dot maps of the elements for which significant results were obtained.

Regions of interest that were examined include the edge of large pores, metallic inclusions, secondary phases, and pores without secondary phases. As previously discussed, each sample is composed of a homogeneous $(U,Zr)O_2$ matrix with relatively low concentrations of Al, Mg, Sb,

and Sn and a zirconium-rich secondary phase around pores and at grain boundaries. In addition, the dot maps in Appendix A indicate the presence of oxidized Fe and Cr inclusions in each matrix. These results suggest that the Fe and Cr are probably the remains of nozzle and other vessel components that were melted during the relocation event.

The metallic inclusions in the 1-11 samples are composed primarily of metallic silver with trace amounts of Zr and other metals. The other constituents of the control rods (In and Cd) are not present, which suggests that the control rod material had been heated sufficiently to volatilize the more volatile In and Cd from the Ag.

Examination of the secondary phases around pores and in the matrix of the debris indicates that the secondary phases are composed primarily of $(Zr,U)O_2$ with greater amounts of Fe and Cr present. The fact that there was time during the cooling process for the lower temperature $(Zr,U)O_2$ phase to form, as discussed in the previous section, suggests that the molten pool remained at a relatively high temperature for a period of time. However, the presence of the localized concentrations of Fe and Cr, probably from the nozzle and guide tube material, suggests that there was not a great deal of mixing after the material was deposited on the lower head. The period of time that the melt remained at high temperatures and the extent of mixing is discussed in Section 6. Also, information from the nozzle and guide tube examinations should provide more information on the period of time that the debris stayed at high temperatures.

4.4 Radiochemical Analyses

Radiochemical analyses were performed on the companion samples to assess bulk composition and radionuclide content. Prior to the destructive analysis, the intact samples were analyzed via gamma spectroscopy to provide an initial estimate of the gamma-emitting radionuclide content. Then, the samples were dissolved using a pyrosulfate fusion technique in a closed system. Iodine-129 tracer was added to the intact sample before dissolution, and ^{90}Sr was added after dissolution. This technique was used to allow measurement of the ^{129}I content of the samples to be performed. A description of the analysis methods used for the companion sample examinations is presented in Reference 5.

Elemental analyses were performed on dissolved samples using inductively coupled plasma spectroscopy techniques. Analyses were performed for 15 elements that constitute the principal

components of the TMI-2 core. For comparison purposes, Table 4 lists the elemental composition of each of the core constituents (see Reference 5) and the average composition of the TMI-2 core if the core was homogeneously mixed (including end fittings). These data include the oxygen content of the uranium but exclude the oxygen that might be present due to the oxidation of zircaloy and structural materials.

Table 5 lists the average compositions of the companion samples from the three quadrants of the lower head for which examinations were performed. The individual particle examination results on which these averages are based are listed in Appendix B. Comparison of the individual examination results indicates that composition of the companion sample material is similar throughout and suggests that the molten pool was well mixed before the debris was solidified. This mixing probably occurred in the molten pool before the debris relocated to the lower head and before a small amount of additional Fe and Cr was added during the relocation process.

The total amount of material accounted for in this analysis is between 84 and 88 wt% of the total sample weight. Within the uncertainties of the analysis, the remaining material is accounted for by the oxidation of the uranium and zirconium present in the samples.

Comparison of the analysis results with Table 4 indicates that the fuel melt is composed almost entirely of the constituents of a fuel rod and that little contamination of the pool by other structural constituents occurred. A comparison of the companion sample results with the loose debris sample analysis results is discussed in Section 5.

4.4.1 Radionuclide Examinations

The radionuclide content of the lower head debris samples was measured for the samples discussed in the previous section. Results of the radiochemical analysis of the individual particle samples are listed in Appendix B. To provide information on the characteristic behavior of fission products, they have been categorized by the volatility of the chemical group and element as shown in Table 6.[5] Possible chemical compounds have been identified, and the radionuclides for which analyses were performed are indicated in the table.

Table 4. TMI-2 reactor core composition.

Material (weight)	Elements	Weight Percent	Average Core Composition	
			Element	Composition (weight percent)
UO_2	U-235[a]	2.265	U	65.8
(94,029 kg)[a]	U-238[a]	85.882	Zr	18.0
(531.9 kg)[b]	0	11.853	O	8.5
			Fe	3.0
Zircaloy-4	Zr[a]	97.907	Ag	1.8
(23,177 kg)[a]	Sn[a]	1.60	Cr	1.0
(125 kg)[b]	Fe[a]	0.225	Ni	0.9
	Cr[a]	0.125	In	0.3
	O	0.095	Sn	0.3
			Al	0.2
Type-304 stainless steel	Fe[a]	68.635	B	0.1
(676 kg) and unidentified	Cr[a]	19.000	Cd	0.1
stainless steel (3960 kg)	Ni[a]	9.000	Mn	0.8
(16.8 kg)[b]	Mn[a]	2.000	Nb	0.04
	Si[a]	1.000		
	N	0.130		
	C	0.080		
	Co	0.080		
Inconel-718	Ni[a]	51.900		
(1211 kg)	Cr[a]	19.000		
(6.8 kg)[b]	Fe[a]	18.000		
	Nb[a]	5.553		
	Mo[a]	3,000		
	Ti	0.800		
	Al[a]	0.600		
	Co	0.470		
	Si[a]	0.200		
	Mn[a]	0.200		
	N	0.130		
	Cu	0.100		
Ag-In-Cd	Ag[a]	80.0		
(2749 kg)	In[a]	15.0		
(43.5 kg)[b]	Cd[a]	5.0		
B_4C-Al_2O_3	Al[a]	34.33[c]		
(626 kg)	O	30.53[c]		
(0 kg)[b]	B[a]	27.50[a]		
	C	7.64[c]		
Gd_2O_3-UO_2	Gd[a]	10.27[c]		
(131.5 kg)	U[a]	77.72[c]		
(O kg)[b]	O	12.01[c]		

a. Elements for which ICP (inductively coupled plasma) analysis was performed.
b. Weight of material in a control rod fuel assembly.

Table 5. Average debris composition by quadrant[a] (wt%).

Element	Southeast (1-9)	Southwest (1-11)	Northeast (1-12)
U	72.3	70.8	68.2
Zr	14.1	12.0	15.2
Sn	--[b]	--[b]	--[b]
Ag	--[c]	--[c]	--[c]
In	0.28[d]	0.26[d]	--[b]
Al	--[b]	--[b]	--[b]
Cr	0.33	0.26	0.52
Fe	0.74	0.53	0.93
Mg	--[b]	--[b]	--[b]
Mn	0.030	0.026	0.028
Mo	--[b]	--[b]	--[b]
Nb	--[b]	--[b]	--[b]
Ni	0.099	0.081	0.10
Total[d]	87.8	84.3	85.1

a. This table presents the average of the examination results obtained from the companion samples; however, due to the small number of samples examined, these data must be used with caution.

b. Not detected. The average composition is calculated using only real values and is averaged without zero values.

c. Due to the analysis method used, some loss of Ag may have occurred during the analysis.

d. Total of measurable constituents. Oxygen content was not measured.

Table 6. Radionuclide volatility groups.

WASH-1400 Group Number	Chemical Group	Element	Boiling Temperature[a] (K)	Volatility	Possible Compounds	Boiling Temperature[a] (K)	Analysis Volatility
I	Noble gases	Kr[b]	120	High		--	--
		Xe[b]	166	High		--	--
II	Halogens	Br	332	High	CsBr	1,573	High
		I	458	High	CsI[b]	1,553	High
					HI	238	High
					I_2	457	High
III	Alkali metals	Rb[b]	973	High	Rb^I	1,573	High
					Rb_2O	--	High
					Rb_2O_2	1,284	High
		Cs[b]	963	High	CsI[b]	1,553	High
					Cs^{OH}	~1,350[c]	High
					Cs_2O	--	High
					Cs_2O_2	923	High
					CS_2UO_4[b]	--	--
IV.a	Heavy chalcogens	Se[b]	958	High	SeO_3	453	High
					SeO_2	--	--
		Te[b]	1,663	High	TeO_2	--	--
					Te_2O_2	--	--
					Silver-telluride	--	--
					Iron-telluride	--	--
					Zirconium telluride	--	--
					Tin-telluride	--	--
					Nickel telluride	--	--
					Chrome telluride	--	--
IV.b	Group VA metals	Sb[b]	1,653	Medium	Sb_2O_3	1,823	Medium
V	Alkaline earths	Sr	1,639	Medium	SrO[b]	~3,100	Low
		Ba	1,800	Medium	BaH_2	1,673	Medium
					BaO[b]	~2,273	Medium
					BaO_2	1,073	High
					$Ba(OH)_2$	1,053	High

Table 6. (continued).

WASH-1400 Group Number	Chemical Group	Element	Boiling Temperature[a] (K)	Volatility	Possible Compounds	Boiling Temperature[a] (K)	Analysis Volatility
VI	Rare earths	Eu	--	Medium	Eu_2O_3[b]	--	--
		Sm	2,173	Medium	Sm_2O_3[b]	--	--
		Pm	3,400	Low	Pm_2O_3[b]	--	--
	Actinides	Am	2,873	Medium	AmO_2[b]	--	--
	Noble metals	Pd	2,473	Low	PdO	--	--
		Rh	6,173	Low	RhO_2	--	--
			(est)		Rh_2O_3	--	--
		Ru	4,423	Low	RuO_2	--	--
					RuO_4	125	High
		Mo	4,780	Low	MoO_2[b]		
					Mo_2O_3	--	--
					MoO_3	--	--
		Tc	--	Low		--	--
VII	Rare earths	Y	3,260	Low	Y_2O_3[b]	--	--
		La	3,743	Low	LaO	--	Medium-high
					La_2O_3[b]	4,473	Low
		Ce	2,690	Low	CeO_2	--	--
					Ce_2O_3[b]	--	--
		Pr	3,400	Low	PrO_2	--	--
					Pr_2O_3[b]	--	--
		Nd	3,300	Low	Nd_2O_3	--	--
	Actinides	Np	--	Low	NpO2[b]	--	--
		Pu	3,508	Low	PuO_2[b]	--	Low
		Cm	--	Low	CmO_2[b]	--	--
	Tetravalents	Zr[c]	>3,173	Low	ZrO_2[b]	~5,273	Low
	Early transition	Nb	~3,573	Low	NbO_2	--	Low
					Nb_2O_5	--	--

a. Boiling temperature at 1 atm., data primarily from CRC Handbook of Chemistry and Physics, 56th Edition.

b. Probable chemical form of the fission product within the fuel.

c. Zirconium is both a fission product and a structural material.

The high-volatility fission product groups (I, II, III, and IV.a) are the noble gases, halogens, alkali metals, and heavy chalcogens. They are characterized by boiling points less than 1600 K for the elemental forms as well as for the listed oxide compounds. From this group, measurements were made for ^{129}I and ^{137}Cs.

The medium-volatility fission products are characterized by boiling points less than 3100 K (UO_2 melting). These fission products are from the Group VA metals, alkaline earths, some of the rare earths, and actinides. However, it should be noted that the volatility of these fission products is strongly dependent on the chemical form of the fission product. For example, ruthenium has two highly volatile oxides (i.e., RuO_2 and RuO_4) that either decompose or boil at less than 400 K. Radionuclides from these groups for which measurements were made are ^{125}Sb, ^{90}Sr, ^{154}Eu, and ^{106}Ru.

The low-volatility fission products include elements from the noble metals, the remaining rare earths and actinides, tetravalents, and early transition elements. Generally, the oxides of these elements have low volatilities; however, some (such as LaO or CeO) have lower boiling points than do the elements. The only radionuclide from this group that was measurable during the lower vessel examination program was cerium/praseodymium.

4.4.2 Comparisons with ORIGEN2

The measured radionuclide concentrations in the debris were compared with concentrations predicted by the ORIGEN2 code in order to assess the retention of radionuclides in the debris bed and to calculate the decay heat associated with the debris bed at and after the relocation event. The ORIGEN2 analysis model used for the TMI-2 core[5] contained 1,239 core nodes. Analyses were performed for ranges of burnup for each of the three ^{235}U enrichments present (i.e., 1.98%, 2.64%, and 2.98%). Table 7 lists the ORIGEN2 values used for comparison with the debris data. The original core average radionuclide concentrations were adjusted because the peripheral (2.98% enriched) assemblies did not participate in the accident. A later ORIGEN2 verification study that was performed for the TMI-2 core[5] indicated core-specific differences in radionuclide inventories. These changes were minor and were not included in the calculations so that direct comparisons could be made with the loose debris examination results reported in Reference 3. The indicated correction factors are listed in Table 7.

Table 7. ORIGEN2 predicted radionuclide concentrations (in microcuries/g U on April 1, 1986).

Radionuclide	Core Average[a]	Central Core Assemblies[b]	Verification Correction[c]	Adjusted Radionuclide Concentration
^{90}Sr	7740	1.08	0.988	8330
^{106}Ru	357	1.16	0.961	413
^{125}Sb	273	1.13	0.432	308
^{129}I	0.00281	1.11	0.867	0.00311
^{137}Cs	8900	1.09	1.021	9680
^{144}Ce	569	1.08	1.069	617
^{154}Eu	660	1.21	0.626	80

a. Core average concentration as listed in Reference 5.

b. Correction to the core average value to account for the fact that the peripheral 2.98% enriched fuel assemblies did not participate in the accident.

c. Correction for the measured variations from the predicted code values as defined and explained in Reference 5. This correction was not included for comparison purposes with previously analyzed loose debris samples.

The method used to estimate retention is

$$\frac{\text{Radionuclide concentration } (\mu\text{Ci/g})}{\text{Uranium content (gU/g sample)}} * \frac{100}{\text{ORIGEN2 predicted radionuclide concentration (microcuries/g uranium)}} = {}^{235}\text{U normalized fission product (retention in \%)} \quad (1)$$

The radionuclide concentrations and uranium concentrations used were from Appendix B. The results of these calculations, normalized fission product retentions, are listed in Table 8. A wide range of retentions is indicated for most radionuclides, including the relatively stable low-volatile radionuclides. The following sections contain discussions of the radionuclide retentions for the low-, medium-, and high-volatility fission products.

4.4.3 Low Volatiles

The low volatiles for which radionuclide comparisons were performed are ^{144}Ce and ^{154}Eu. Table 8 lists the normalized retentions for the companion samples. It should be noted that within the uncertainties of the analysis, complete retention or some small losses of ^{154}Eu occurred. Uncertainties in the production of ^{154}Eu account for the low values and suggest that no loss of ^{154}Eu occurred.

4.4.4 Medium Volatiles

The fission products that are expected to have a medium volatility are ^{90}Sr and ^{125}Sb. Strontium-90 is the least volatile and is expected to be retained by the fuel to the greatest extent. The ^{90}Sr data shown in Table 8 indicate a range of retentions from 48 to 96% and suggests some release of this fission product. The medium-volatile radionuclide ^{125}Sb exhibits a greater range of retentions because it is expected to remain in a metallic state due to the high oxidation potentials required for the oxidation of this element, and would be expected to be more mobile. In previous core examinations, an increase in metallic content generally correlated with increases in ^{125}Sb content for metallic samples in the upper core region.

Table 8. Radionuclide retention in the debris bed.[a]

Radionuclide	Radionuclide Retention(%)		
	Southeast (1-9)	Southwest (1-11)	Northeast (1-12)
^{90}Sr	48	47	96
^{125}Sb	1.9[b]	1.1[b]	5.6[b]
^{137}Cs	3.6	1.3	18
^{144}Ce	91	85	97[b]
^{154}Eu	83	84	80
^{129}I	--[c]	--[c]	--[c]

a. Retention is calculated based on the uranium content of the sample material as determined from the elemental analysis results in Appendix B.

b. A radionuclide concentration was not detectable. Only nonzero values are represented in the average.

c. Iodine-129 values are not included due to reactor shutdowns at the INEL. Results will be included in the final VIP report, if possible.

4.4.5 High Volatiles

The high-volatile radionuclide for which analyses were performed is ^{137}Cs. The volatile ^{137}Cs was measurable in all samples at retentions substantially lower than those found in intact fuel material; however, there were higher retentions in the northeast quadrant (18%). Why higher levels of this radionuclide and both medium- and low-volatile radionuclide concentrations were found in this region is not known.

Decay heat calculations were performed for the radionuclide retentions measured as part of this examination program (see Appendix C). Specific decay heats were calculated for 224 minutes after shutdown, the beginning of the relocation of debris to the lower head, and at 600 minutes for the later cooldown period. Some principal radionuclides were removed from the decay heat calculations. They were the noble gases (primarily Xe and Kr) and the high volatiles (all cesiums and iodines). These radionuclides were removed from the calculation because they would not be expected to be present in the melt as they would have volatilized and been released from the fuel before the molten material relocated to the lower head. The decay heat produced from the selected radionuclide list is 0.13 watts/g of debris at 224 minutes and 0.096 watts/g of debris at 600 minutes after the accident. These data indicate a slow reduction in the decay heat available to keep the lower head debris in a liquid state or as a partially solidified slurry. Much of the decay heat would be expected to be retained in the central mass and protected from cooling by a protective ceramic layer.

5. COMPARISONS WITH DOE LOOSE DEBRIS ANALYSES

Examinations of loose debris samples obtained as part of the DOE program were performed during 1987 (see Reference 3) to determine physical properties such as density and porosity, metallurgical properties, composition, and radionuclide content. These samples were obtained before drilling operations began in the upper core region. Consequently, they would be expected to be representative of the composition of the debris material that relocated to the lower head 224 minutes after shutdown.

The average density of the loose debris samples is lower than the average density of the companion samples. The densities of the loose debris samples ranged from 6.57 to 8.25 g/cm^3, and the average density of these samples was about 7.1 g/cm^3. In contrast, the densities of the companion samples had a higher range (7.45 to 9.4 g/cm^3), and the average density of the individual companion sample particles was 8.4 ± 0.6 g/cm^3. It should be noted that the average density of the individual particles is statistically the same as the density of the companion samples (8.7 g/cm^3).

The measured porosities of the loose debris samples ranged between 9 and 31%, and the average porosity was about 27%. In contrast, the porosities of the companion sample debris ranged from 5% to 41%, and the average porosity was 18 ± 11%. These data suggest that at least part of the difference in the densities between the loose debris samples and the companion samples is due to the lower average porosity of the companion samples. In addition to differences in the porosity, there are differences in the composition of the loose debris as compared to the companion samples.

The loose debris had a uranium content that ranged from 62 to 73 wt%, with an average uranium content of 65 wt%. This is lower than the average uranium content of the companion samples, which was about 70 wt%. However, the average Zr content of the loose debris samples (12.6 wt%) is similar to the average Zr content of the companion samples (13.8 wt%).

In the loose debris samples, the Fe content ranged from 1.8 to 3.7 wt% with an average of 2.4 wt%. In contrast, the average Fe content of the companion samples was about 0.7 wt%. In addition, the concentrations of Cr, Ni, Mn, and Mo were higher in the loose debris than in the companion samples. It is unclear why the loose debris had slightly higher concentrations of

structural materials than the companion samples. In general, these data suggest that the entire debris bed (loose debris and companion debris) is relatively homogeneous.

Comparisons of radionuclide retention were performed between the loose debris and the companion samples, and it was determined that the radionuclide retention was similar in both locations.

6. DATA REQUIRED FOR MODEL DEVELOPMENT

The data required to develop the margin-to-failure analysis for the TMI-2 reactor vessel are the physical, metallurgical, and radiochemical characteristics of the debris. The physical property data required are the bulk density of the debris, the porosity, and the particle size distribution. The data needed from the metallurgical examinations are the initial debris bed temperature and melting point, the extent of oxidation of the debris by element, and the cooling rate of the debris bed. From the radiochemical examinations, the information needed is the composition of the debris bed, the fission product retention, and the decay heat available during and after the relocation event. Additional information such as the height of the companion layer and the distribution will be provided as part of the lower head mapping task being performed for the TMI-2 VIP.

The measured physical properties (density and porosity) of the companion samples were discussed in previous sections. The average density of the individual particle samples was determined to be 8.4 ± 0.6 g/cm^3. This compares well with the average density of the companion samples (8.7 g/cm^3) and suggests that a density of 8.7 g/cm^3 should be used for calculational purposes. For comparison purposes, a calculation was performed to determine the theoretical density of the debris based on the density of UO_2 (10.9 g/cm^3) and the density of ZrO_2 (5.6 g/cm^3). Based on a weighted average of the densities of these two primary constituents, the average density without porosity would be 10.4 g/cm^3. However, if this density is adjusted for a porosity of 18%, the theoretical density would be about 8.8 g/cm^3, which is similar to the measured average densities of the debris.

The porosities of the individual particle samples ranged from 5% to 41%, and the average porosities of the individual particles from each quadrant ranged from 17 to 21%, with an average companion sample porosity of 18 ± 11%. A comparison of these results with the average porosity of the loose debris (27%), as discussed in the previous section, suggests that an appropriate porosity for calculational purposes would be 18%, and that a porosity of about 27% should be used for loose debris calculations.

Information was requested on the particle size distribution for the companion samples. However, defueling information indicates that the companion material was a monolithic mass and suggests that the companion layer should be assessed as an intact block of material. In the case

of the loose debris, photographic examinations of the debris bed indicated that the debris bed was a consolidated mass with relatively small particulate debris (powder) present around large pieces (30-40 cm in diameter) of debris. The distribution of loose debris over the companion debris is being obtained from the lower head mapping task.

The specific data needed from the metallurgical examinations are the initial debris bed temperature and melting point, the extent of oxidation of the debris, and the cooling rate of the debris bed. Although specific measurements of these properties were not made as part of this project, information on these characteristics can be obtained from the metallurgical results. Also, the relative homogeneity of the debris bed and the presence of few constituents other than U, Zr, and O allows some information to be deduced from the available data.

Hofmann[6] addressed the range of temperatures that might be expected in a severe reactor accident and has shown that the lowest temperatures that might be expected in the dissolution of uranium by zirconium are on the order of 1,760°C, about 1,000°C below the melting point of UO_2 (~2,850°C). However, the companion samples have compositions that are principally $(U,Zr)O_2$ (i.e., about 78 wt% UO_2 and 17 wt% ZrO_2) with some secondary $(Zr,U)O_2$ phases. Hofmann also indicates that a well-mixed $(U,Zr)O_2$ solid solution, as shown by the metallography and SEM results, would be expected to be found in a peak temperature range between 2,600°C and 2,850°C. Consequently, without further experimental validation, it is suggested that the peak temperature of the melt that relocated to the lower head was probably greater than 2,600°C.

Based on the metallography and SEM examination results, the extent of the oxidation of the companion samples can be considered to be almost complete with little or no unoxidized material present other than materials such as silver. Dot maps with other constituents such as Fe and Cr were found to have similar oxygen concentrations to the $(U,Zr)O_2$ melts, and would be expected to be fully oxidized. These data suggest that the companion debris was fully oxidized with little metallic material present.

The cooling rate of the debris bed has been discussed in previous sections; however, the most important point that addresses the cooling rate is the formation of secondary phases around pores and in the matrix material. These secondary phases contain apparent $(Zr,U)O_2$ phases with the presence of Fe and Cr. The formation of these phases would require a long cooldown period to allow the phase separation to occur between the $(U,Zr)O_2$ and $(Zr,U)O_2$ phases. Bart[7] has

suggested that the cooling time should be between 3 and 72 hours to cause this type of phase separation. This is consistent with a molten mass of material that is thermally isolated from the cooling water above the debris bed. A further analysis of the amount of time at temperature will be based on decay heat calculations for the companion debris as part of the VIP integration report.

From the radiochemical examinations, the information required for the margin to failure analysis is the composition of the debris bed, fission product retention, and the decay heat available during and after the relocation event. As previously discussed, the composition of the debris bed is similar for all samples with an average composition of about 70 wt% U, 13.75 wt% Zr, and 13 wt% O. This composition accounts for about 97 wt% of the debris.

The fission product retention in the debris was discussed in Section 4. Of particular interest to the margin-to-failure analysis is the decay heat present in the debris bed during the relocation event and during the cooldown period. The decay heat at 224 minutes after shutdown is 0.18 watts/g of U, and at 600 minutes, it is 0.14 watts/g of U. After conversion of these data to the known debris composition, the decay heat present is 0.13 watts/g of debris at 244 minutes, and at 600 minutes, it is 0.096 watts/g of debris.

7. SUMMARY AND CONCLUSIONS

Examinations were performed on companion samples from three quadrants of the lower head. These examinations indicate that the debris bed is relatively homogeneous with relatively small variations in composition and density. The companion samples consisted primarily of previously molten $(U,Zr)O_2$ ceramic melt. Small amounts of metallic melt (< 0.5%) were found only in samples from the southwest quadrant. The pores in some of the samples were aligned in stratified layers and were surrounded by microporosity and two-phase structures consisting of uranium-rich $(U,Zr)O_2$ and zirconium-rich $(Zr,U)O_2$. As previously discussed, it has been suggested that these stratified layers are indicators of the percolation of gases through the melt and indicate relatively low cooling.

All the samples examined from the northeast quadrant were predominantly single-phase ceramic melt with widely varying amounts of porosity. The lack of segregated $(U,Zr)O_2$ and $(Zr,U)O_2$ phases may suggest more rapid debris cooling in this quadrant of the lower head.

The presence of two-phase $(U,Zr)O_2$ and $(Zr,U)O_2$ structures on some quadrants indicates that samples with this morphology were not rapidly quenched, but underwent a gradual cooldown. The microstructure is indicative of an overall composition that was uranium-rich $(U,Zr)O_2$.

Radiochemical analyses of the debris indicate that the debris was composed of about 70 wt% U, 13.75 wt% Zr, and 13 wt% O. This composition accounts for about 97 wt% of the debris. The remaining constituents are the elemental constituents of stainless steel and inconel core components that were probably melted during the relocation of debris to the lower head. Further, the examinations indicate that much of the high-volatile radionuclide content had volatilized out of the debris, leaving primarily medium- and low-volatile components in the debris bed. Decay heat analyses were performed to determine the amount of heat present in the debris bed during the relocation event and at 600 minutes. These calculations indicate that the retained heat in the lower debris bed was about 0.13 watts/g of debris at 244 minutes and 0.096 watts/g of debris at 600 minutes. These data indicate a significant reduction in the heat available to maintain the debris bed in a molten condition.

Comparisons of the companion sample data with the loose debris data indicate that the loose debris layer has a slightly lower uranium content, is more porous, and contains higher

concentrations of iron, chromium, and other constituents of stainless steel and inconel than do the companion samples. The information required for the margin-to-failure analysis that can be obtained from the companion sample analyses has been acquired. The relative homogeneity of the debris bed, as determined from the companion sample examinations, should make the margin-to-failure analysis more accurate and reduce uncertainties in the final assessment.

8. REFERENCES

1. J. P. Adams et al., *TMI-2 Lower Plenum Video Data Summary*, EGG-TMI-7429, EG&G Idaho, Inc., July 1987.

2. E. Tolman et al., *TMI-2 Core Bore Acquisition Summary Report*, EGG-TMI-7385 (Revision 1), EG&G Idaho, Inc., February 1987.

3. C. S. Olsen, D. W. Akers, and R. K. McCardell, *Examination of Debris from the Lower Head of the TMI-2 Reactor*, GEND-INF-084, EG&G Idaho, Inc., January 1988.

4. GPU TMI-2 Technical Bulletin, TB-89-02, February 27, 1989.

5. D. W. Akers et al., *TMI-2 Core Bore Examinations*, GEND-INF-092, January 1990.

6. P. Hofmann et al., "Reactor Core Materials Interactions at Very High Temperatures," *Nuclear Technology*, Vol. 87, August 1989.

7. G. Bart, "TMI-2 Core Sample Evaluation at Paul Scherrer Institute," *TMI-2 Examination Results from the OECD-CSNI Program - Volume 2* (Draft available from EG&G Idaho), EGG-OECD-9168, August 1990.

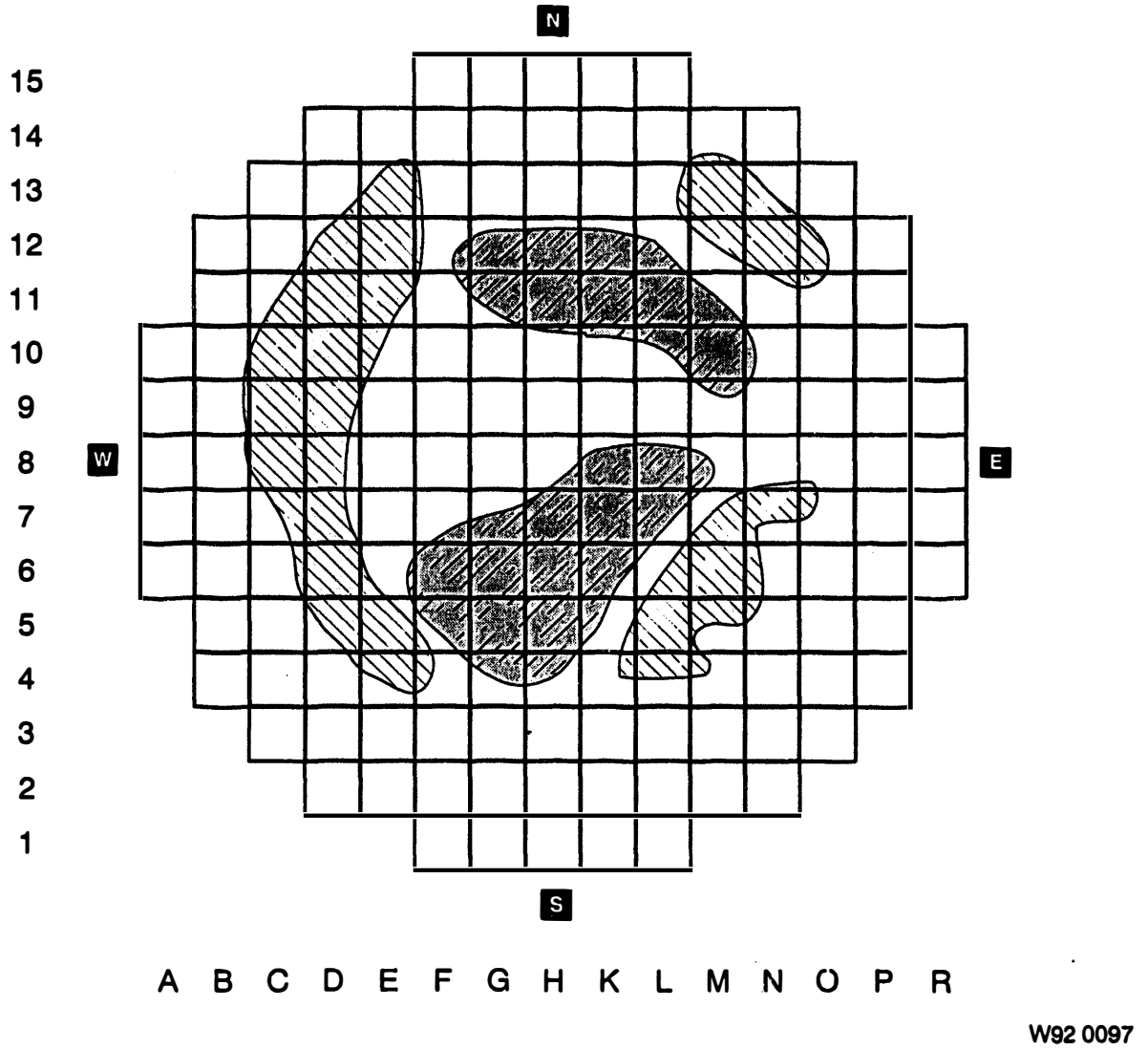

Figure 1. Loose debris distribution and location.

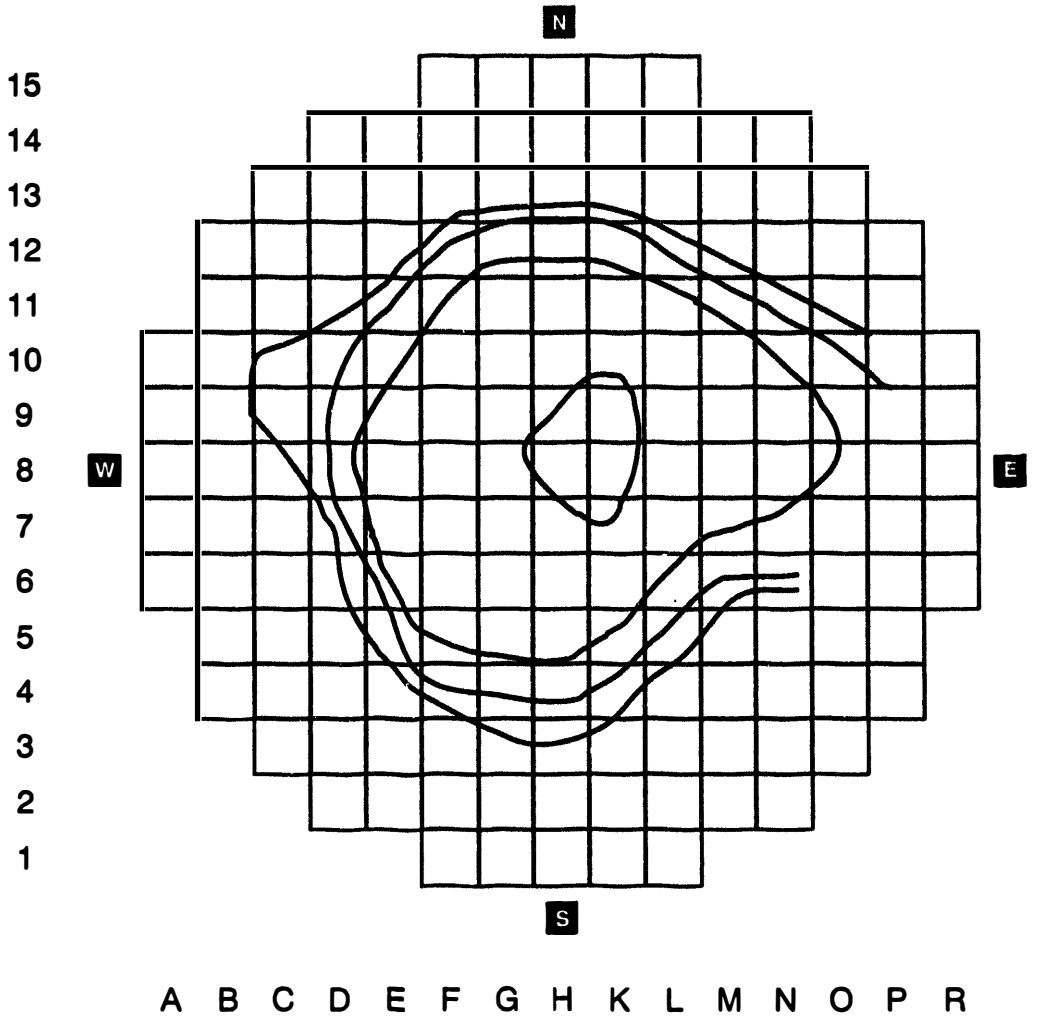

Figure 2. Hard debris distribution and location. (Contour lines are in 6-in. increments with the outside line equal to 0 in. and the inside equal to 18 in.)

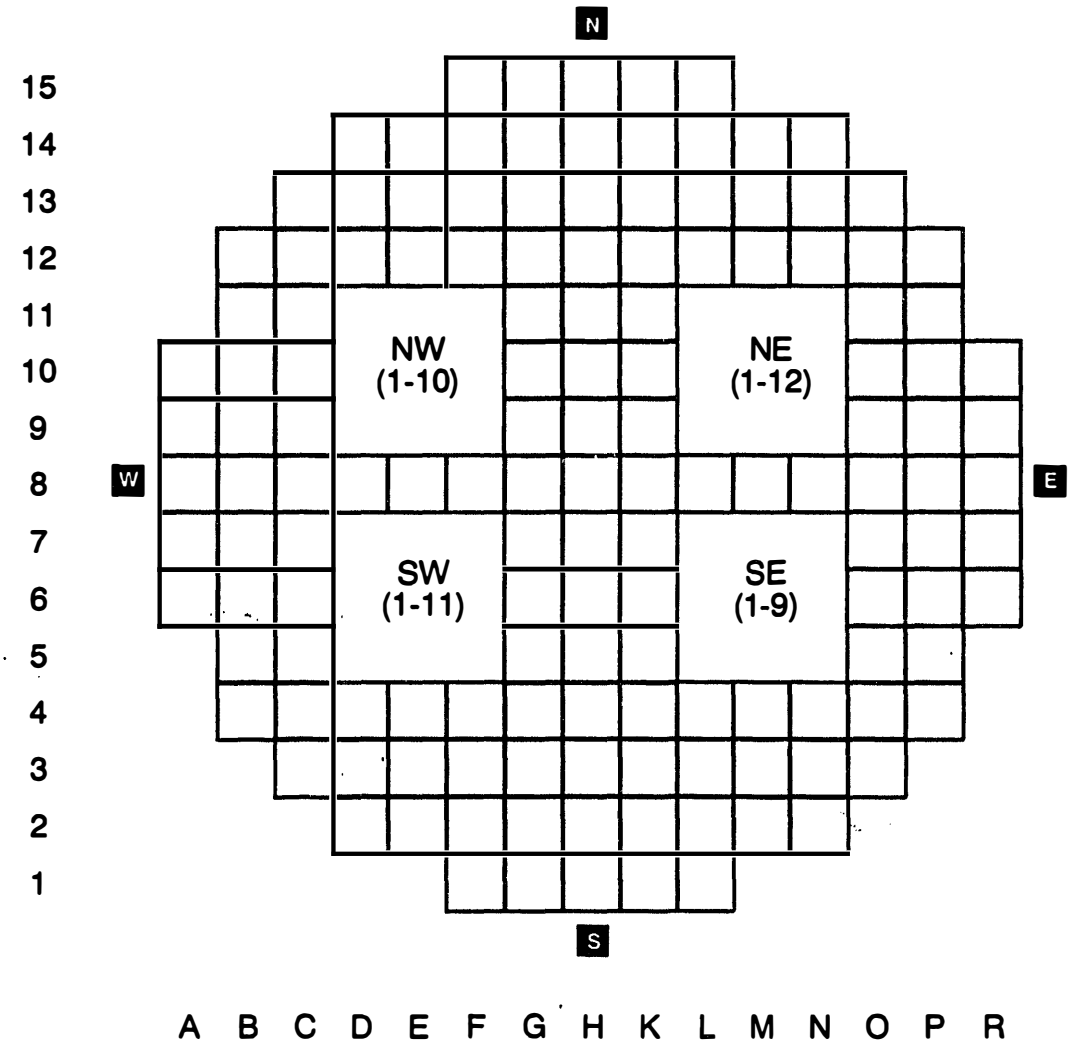

Figure 3. Locations of companion samples.

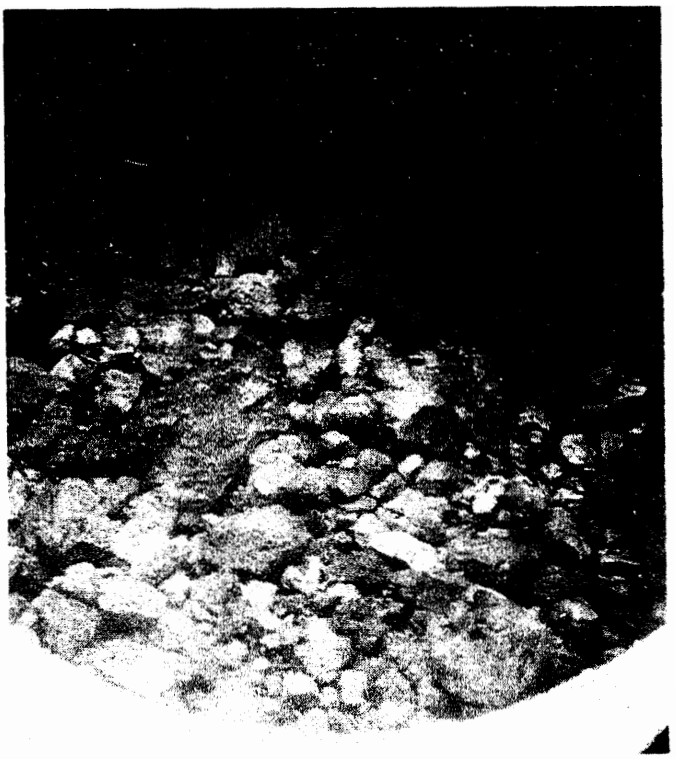

Figure 4. Sample collected from the southeast quadrant (sample 1-9).

Figure 5. Sample collected from the northwest quadrant (sample 1-10).

Figure 6. Sample collected from the southwest quadrant (sample 1-11).

Figure 7. Sample collected from the northeast quadrant (sample 1-12).

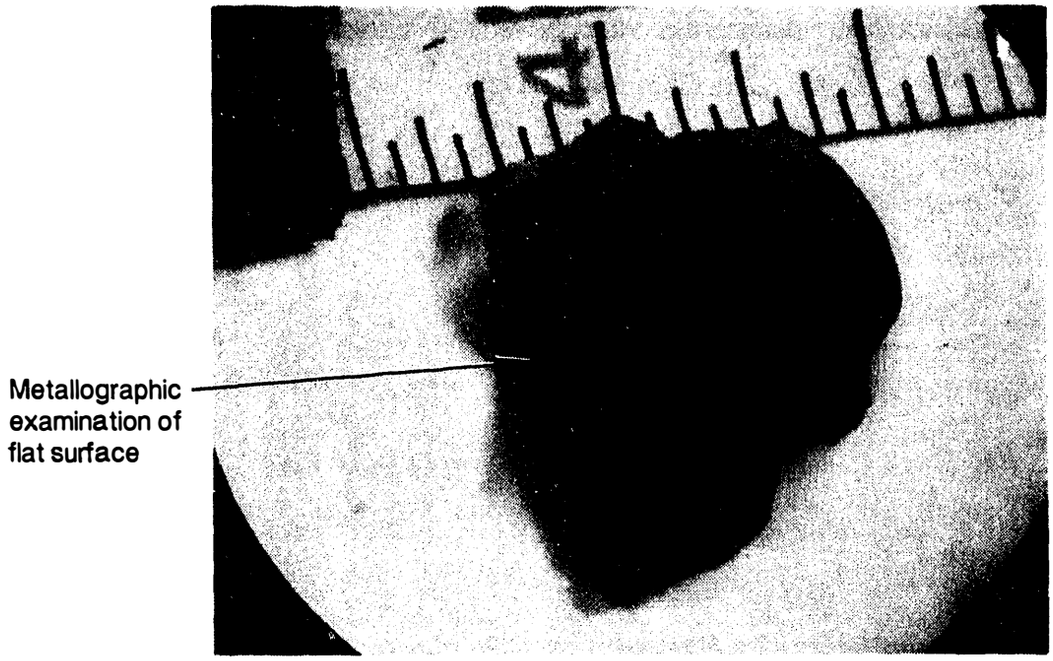

Figure 8. TMI-2 lower plenum sample 1-9-F.

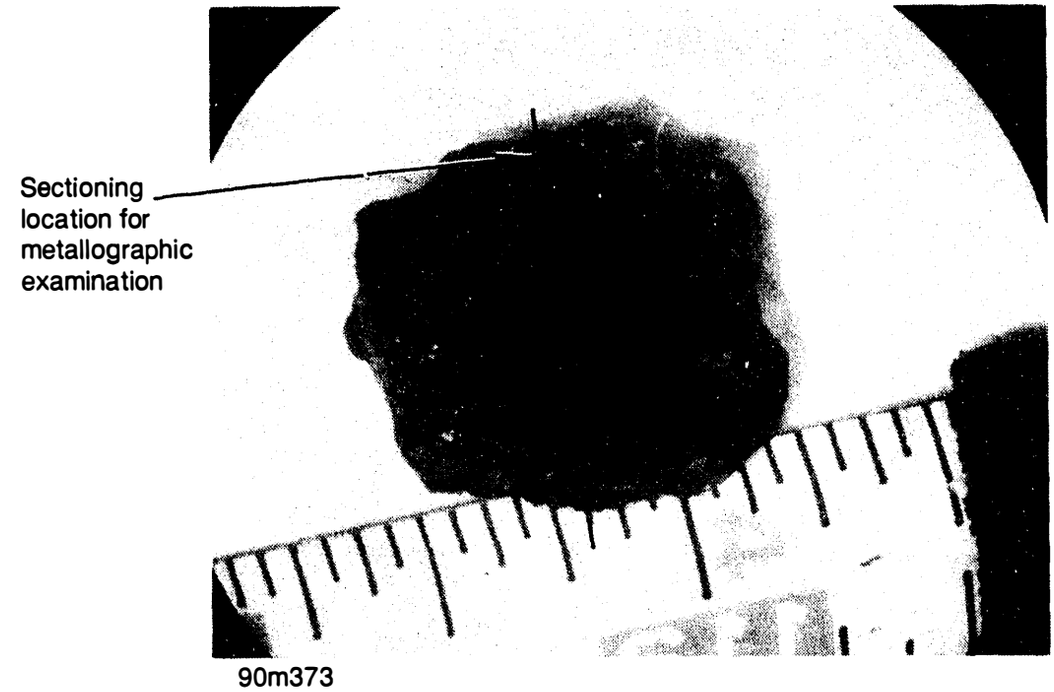

Figure 9. TMI-2 lower plenum sample 1-9-G.

90m376

Figure 10. TMI-2 lower plenum sample 1-11-C.

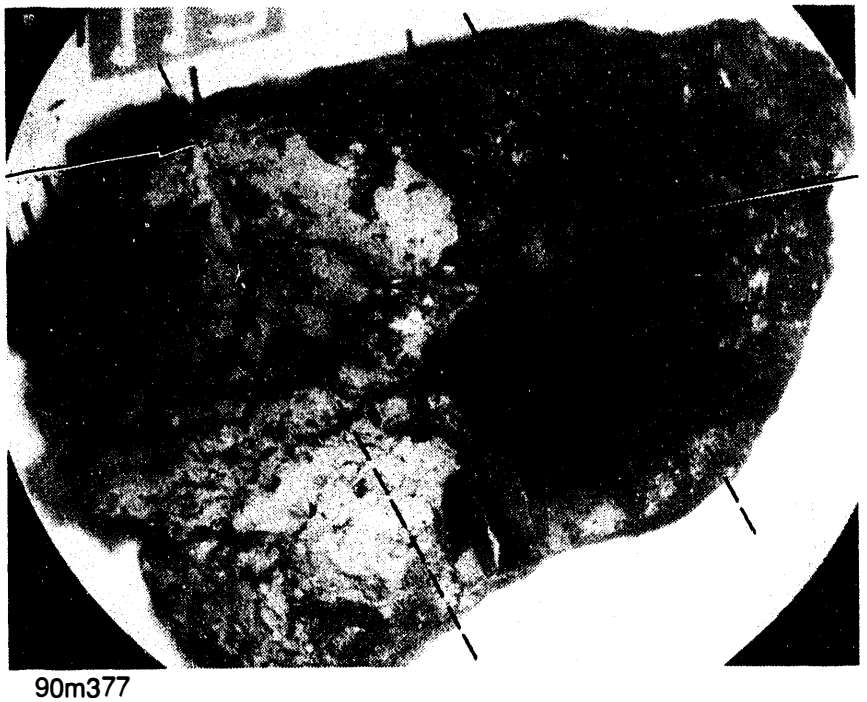

90m377

Figure 11. TMI-2 lower plenum sample 1-11-D.

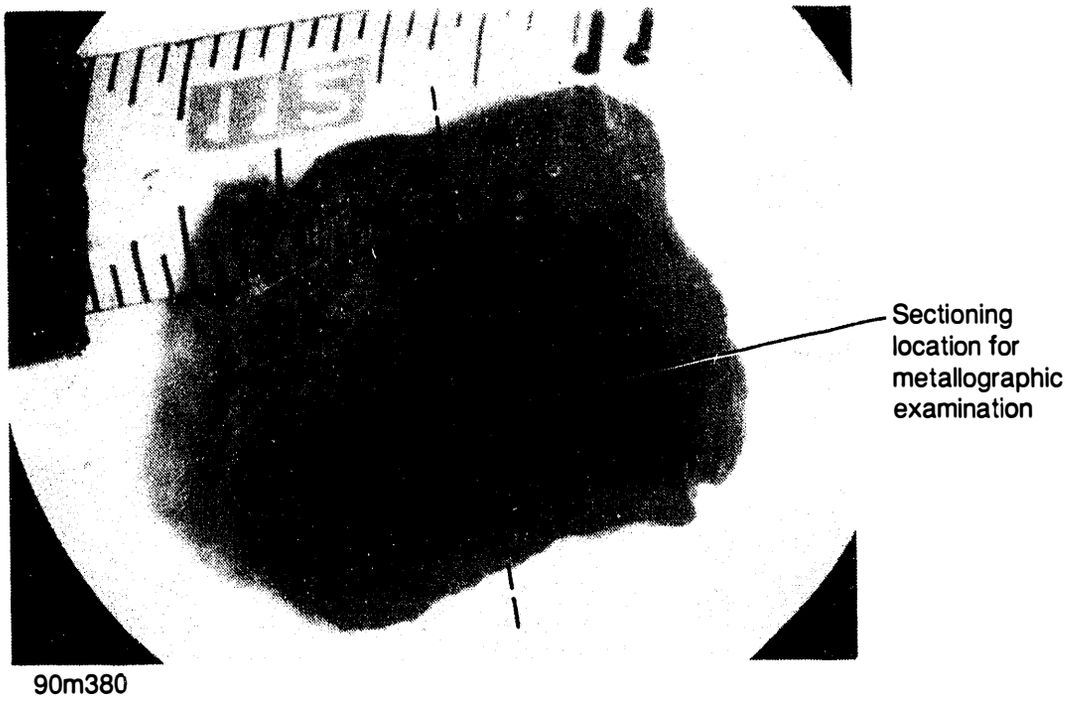

Figure 12. TMI-2 lower plenum sample 1-12-C.

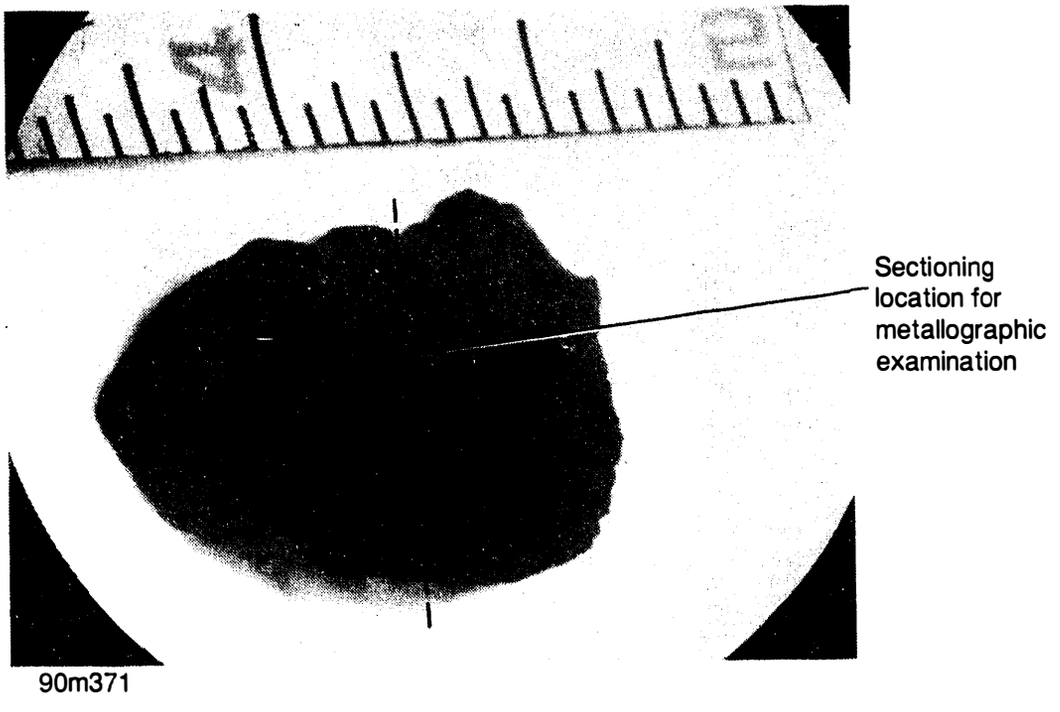

Figure 13. TMI-2 lower plenum sample 1-12-D.

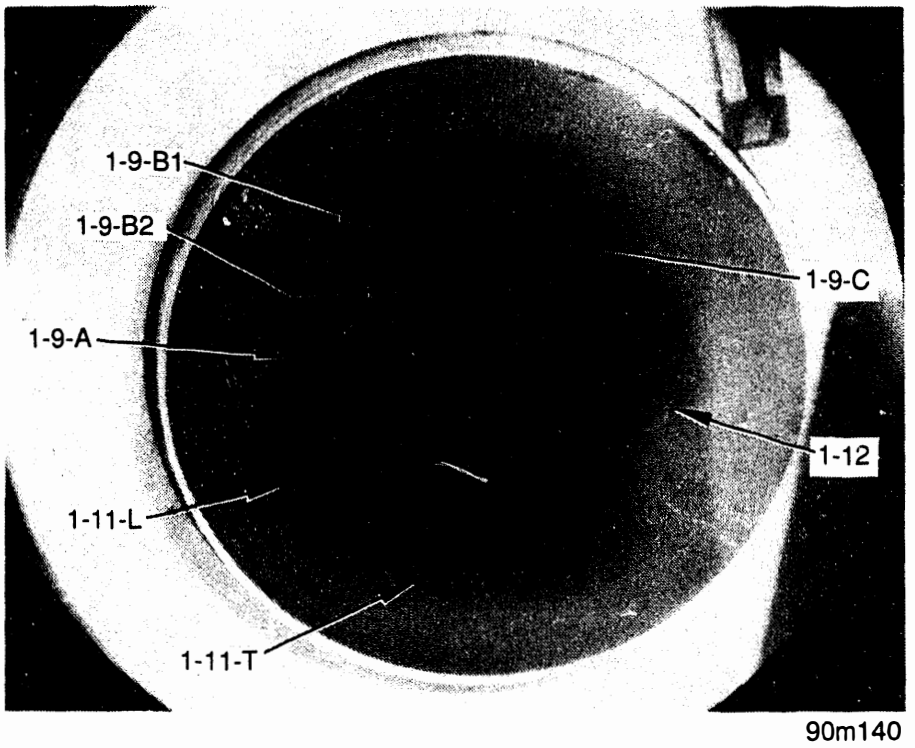

Figure 14. First epoxied and polished metallographic mount.

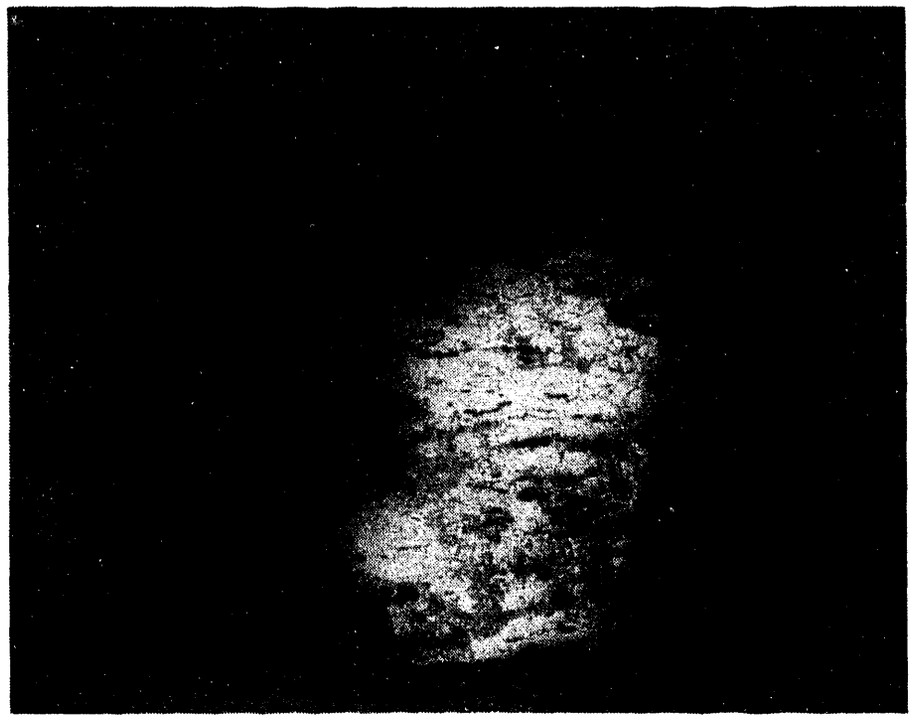

90m143 X2.3

Figure 15. Sample 1-9-A .

90m144 X3.0

Figure 16. Samples 1-9-B1 and 1-9-B2 .

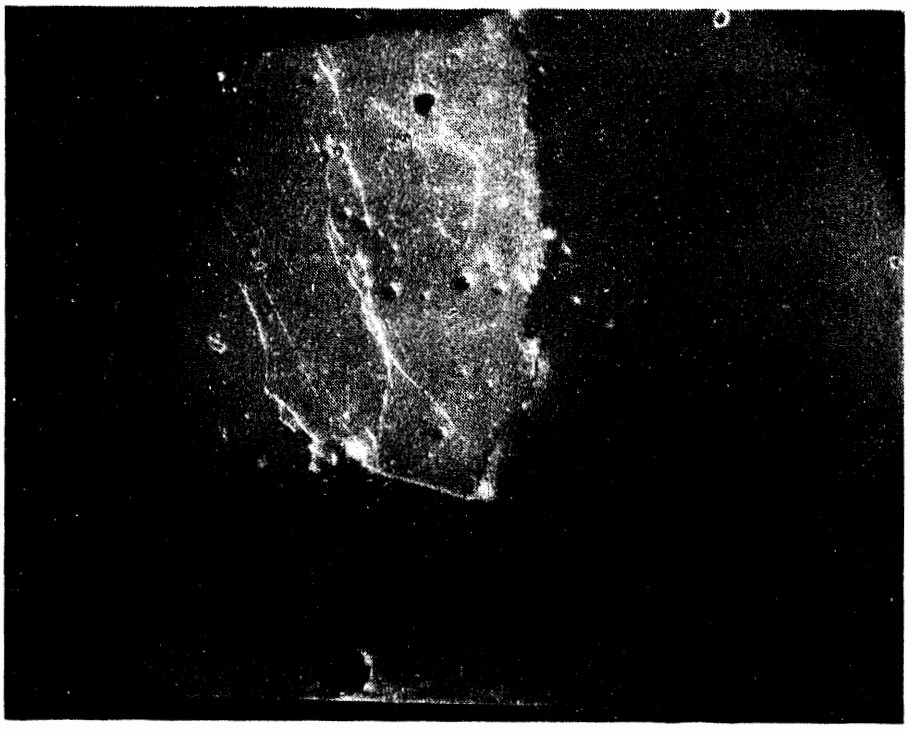

90m145 X3.9

Figure 17. Sample 1-9-C.

90m141 X2.9

Figure 18. Sample 1-11-L.

90m142 X2.8

Figure 19. Sample 1-11-T .

90m146 X2.4

Figure 20. Sample 1-12 .

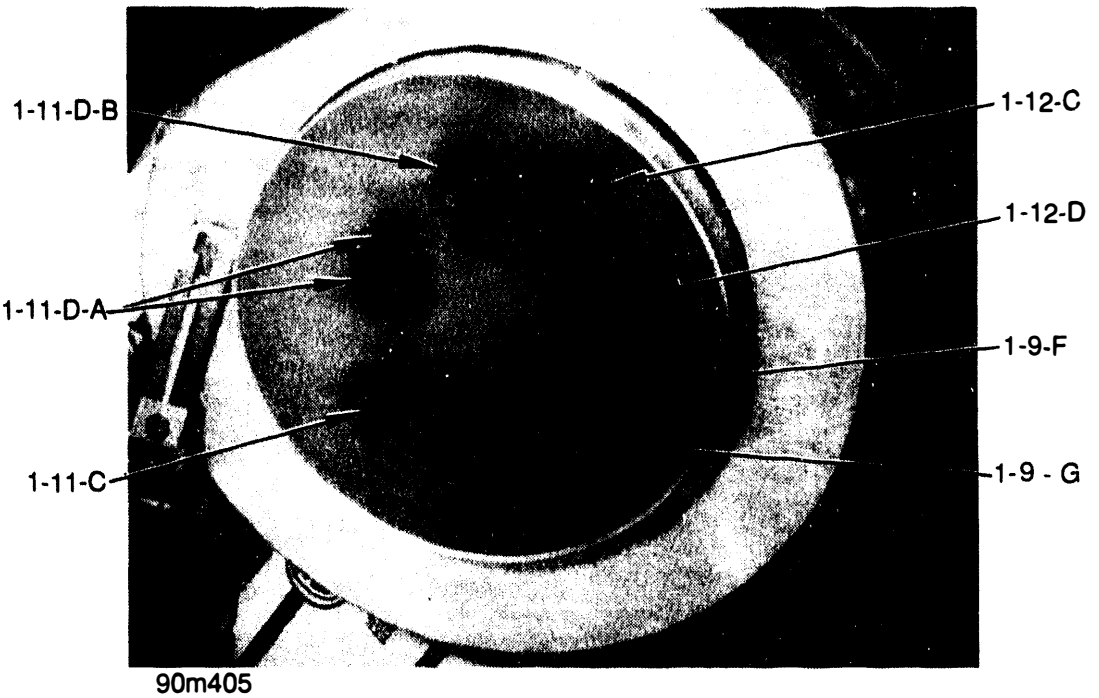

90m405

Figure 21. Second epoxied and polished metallographic mount.

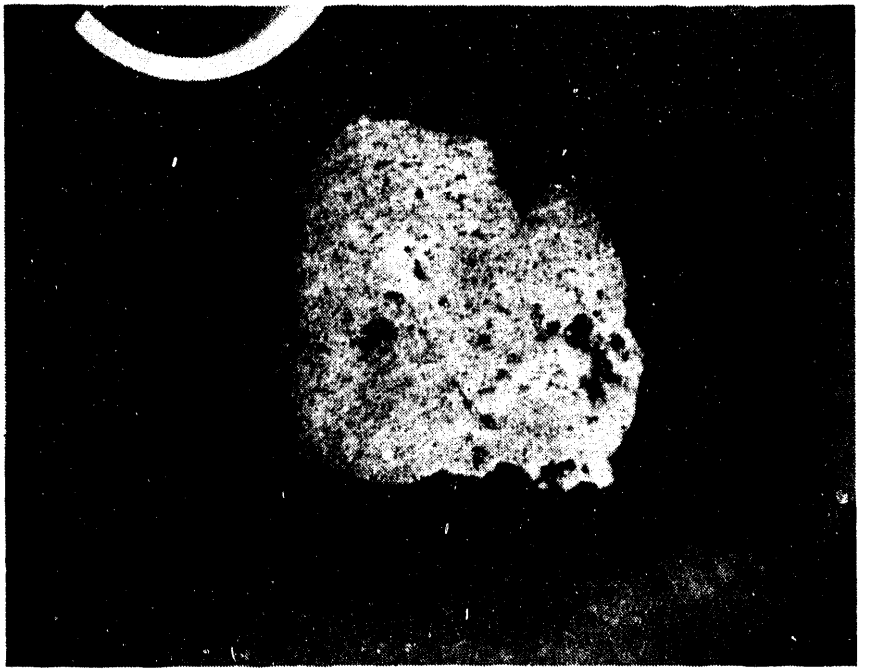

90m406 X2.4

Figure 22. Sample 1-9-F.

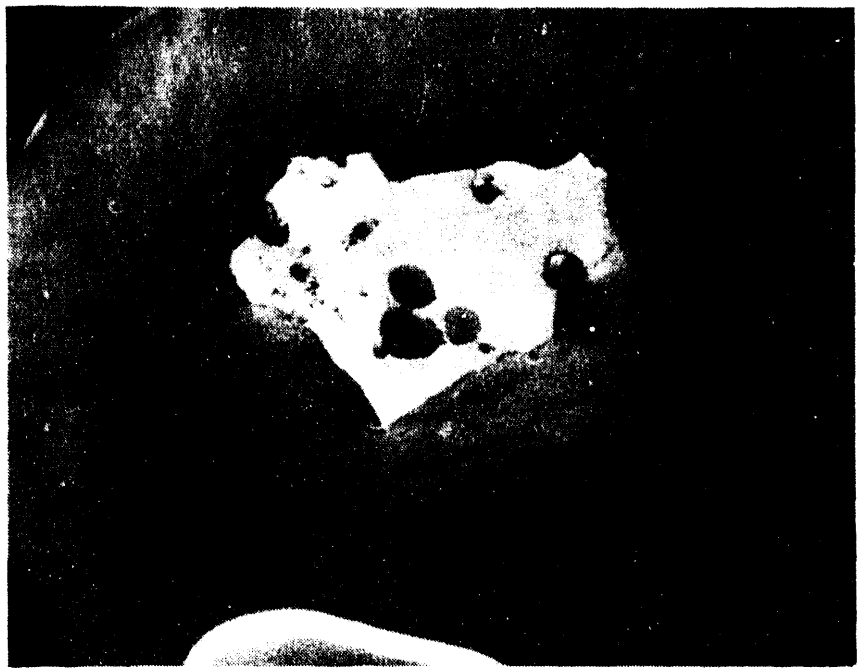

90m407 X2.7

Figure 23. Sample 1-9-G.

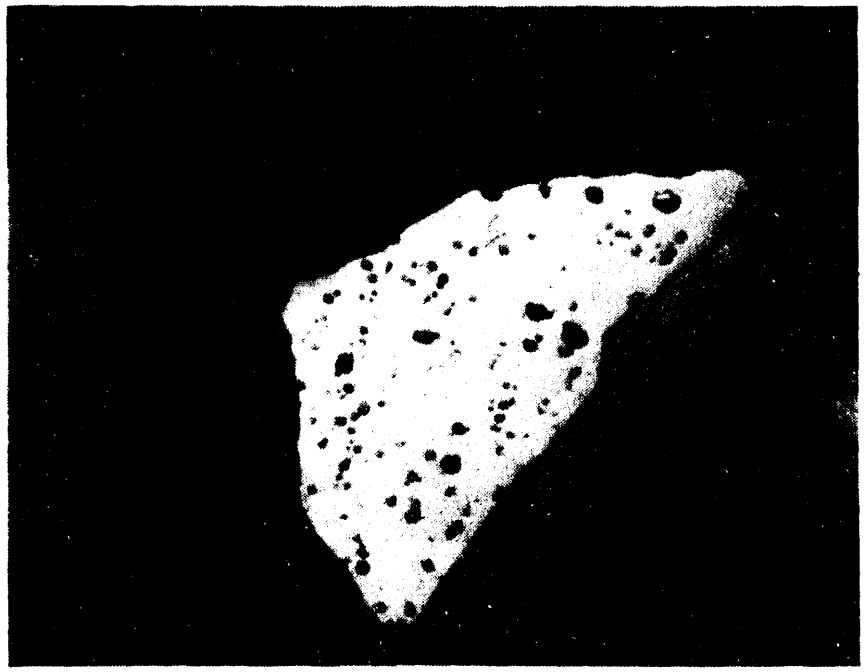

90m408 X2.9

Figure 24. Sample 1-11-C.

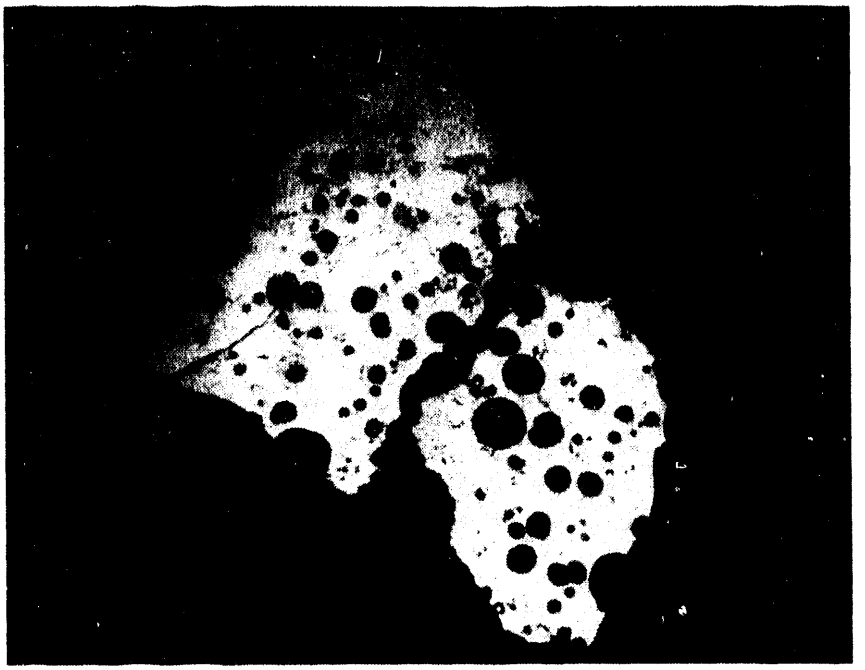

90m409 X2.8

Figure 25. Sample 1-11-D-A .

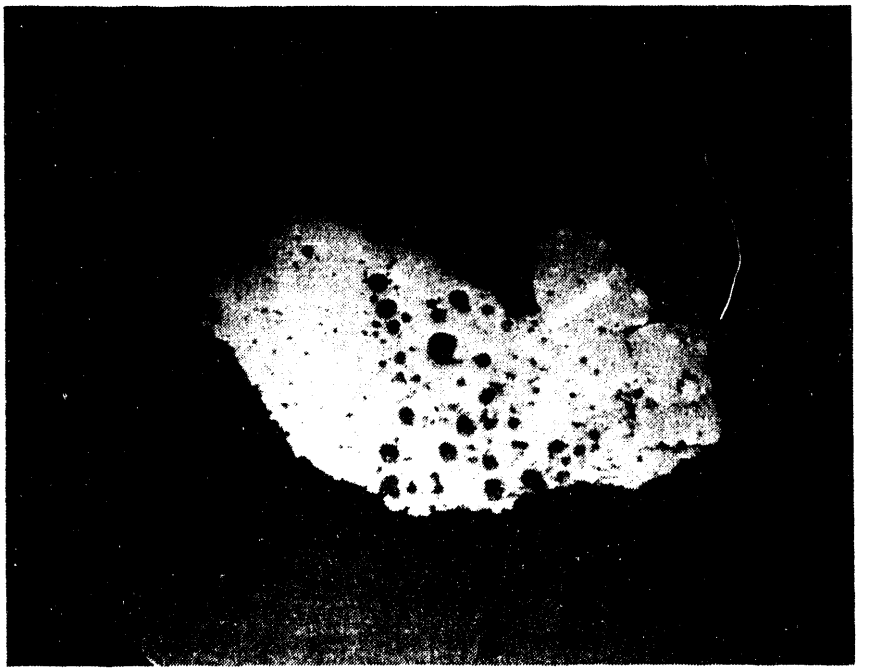

90m410 X2.6

Figure 26. Sample 1-11-D-B .

90m411 X2.5

Figure 27. Sample 1-12-C.

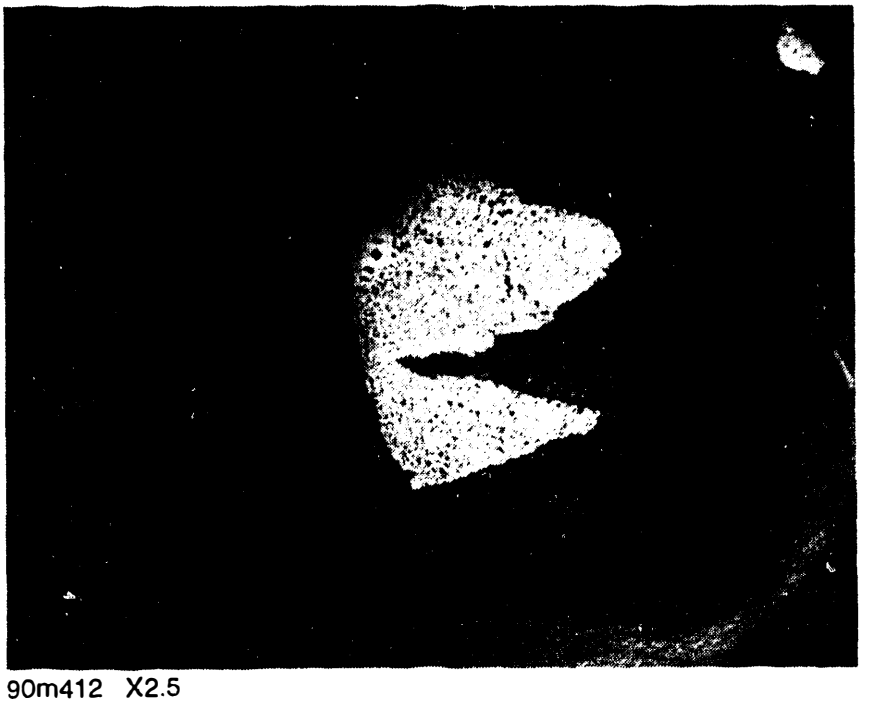

90m412 X2.5

Figure 28. Sample 1-12-D.

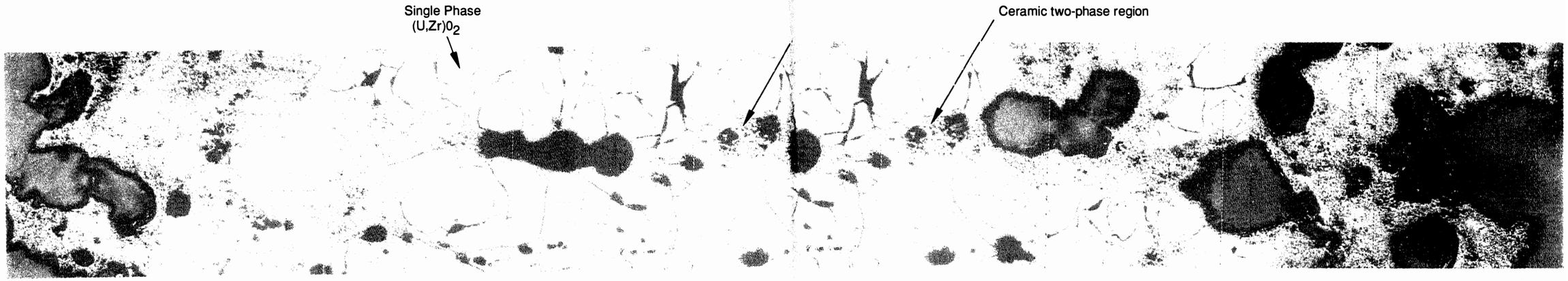

Figure 29. Typical microstructure of 1-9-A .

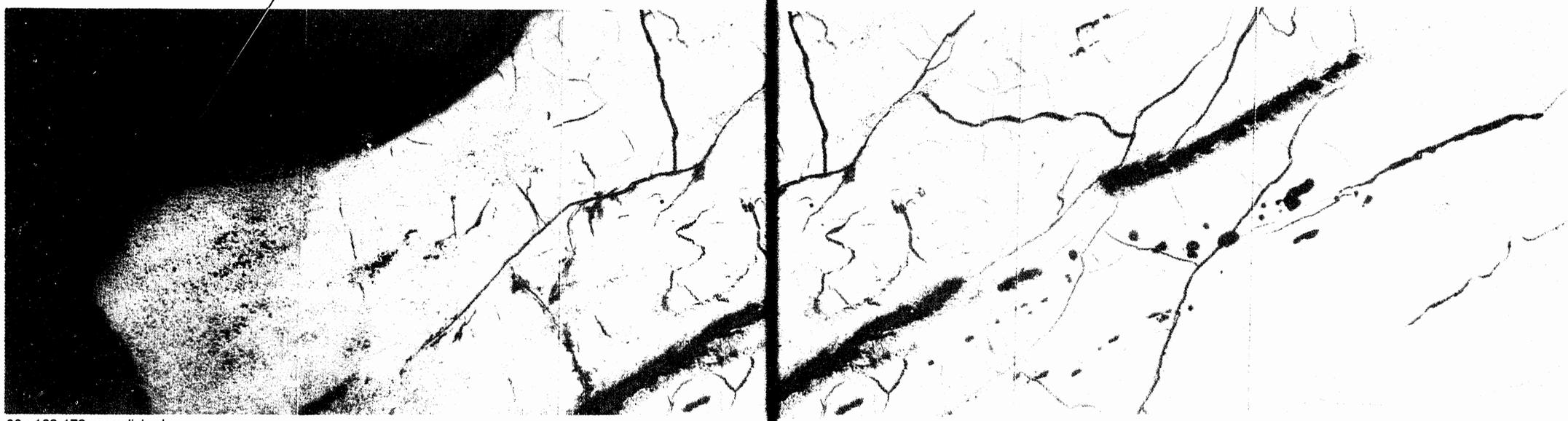

90m168-172, as polished

Figure 30. Typical microstructure of 1-9-B1.

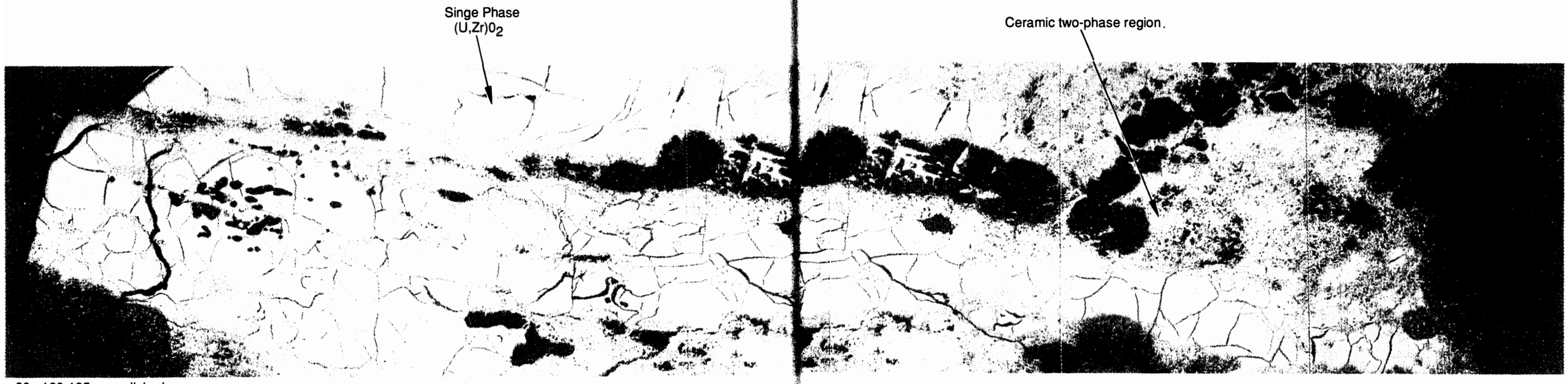

Figure 31. Typical microstructure of 1-9-B2.

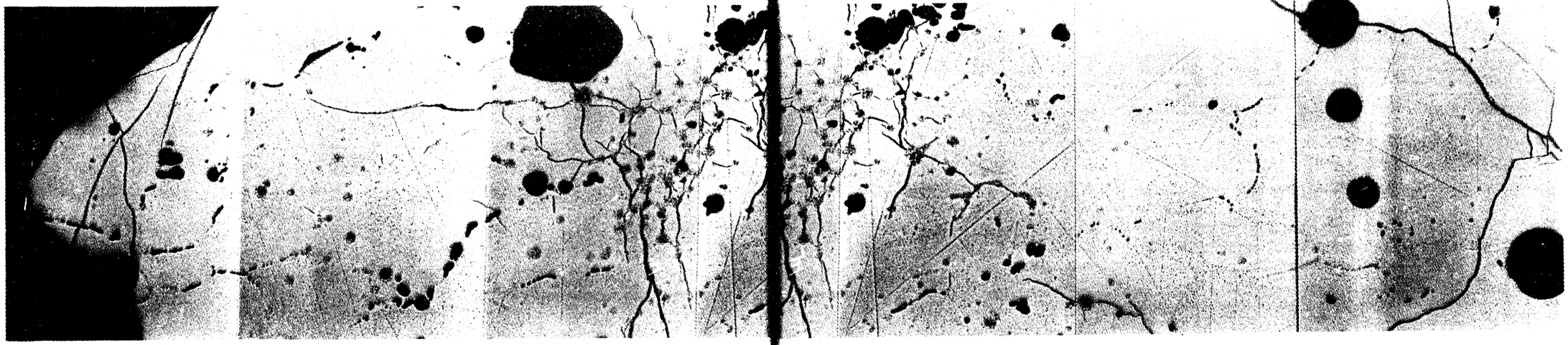

90m175-180, as polished

200µm

Figure 32. Typical microstructure of 1-9-C.

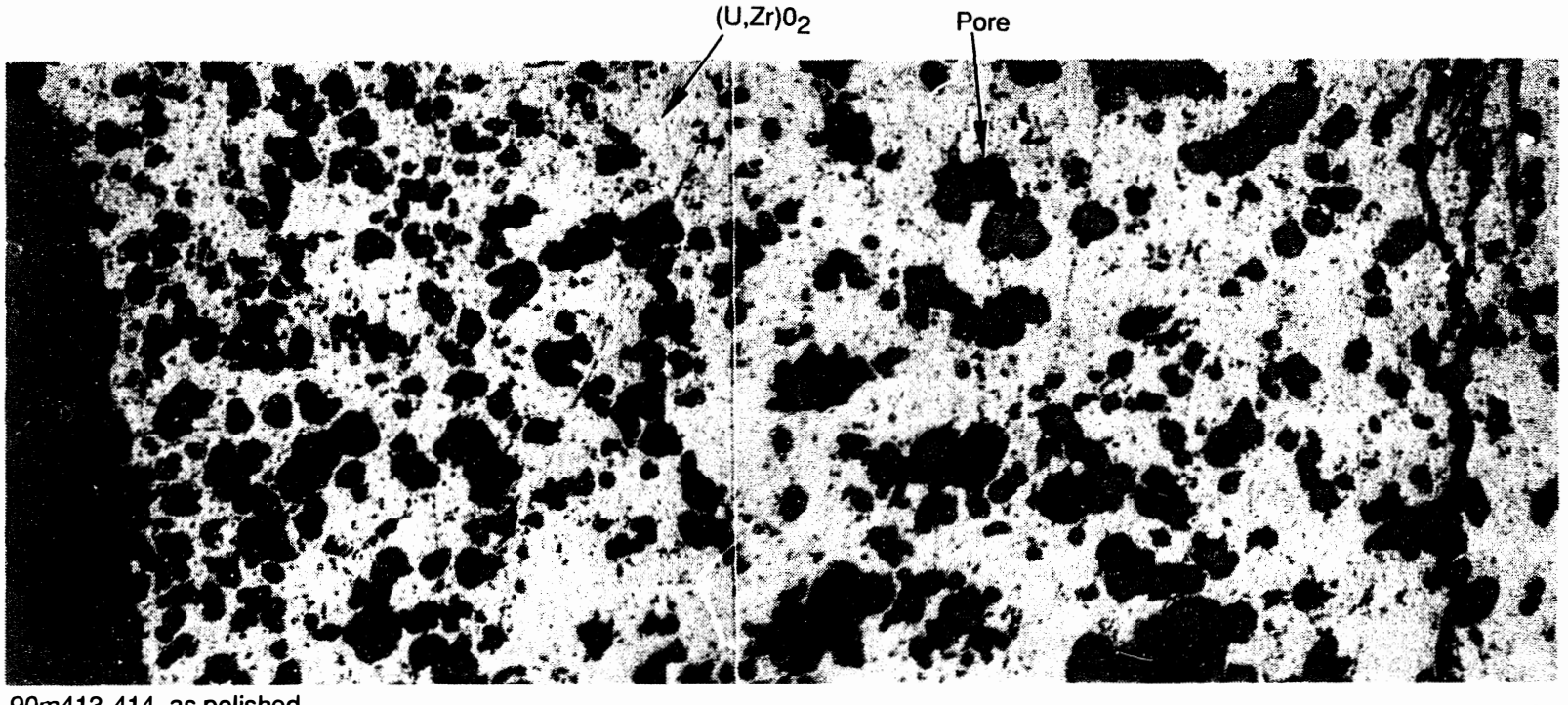

Figure 33. Typical microstructure of 1-9-F.

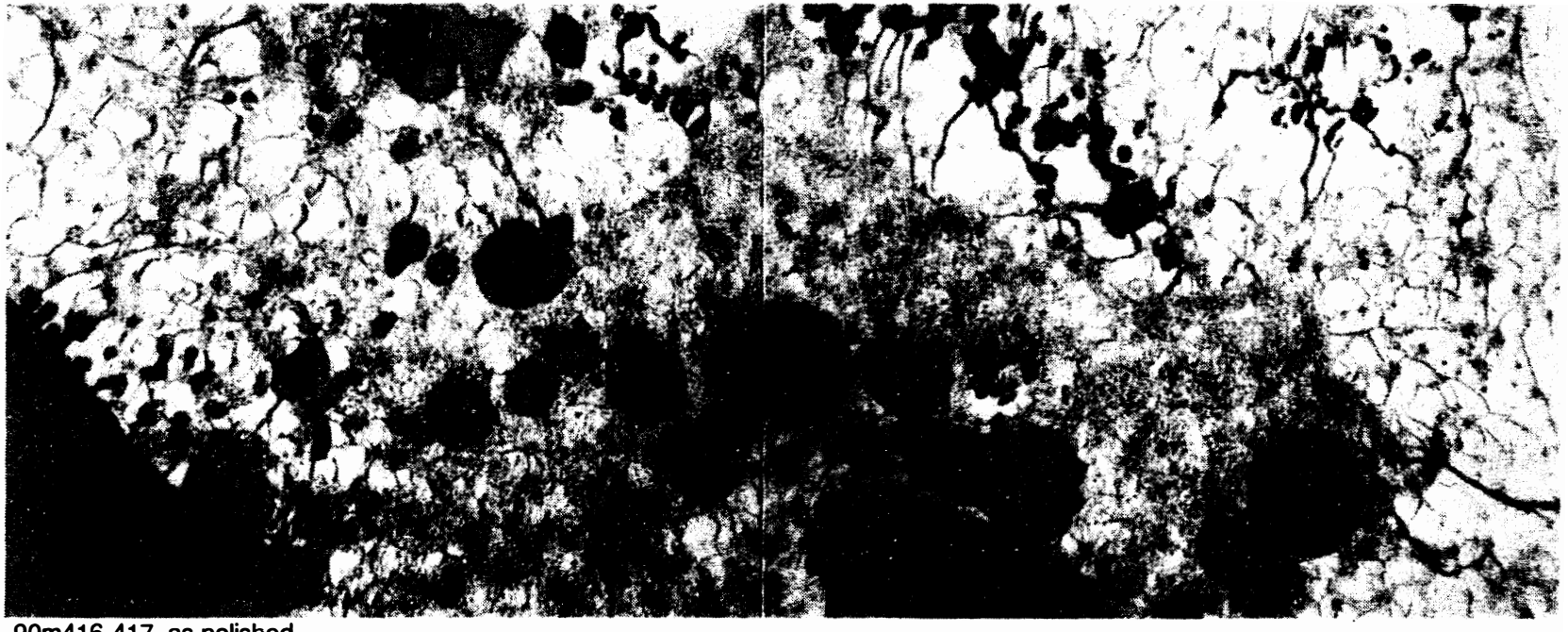

Figure 34. Typical microstructure of 1-9-G.

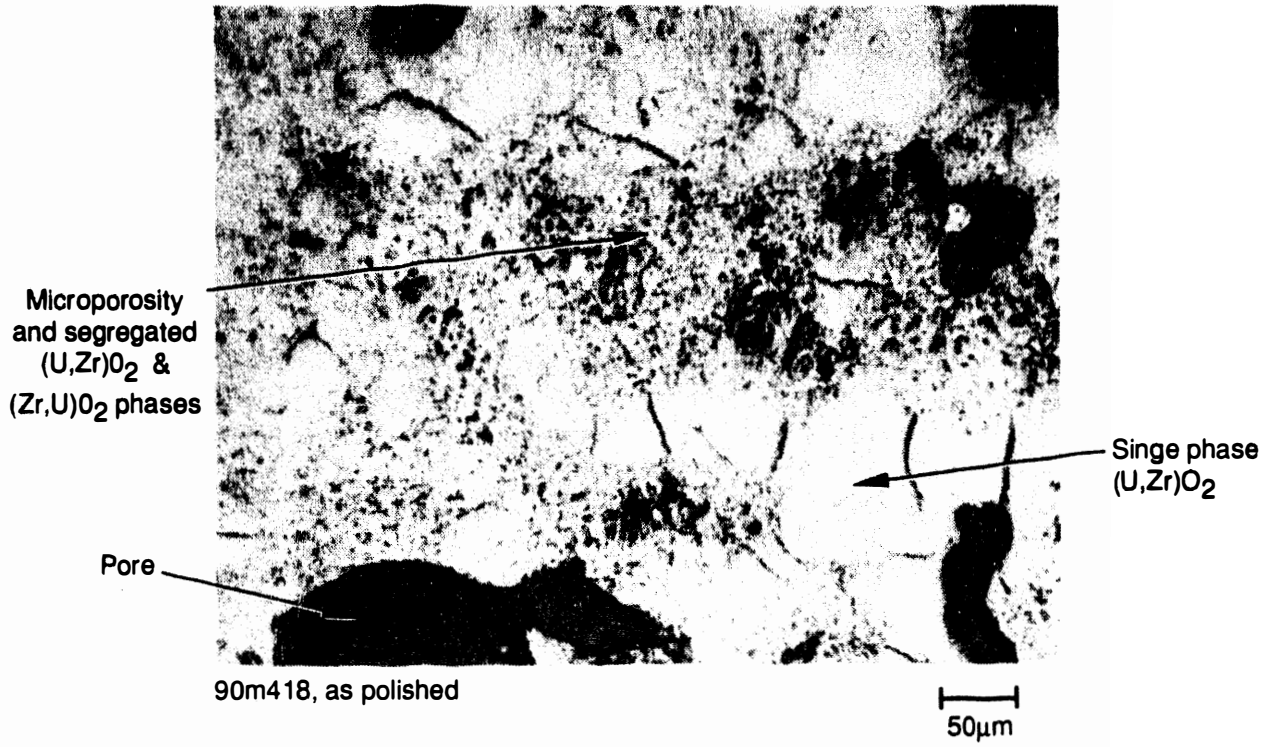

Figure 35. Details of typical microstructure in ceramic melt.

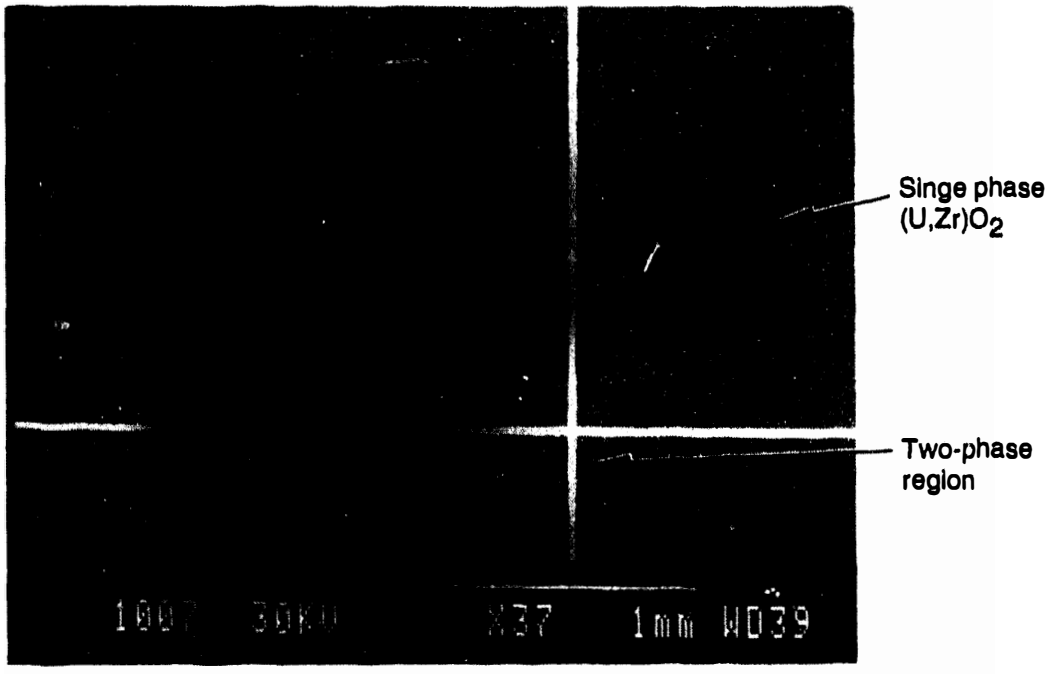

Figure 36. Location of scanning electron microscope backscattered image (1-9-A, Area 2).

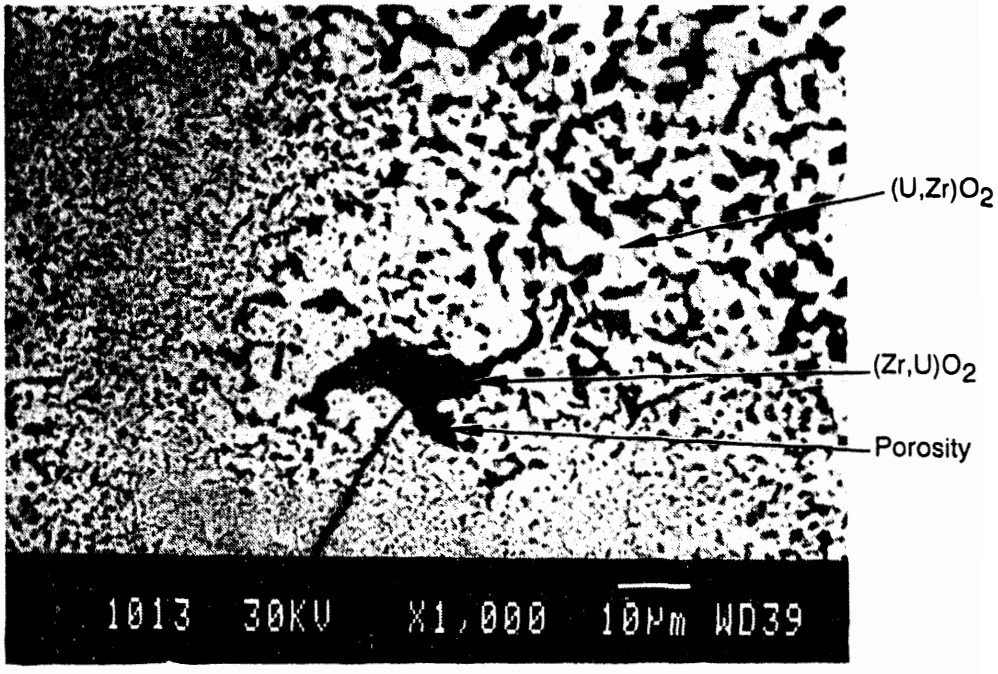

Figure 37. SEM backscattered electron image of two phase region (1-9-A, Area 2).

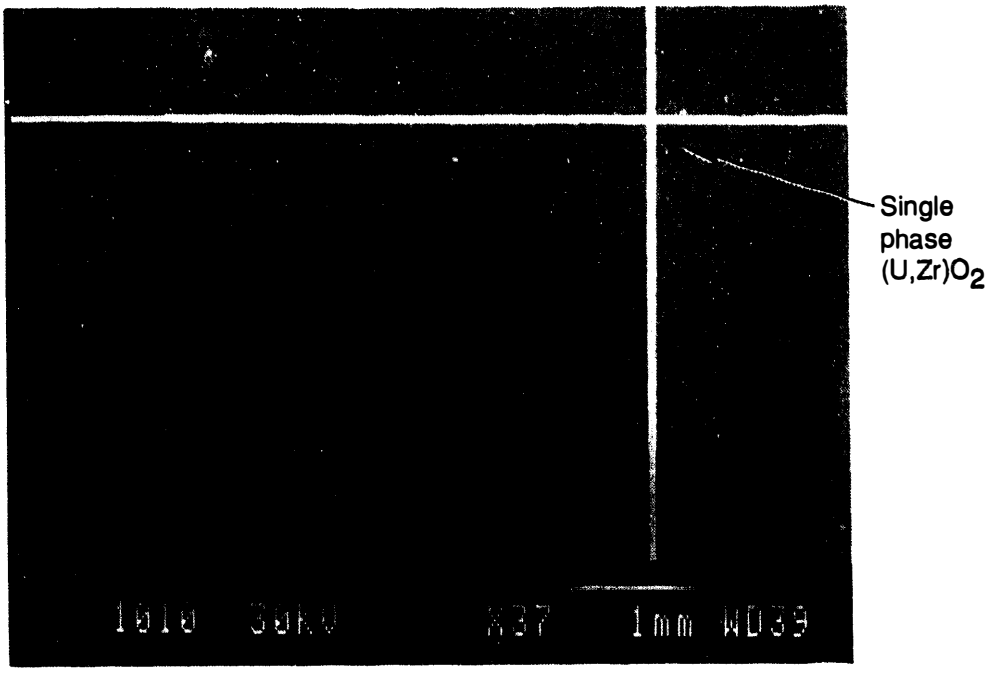

Figure 38. Location of SEM backscattered electron image (1-9-A, Area 5).

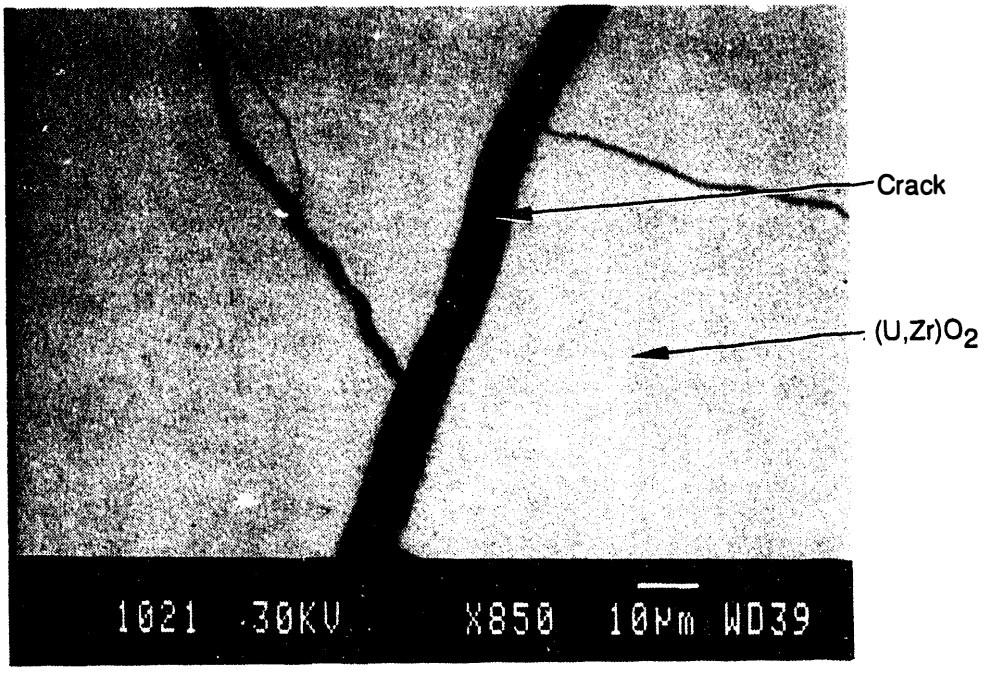

Figure 39. SEM backscattered electron image of single phase region (1-9-A, Area 5).

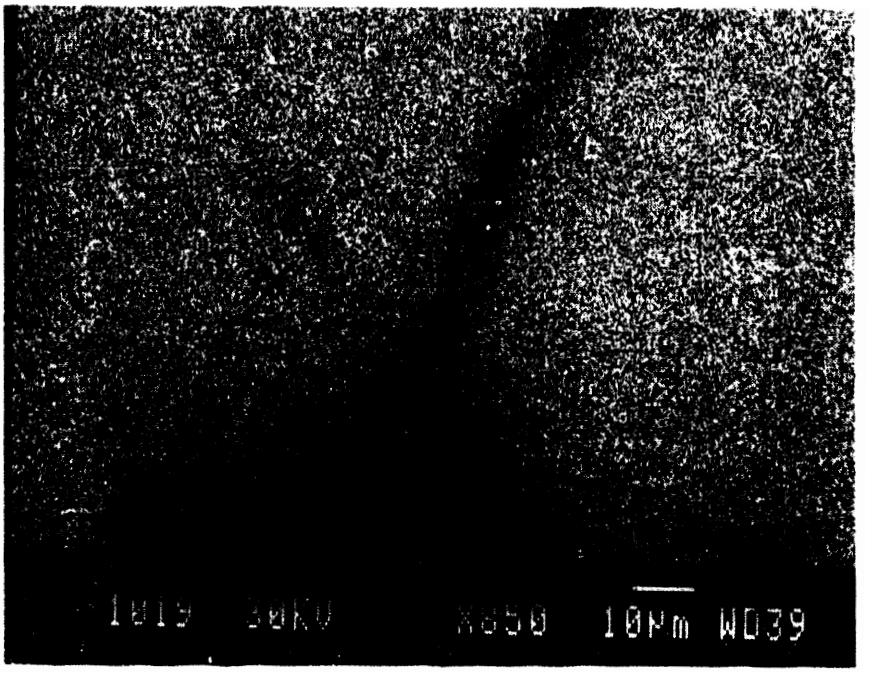

Figure 40. Elemental dot map for uranium (1-9-A, Area 5).

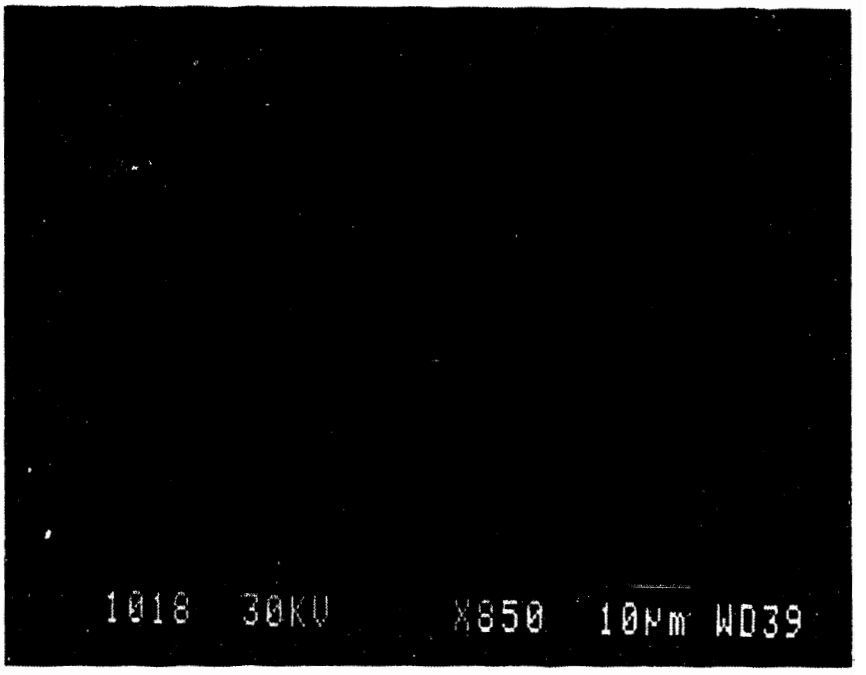

Figure 41. Elemental dot map for zirconium (1-9-A, Area 5).

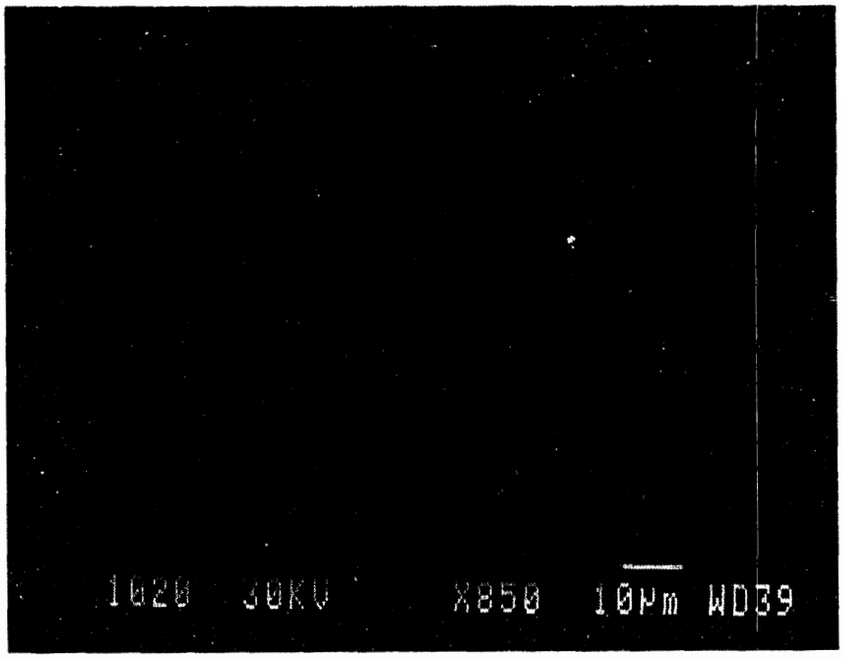

Figure 42. Elemental dot map for oxygen (1-9-A, Area 5).

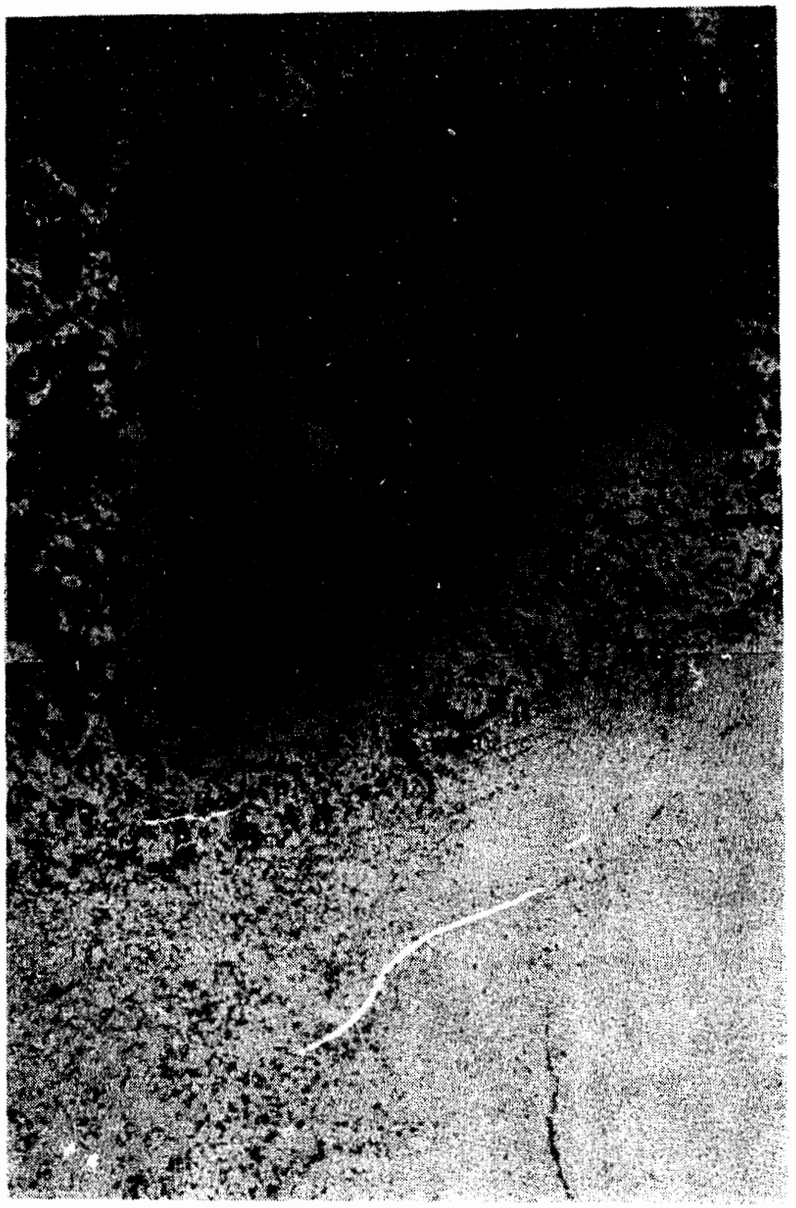

90m173-174, as polished

50μm

Figure 43. Molten edge of sample 1-9-B1 .

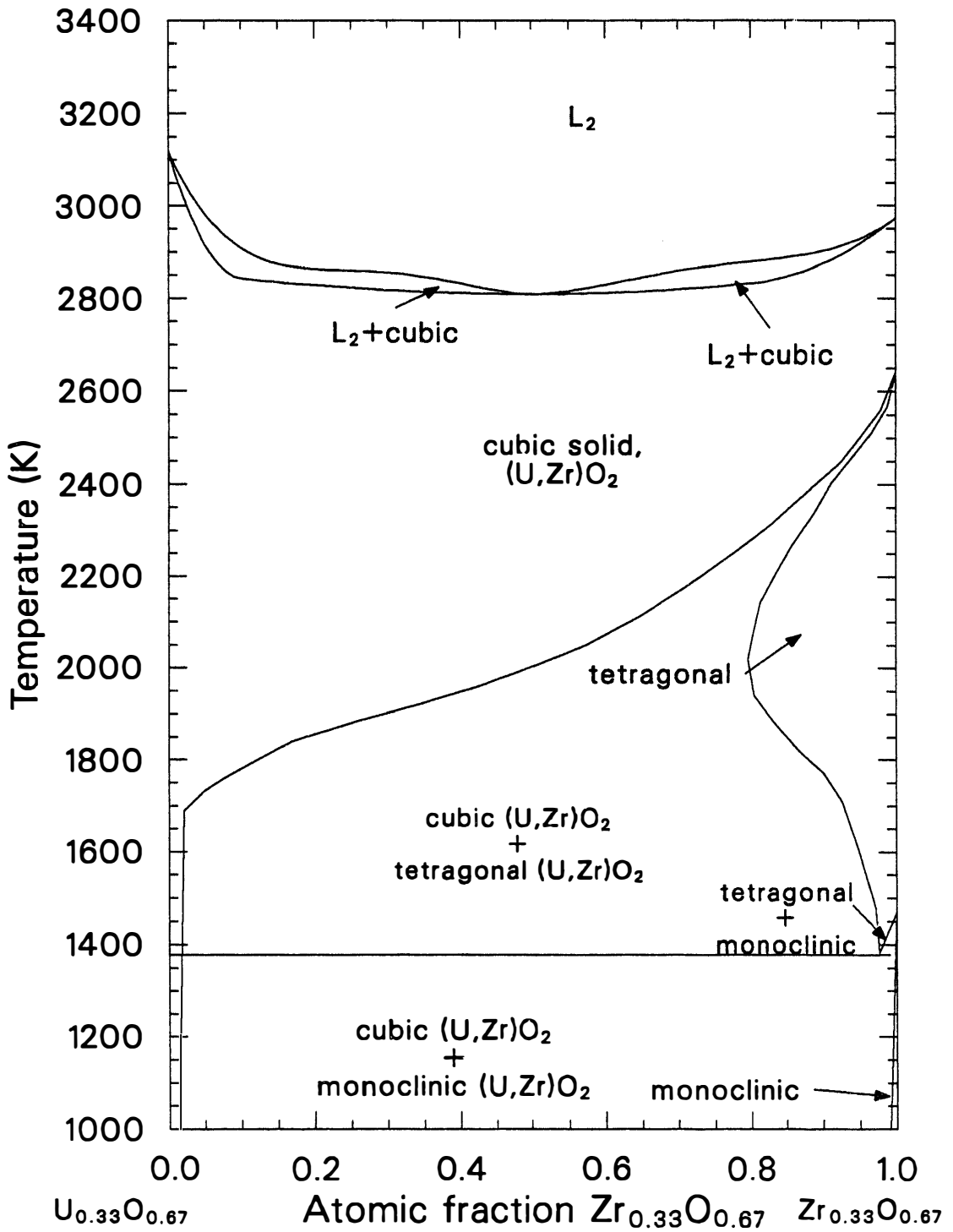

Figure 44. UO_2-ZrO_2 pseudobinary phase diagram.

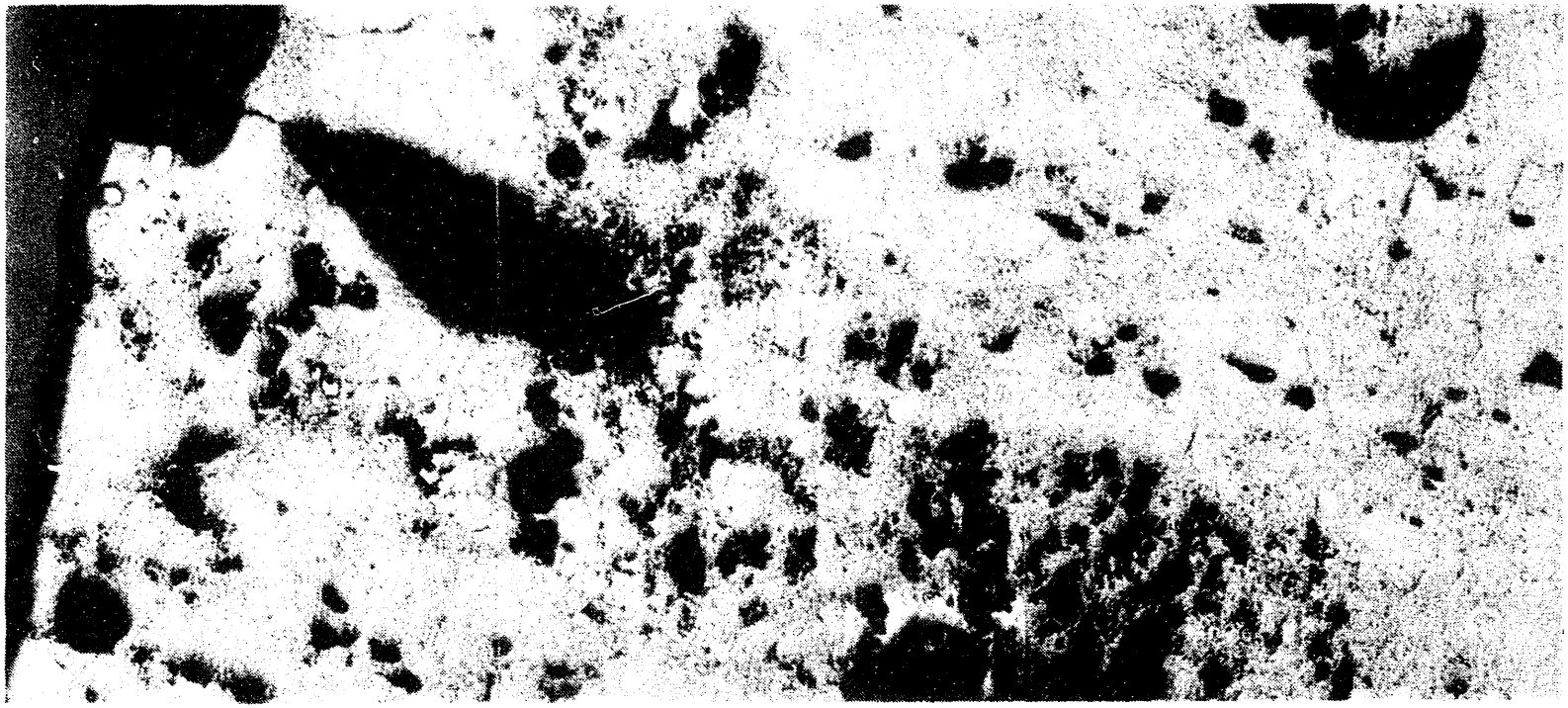

90m190-192, as polished

200µm

Figure 45. Typical microstructure in 1-11-L .

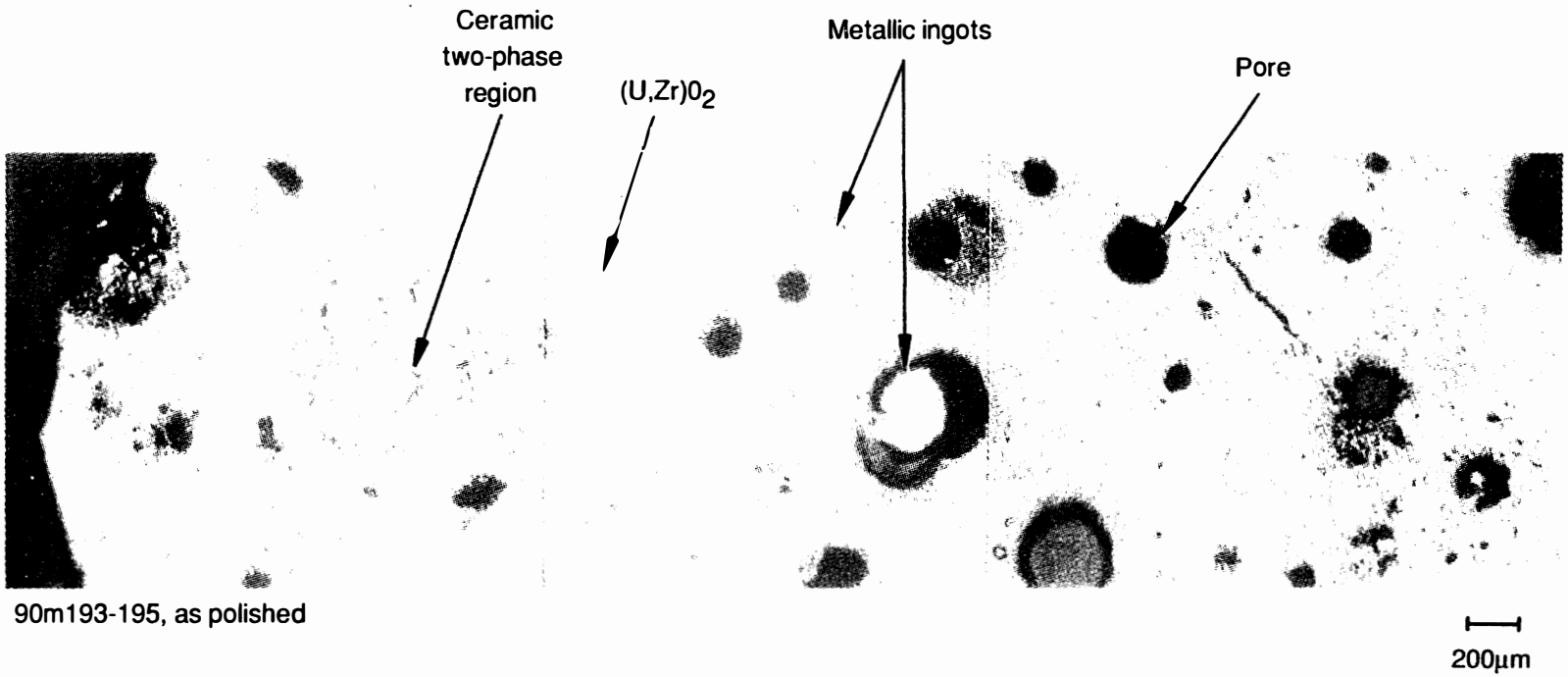

Figure 46. Typical microstructure in 1-11-T.

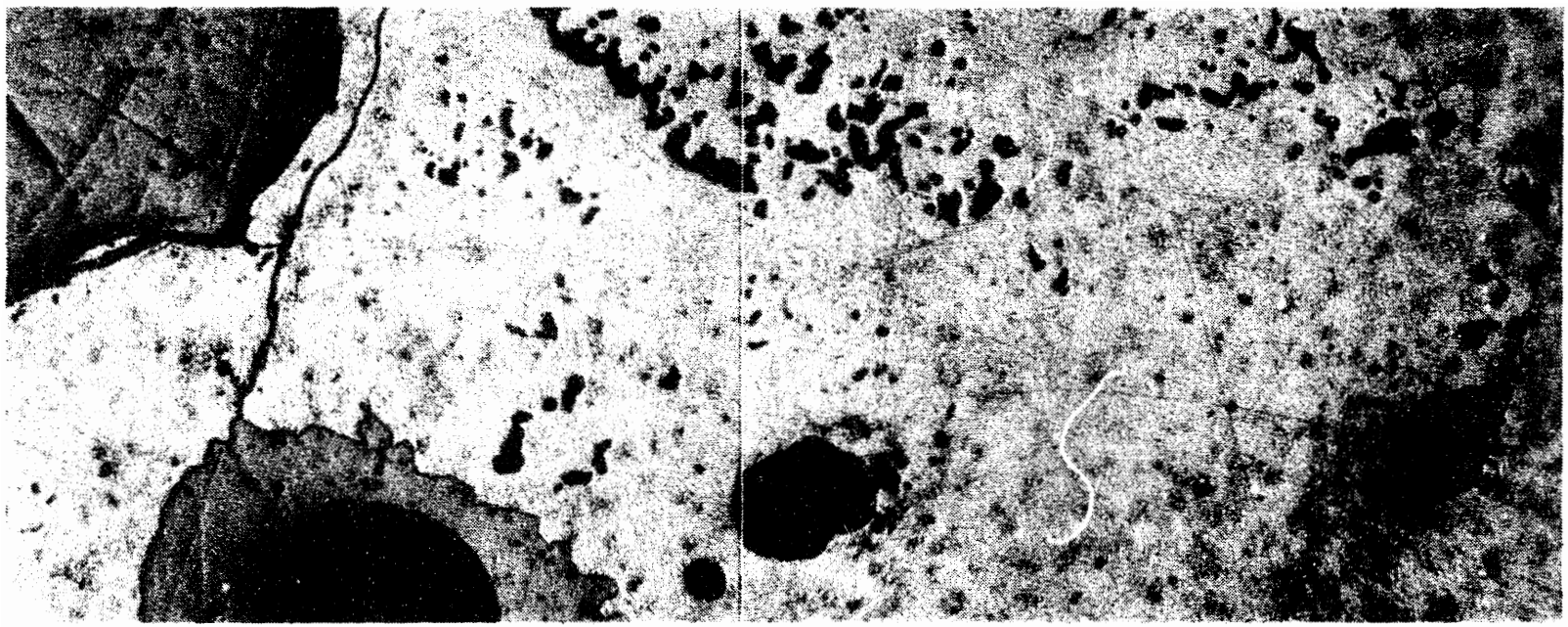

Figure 47. Typical microstructure in 1-11-C.

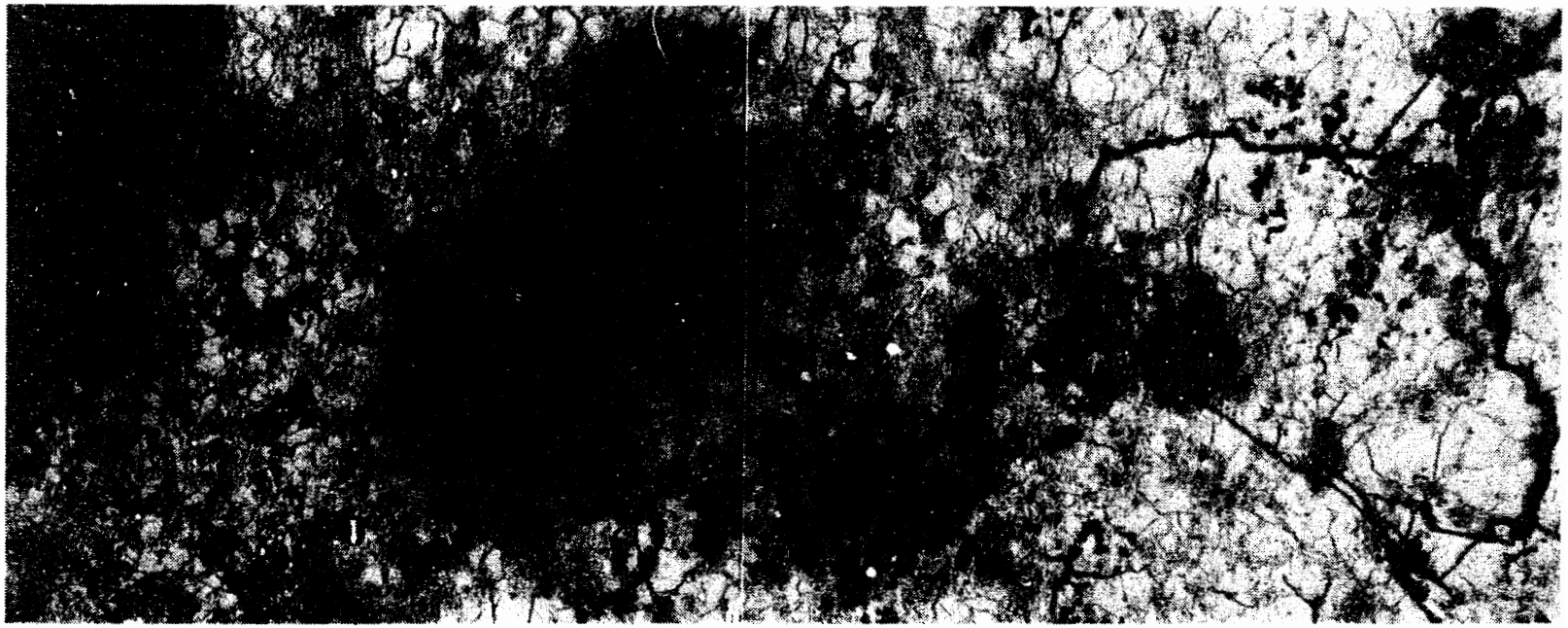

90m422-423, as polished

200µm

Figure 48. Typical microstructure in 1-11D-A.

90m425-426, as polished

200μm

Figure 49. Typical microstructure in 1-11D-B.

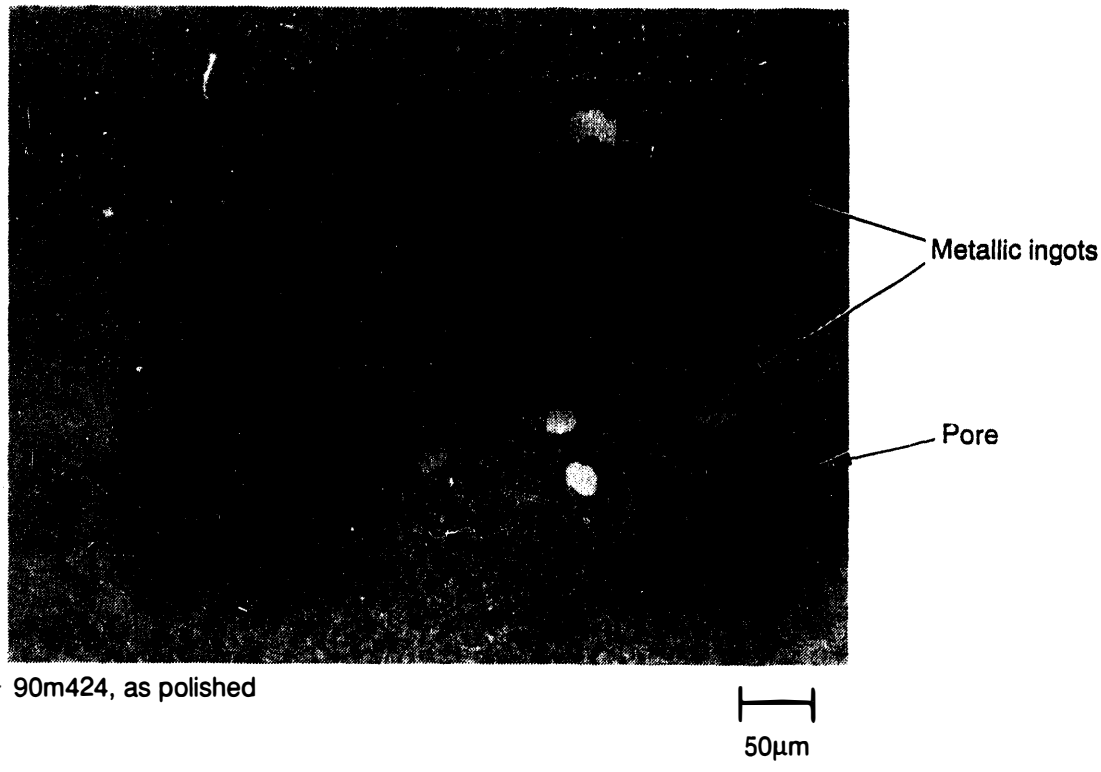

Figure 50. Metallic ingots in ceramic (U, Zr)0_2 matrix.

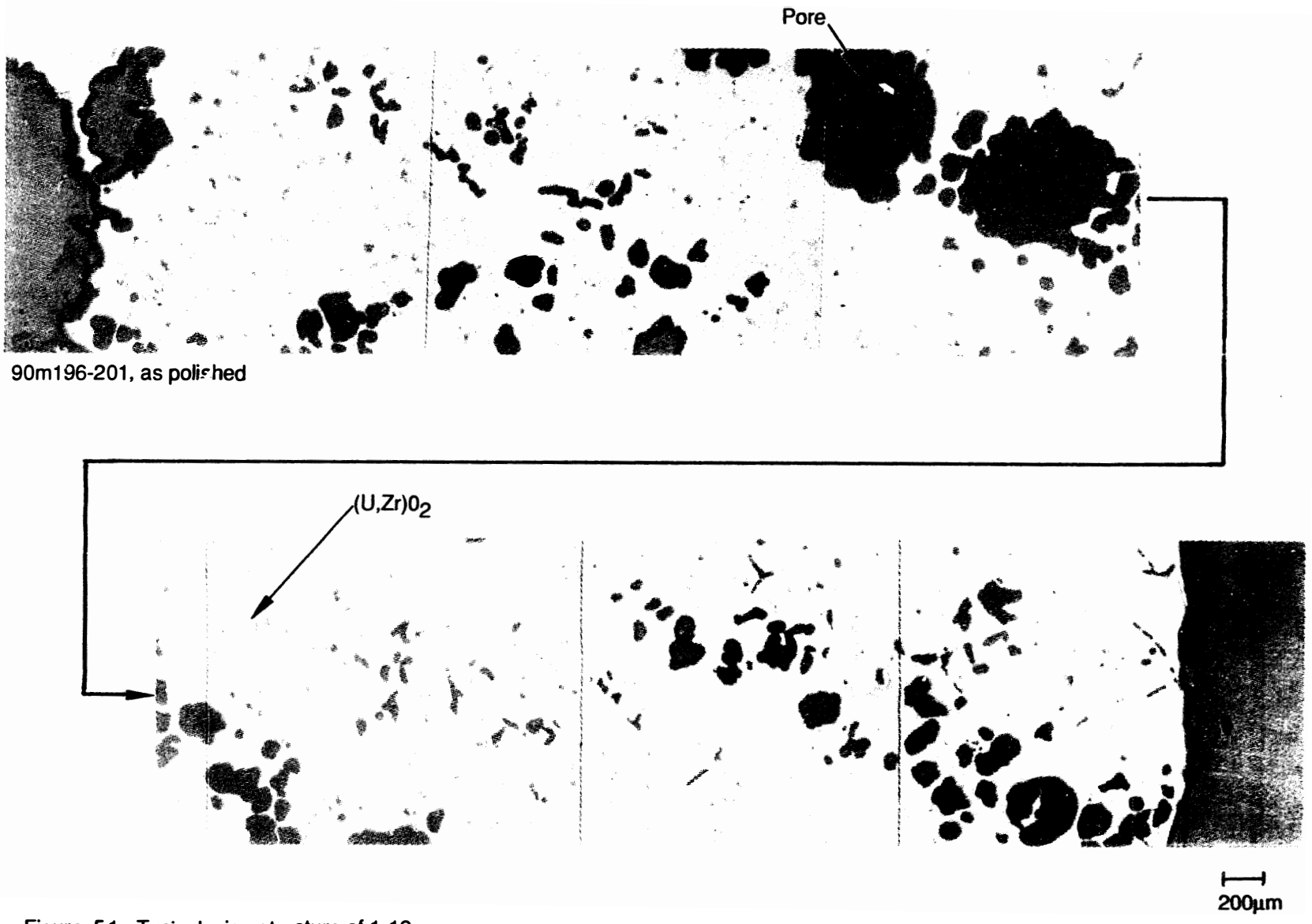

Figure 51. Typical microstructure of 1-12.

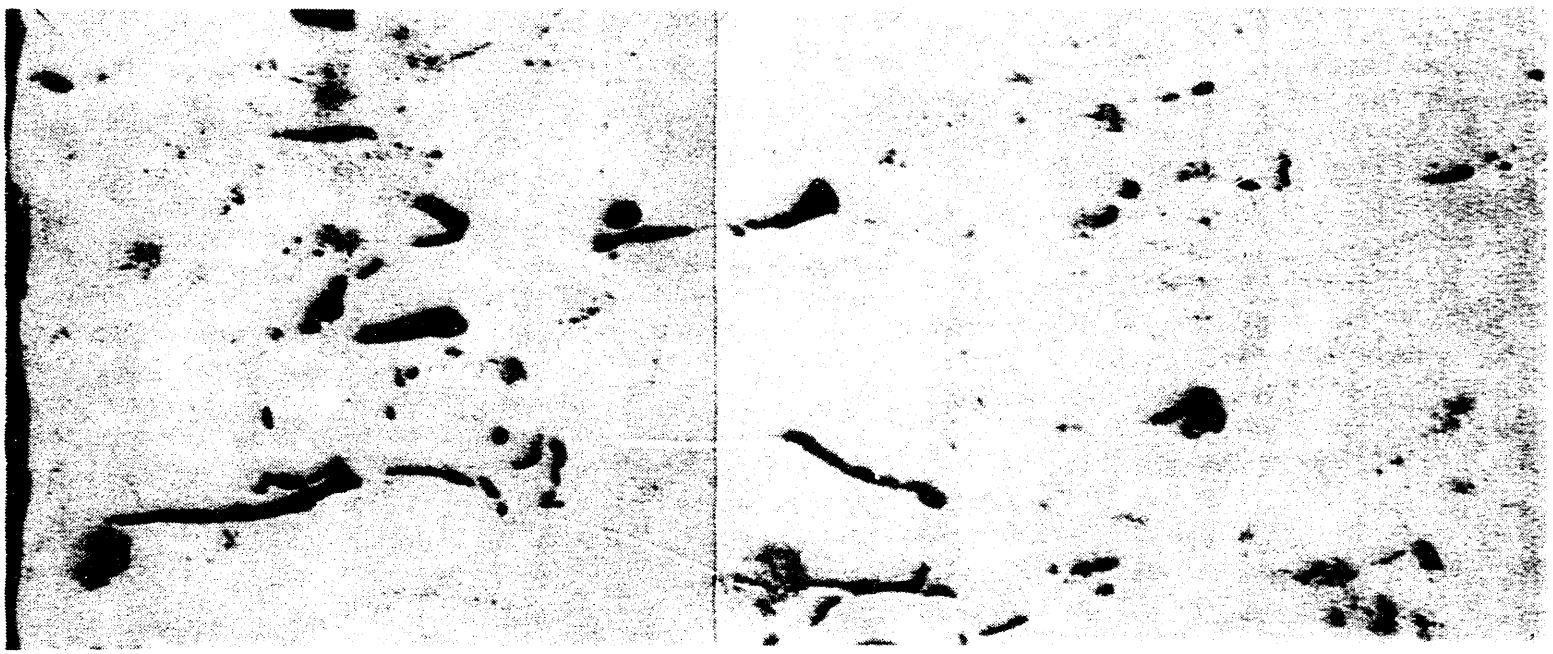

Figure 52. Typical microstructure of 1-12-C.

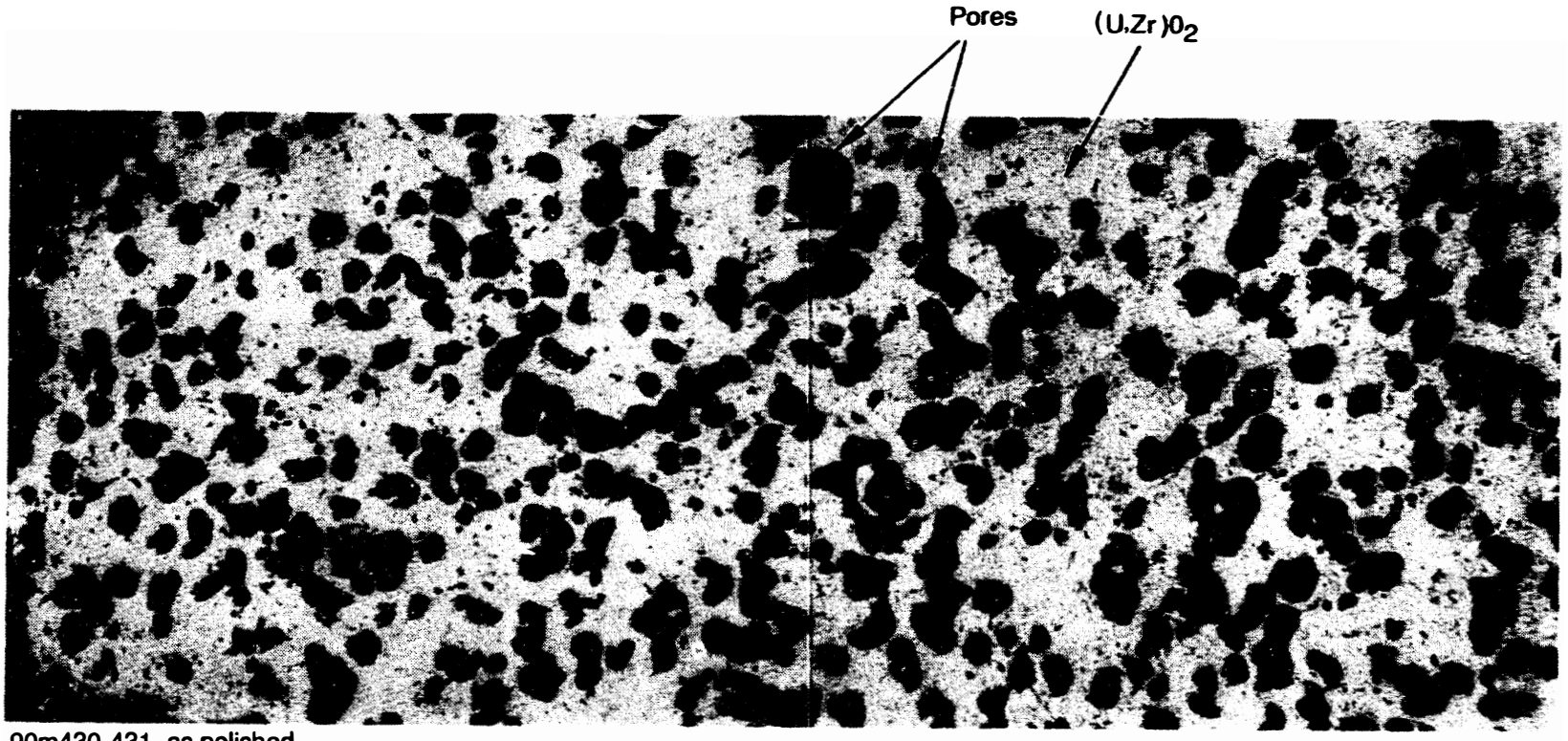

Figure 53. Typical microstructure of 1-12-D.

Appendix A

SEM Examination Results

FIGURES

Appendix A

SEM Examination Results

Examination of Figure A-1 for sample 1-11-T indicates that five regions of interest were examined. They include the edge of a large pore, a small pore with a metallic inclusion, a mottled secondary phase, an apparent inclusion in the melt, and a pore without any secondary phase present. Examination of the dot maps of the large pore, region of interest (ROI) #1, indicates that the sample is composed of $(U,Zr)O_2$ with the presence of some Al, Mg, Sb, and Sn in the matrix. In addition, Figure A-8 and the ROI #1 dot maps (Figures A-9 through A-17) indicate the presence of oxidized Fe and Cr inclusions in the matrix. These results suggest that the Fe and Cr are probably the remains of nozzle material that did not have sufficient time to be distributed evenly in the melt. However, as discussed in Section 4.4, constituents other than U and Zr are present at only trace concentrations in the melt.

Figures A-18 through A-28 show ROI #2 from sample 1-11-T. The composition of the matrix of this sample is similar to ROI #1. The primary difference is the metallic inclusion in the center of the sample. This metallic inclusion is composed of silver with trace amounts of Zr and other metals present. However, the other constituents of the control rods (In and Cd) are not present. These data suggest that the control rod material had been heated sufficiently to remove the more volatile In and Cd from the Ag.

Figures A-29 through A-39 show ROI #3, a mottled secondary phase at the edge of a pore. Based upon the dot maps for this material, it is composed of a $(U,Zr)O_2$ phase that is rich in oxidized Fe and Cr. This phase probably formed during the relatively slow cooldown of the bulk debris bed. Figures A-40 through A-47 show ROI #4, which is a pore with a secondary phase that appears to contain relatively lesser amounts of U. However, both cases are apparent evidence for the relatively slow cooldown of the debris bed that allows the lower melting point materials to segregate near pores and the probable formation of lower melting temperature eutectics near these pores.

ROI #5 of sample 1-11-T (Figures A-48 through A-57) is a pore that is not surrounded by an apparent secondary phase. However, the dot maps for this sample indicate the presence of Fe,

Cr, and Ag around the periphery of the pore, and the oxygen analysis results suggest that the Ag is oxidized; however, further confirmation is required to indicate that the oxidation potentials were sufficiently high to oxidize Ag during the accident.

Figure A-58 shows sample 1-9-A, and Figure A-59 shows the first region of interest examined, which is a mottled region containing both high and low atomic number material. The dot maps of this region (Figures A-63 through A-68) indicate that the mottling is again due to the presence of Fe, Cr, and some other metals. Again, the presence of these metals is probably due to the melting of structural materials during the relocation event.

The second region of sample 1-9-A that was examined (Figures A-69 through A-77) is a relatively homogeneous phase containing U and Zr with possibly a small amount Ni present.

Figure A-78 shows sample 1-9-B, and Figure A-79 shows the edge of a pore in this sample. The dot maps for this region (Figures A-83 through 92) again show a relatively homogeneous $(U,Zr)O_2$ phase with the presence of some Fe and Cr. These data again indicate the presence of a relatively homogeneous matrix that may have some Fe and Cr in the matrix or some localized accumulations of this material.

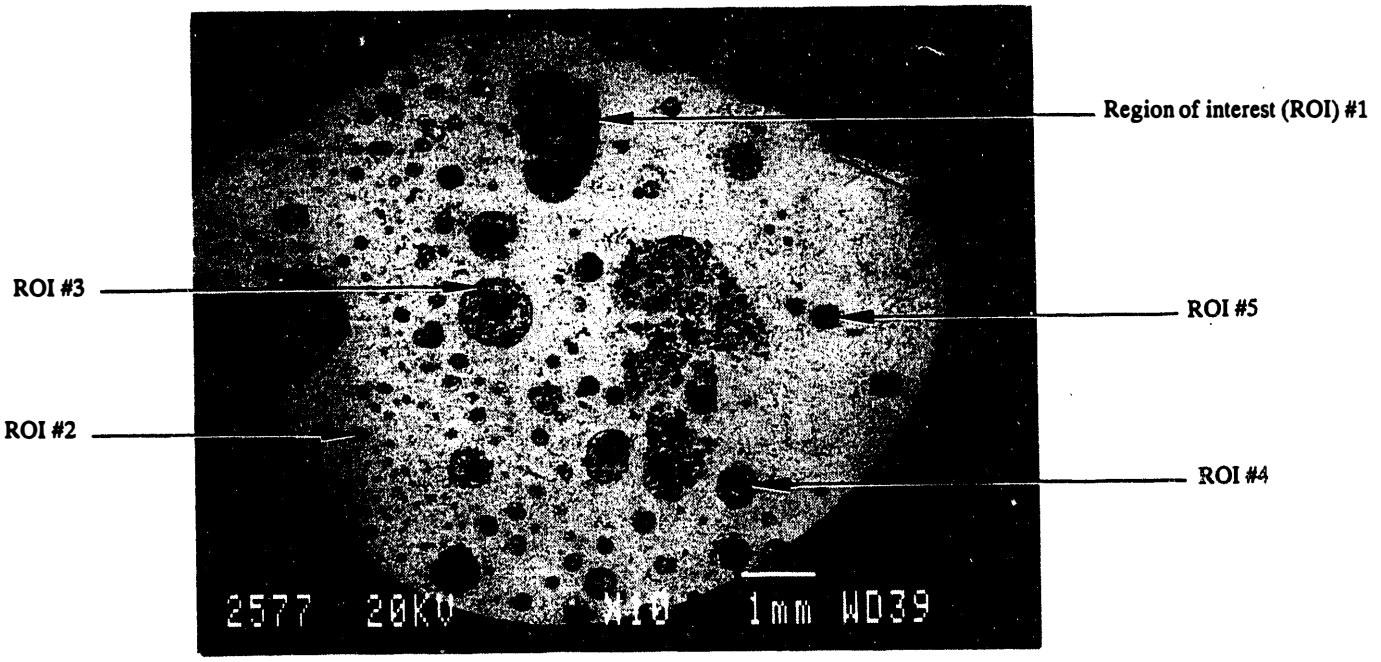

Figure A-1. Sample 1-11-T whole sample secondary electron image (#2577).

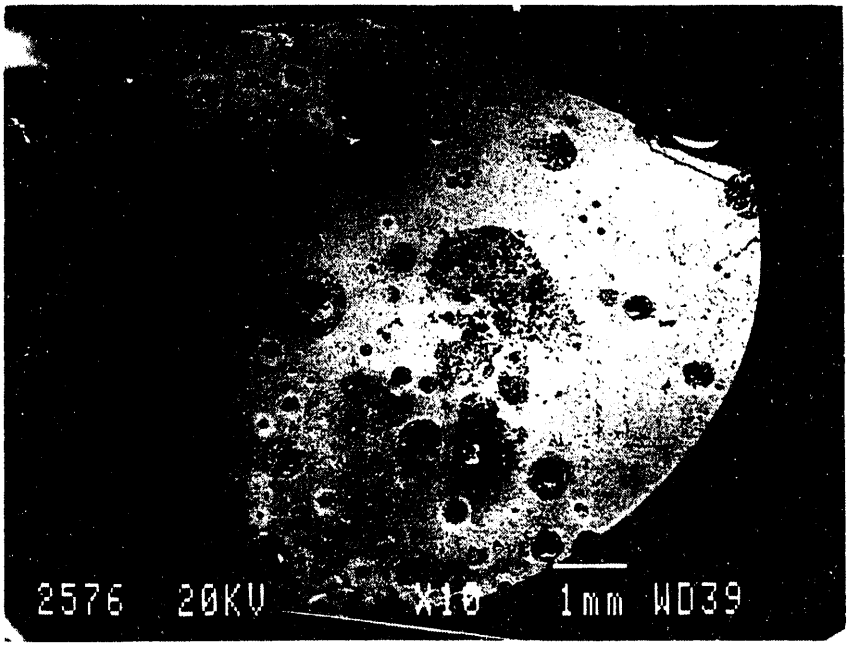

Figure A-2. Sample 1-11-T whole sample topographical (#2576).

Figure A-3. Sample 1-11-T whole normal alignment (area of interest) secondary electron image (#2579).

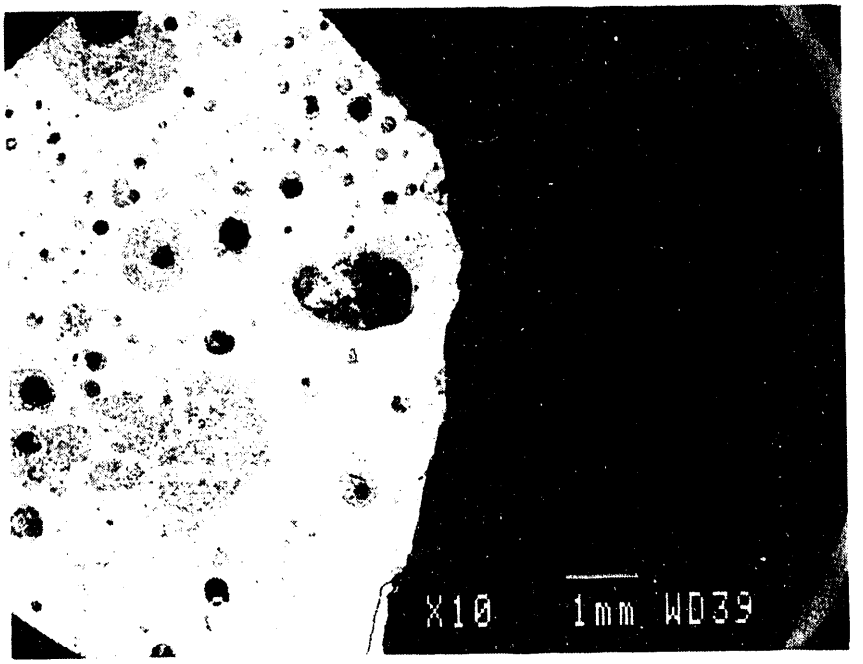

Figure A-4. Sample 1-11-T whole normal alignment (area of interest) compositional (#2581).

Figure A-7. Sample 1-11-T ROI #1 (reduced area of interest) secondary electron image (

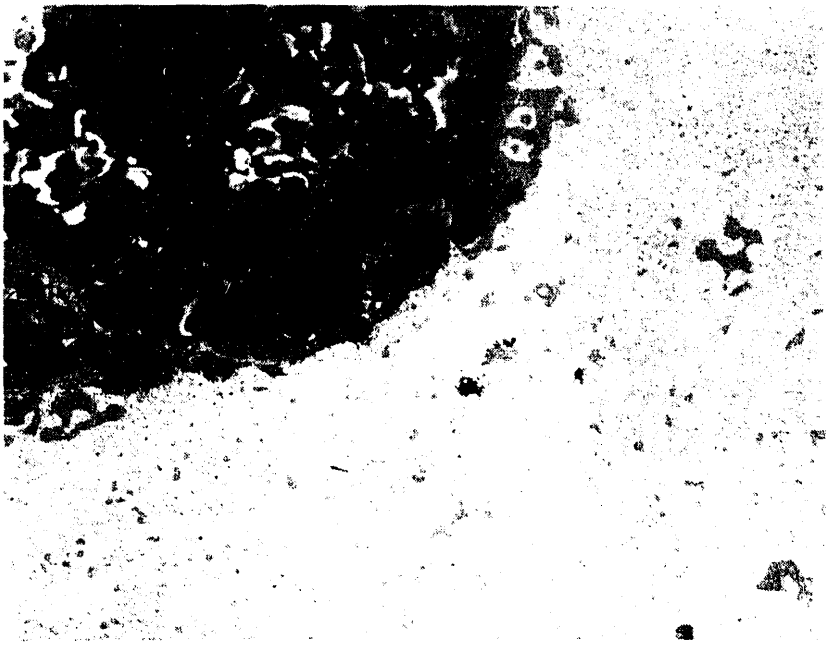

Figure A-8. Sample 1-11-T ROI #1 compositional (#2589).

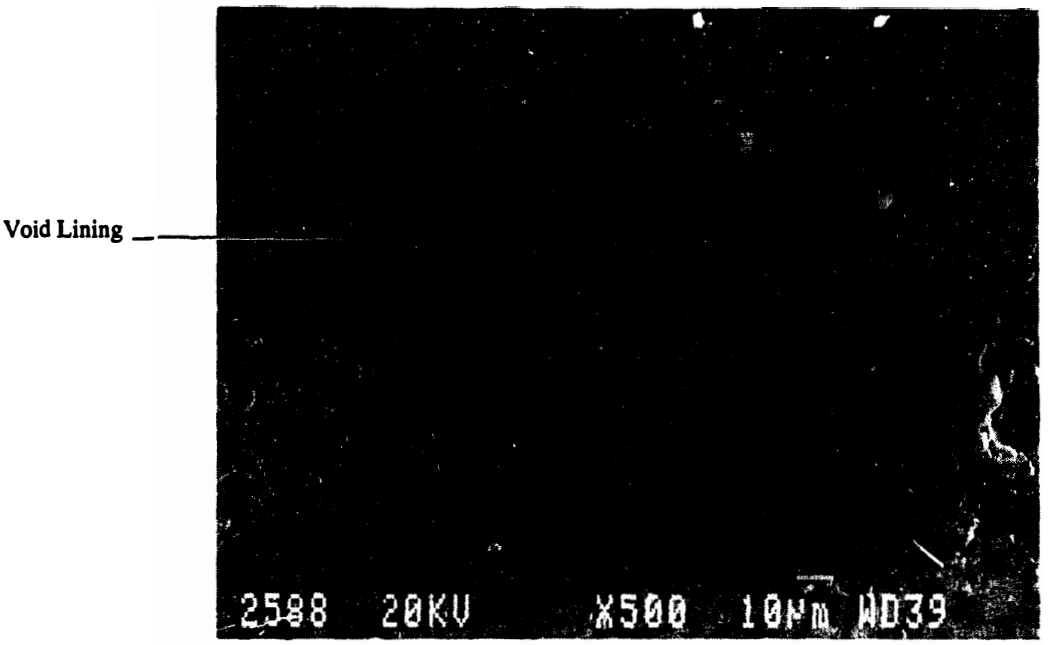

Figure A-7. Sample 1-11-T ROI #1 (reduced area of interest) secondary electron image (#2588).

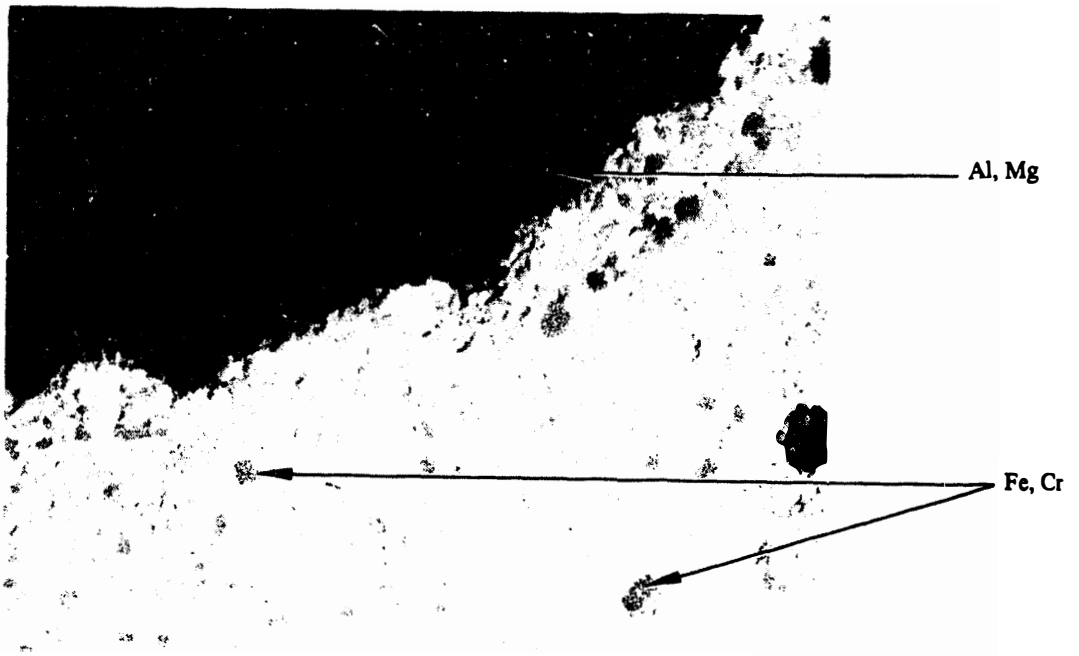

Figure A-8. Sample 1-11-T ROI #1 compositional (#2589).

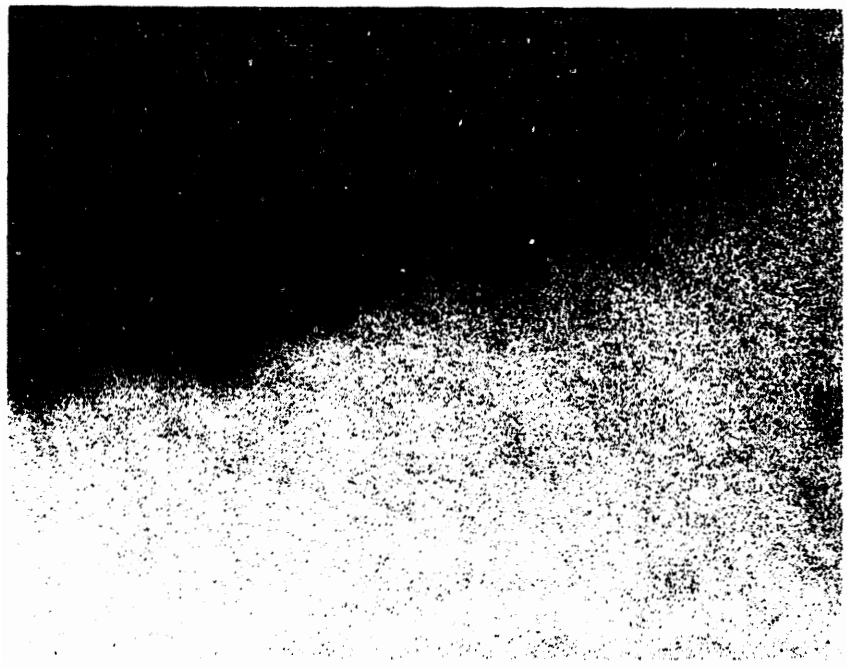

Figure A-9. Sample 1-11-T ROI #1 dot map of U (#2606).

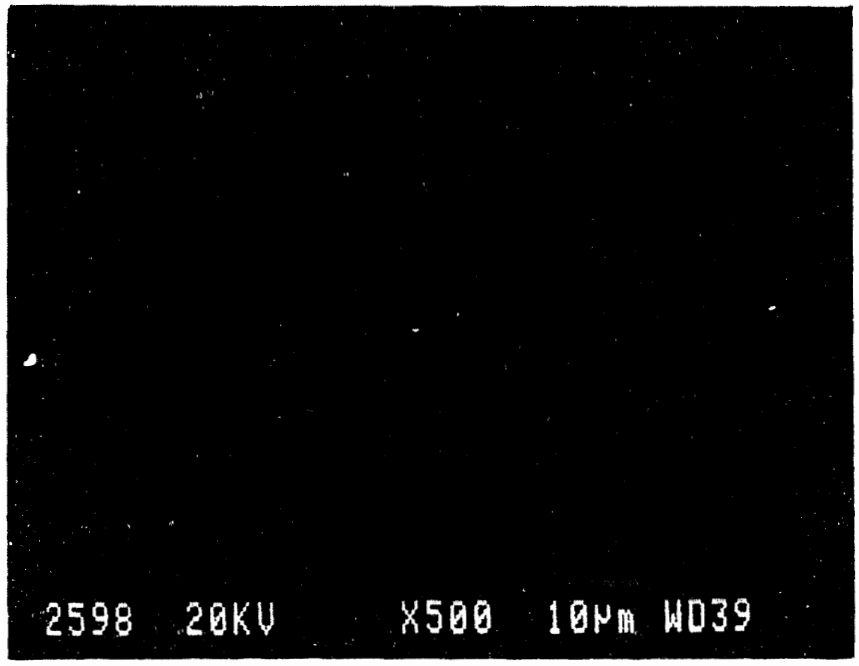

Figure A-10. Sample 1-11-T ROI #1 dot map of O (#2598).

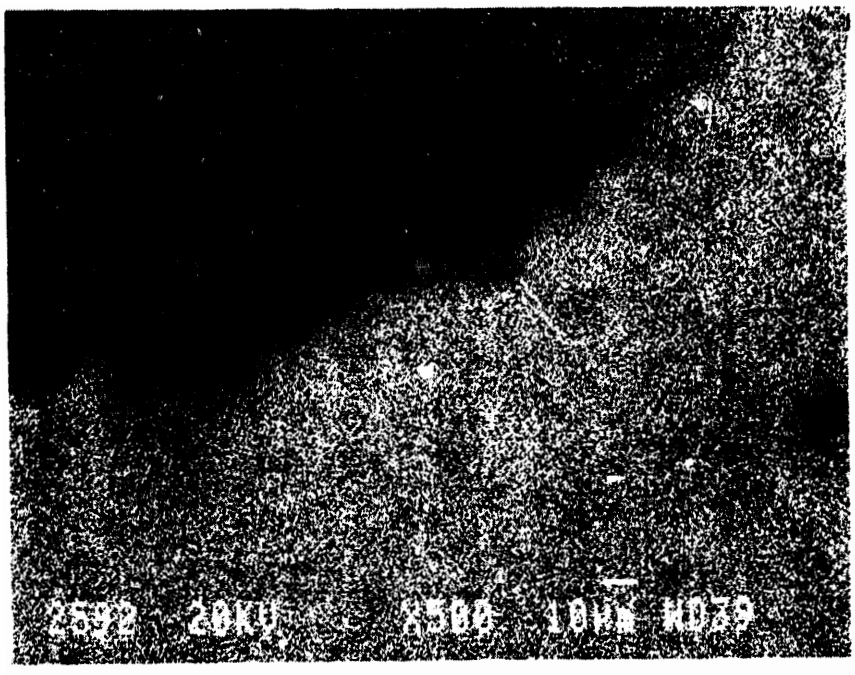

Figure A-11. Sample 1-11-T ROI #1 dot map of Zr (#2592).

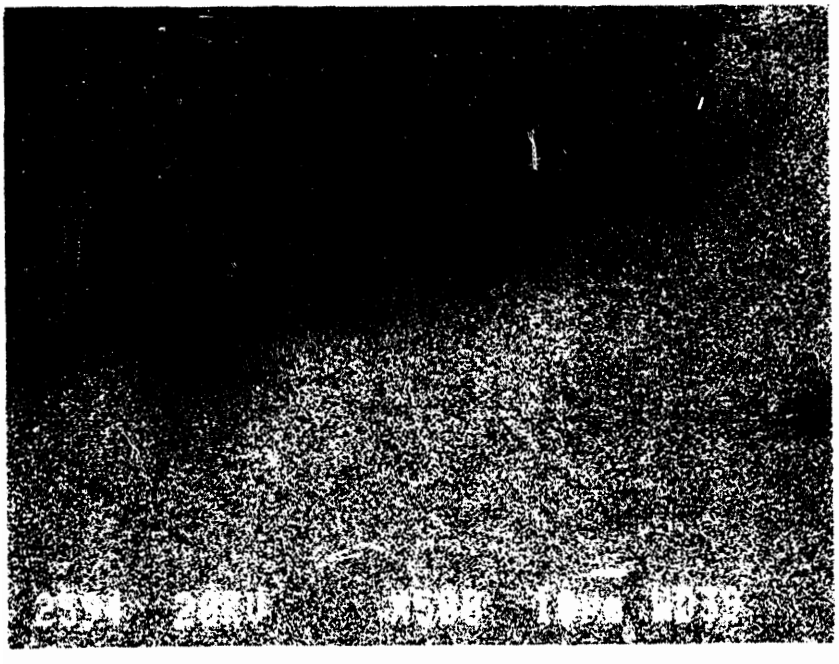

Figure A-12. Sample 1-11-T ROI #1 dot map of Al (#2594).

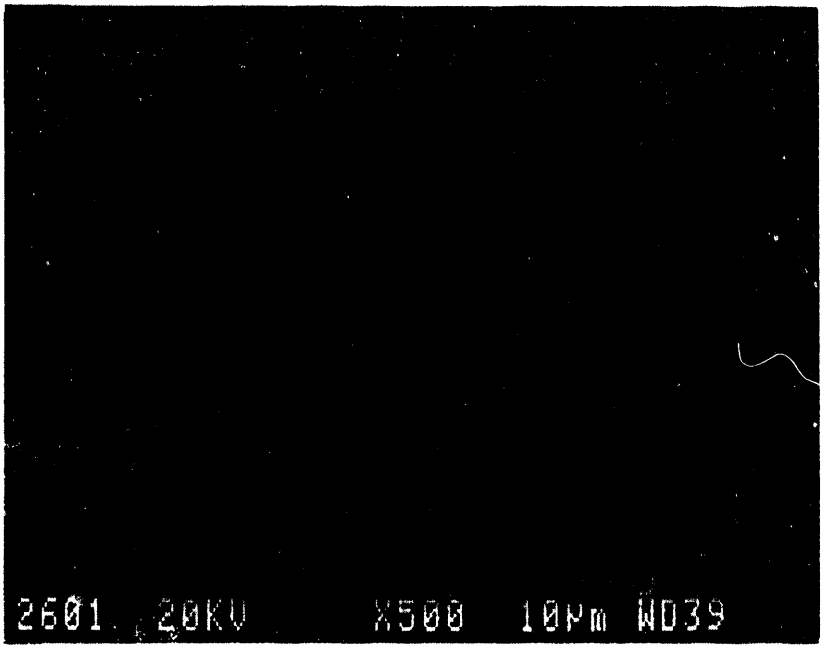

Figure A-13. Sample 1-11-T ROI #1 dot map of Cr (#2601).

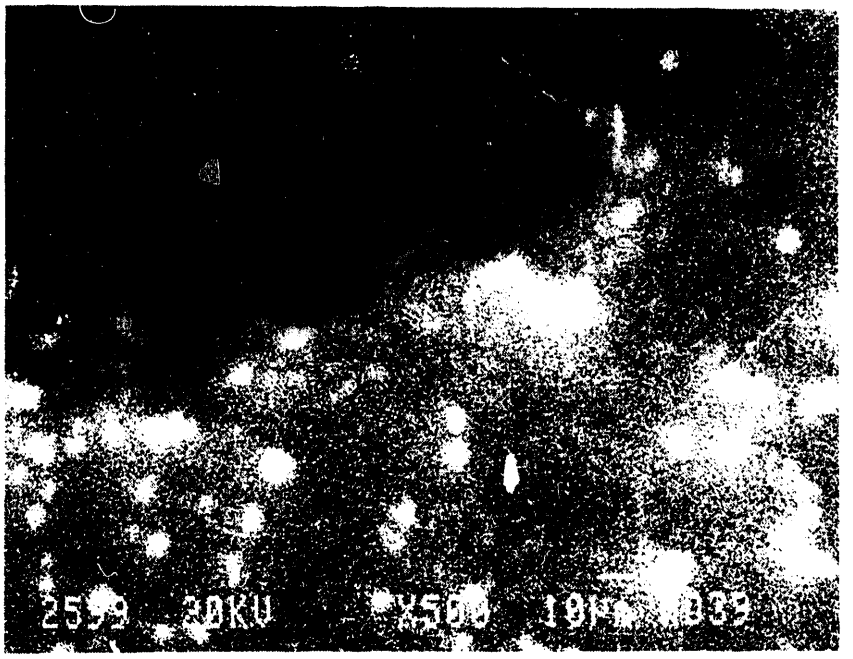

Figure A-14. Sample 1-11-T ROI #1 dot map of Fe (#2599).

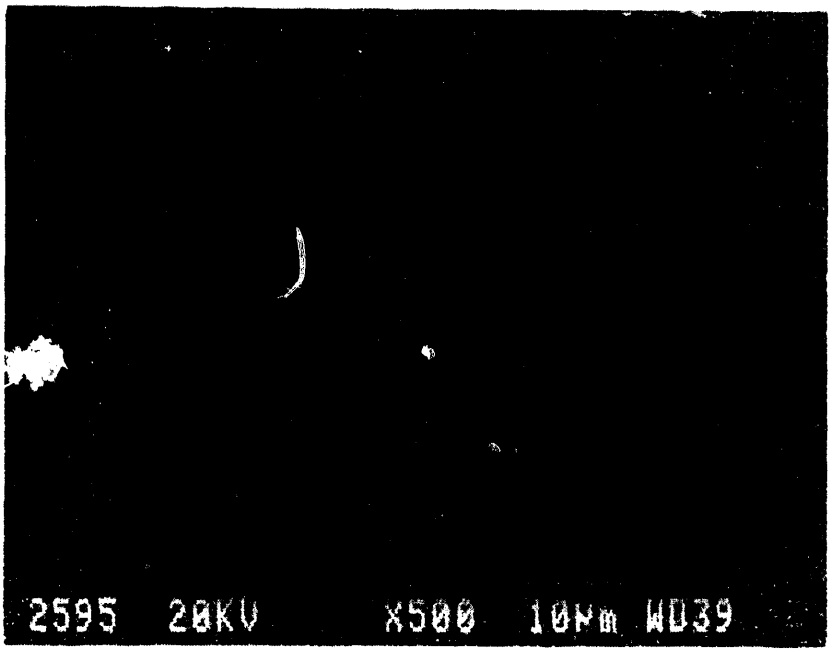

Figure A-15. Sample 1-11-T ROI #1 dot map of Mg (#2595).

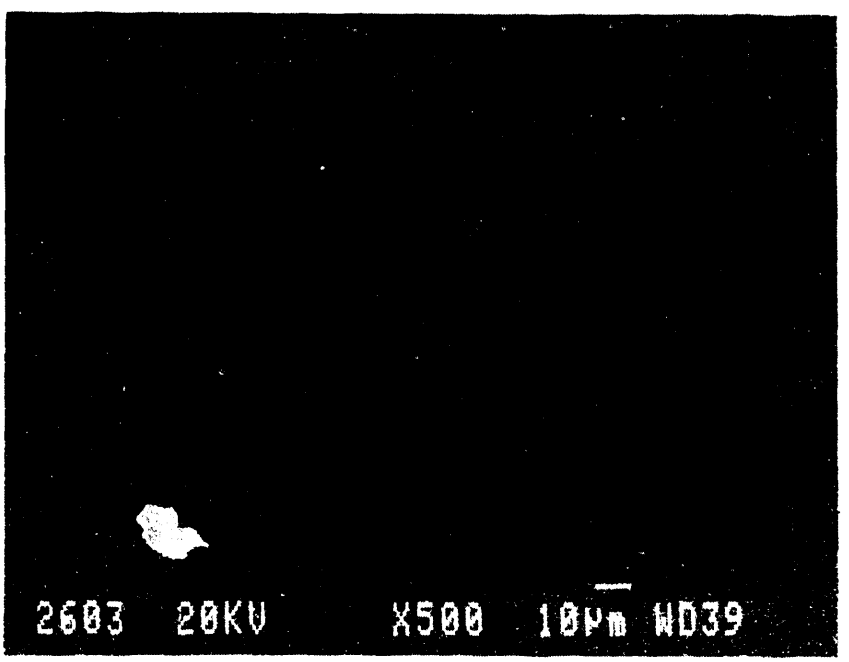

Figure A-16. Sample 1-11-T ROI #1 dot map of Sb (#2603).

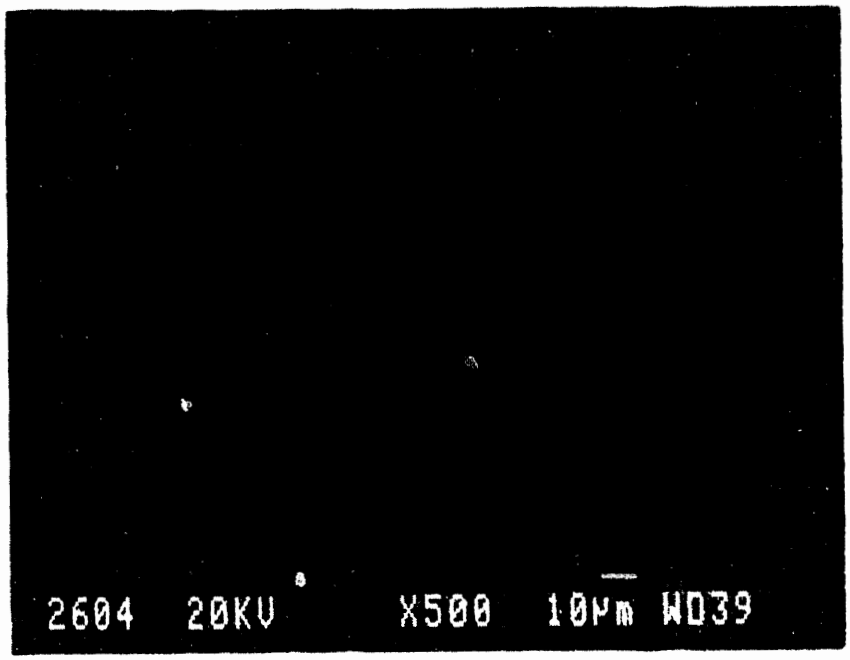

Figure A-17. Sample 1-11-T ROI #1 dot map of Sn (#2604).

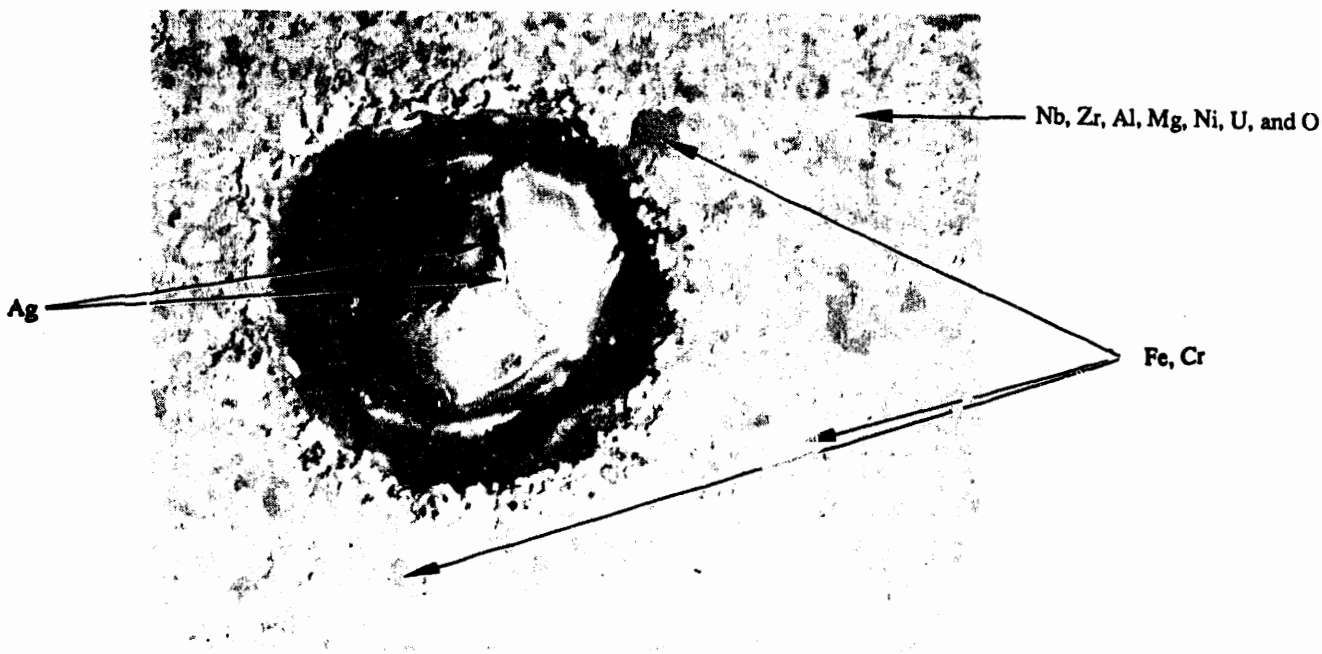

Figure A-18. Sample 1-11-T ROI #2 topographical (#2610).

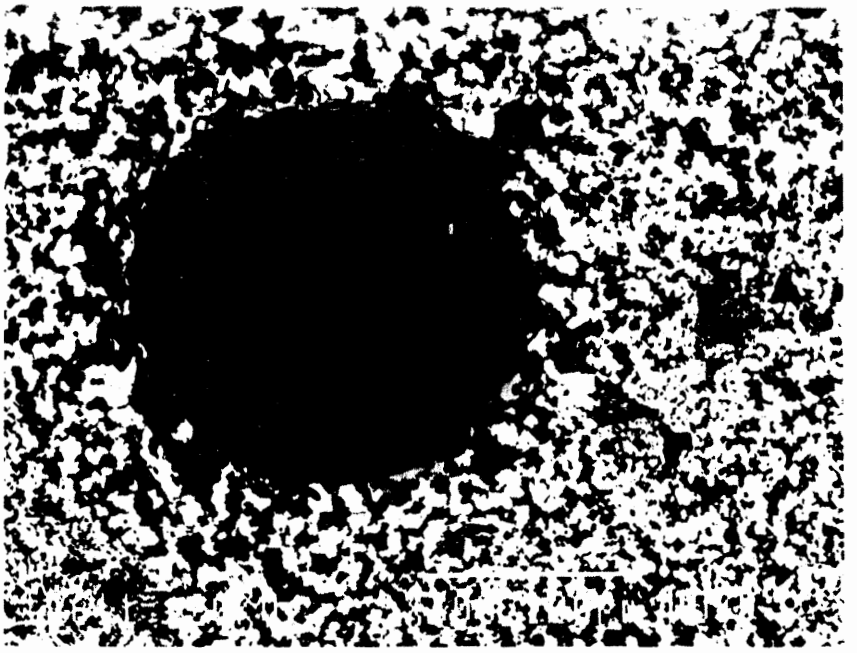

Figure A-19. Sample 1-11-T ROI #2 compositional (#2611).

Figure A-20. Sample 1-11-T ROI #2 dot map of U (#2633).

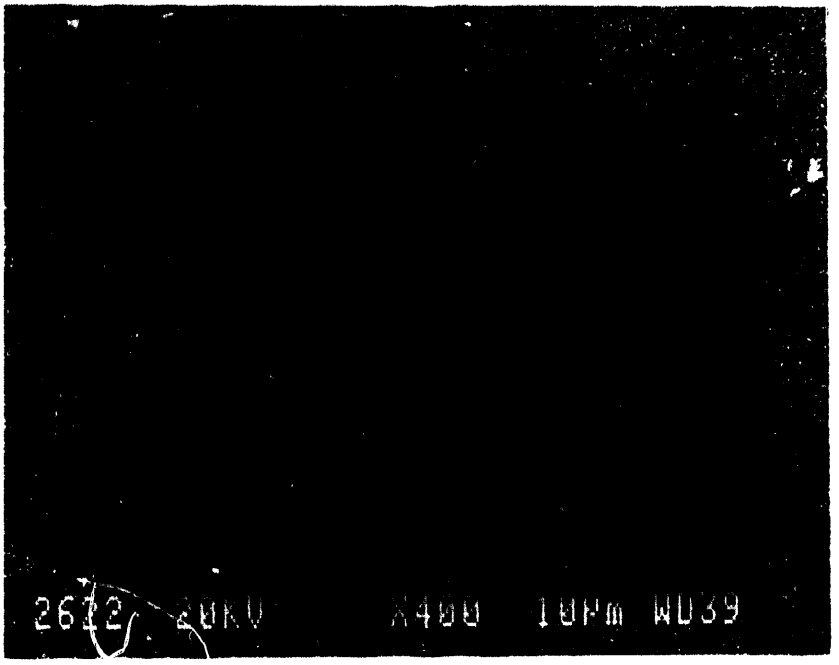

Figure A-21. Sample 1-11-T ROI #2 dot map of Zr (#2622).

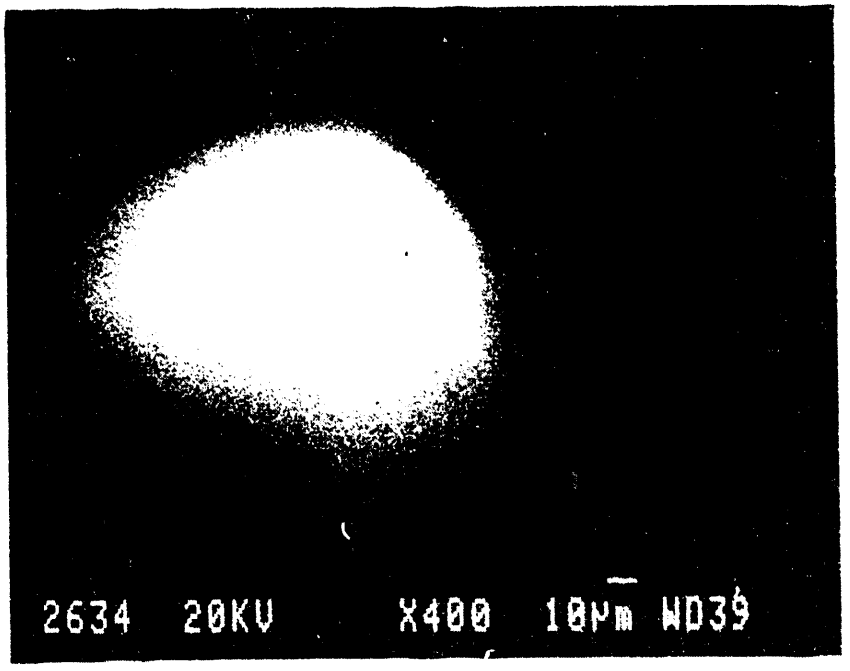

Figure A-22. Sample 1-11-T ROI #2 dot map of Ag (#2634).

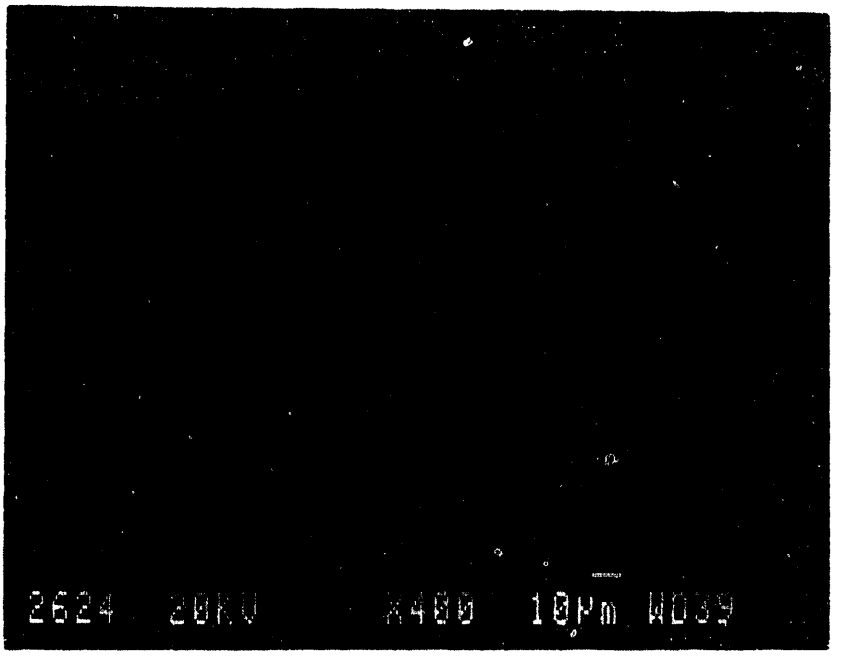

Figure A-23. Sample 1-11-T ROI #2 dot map of Al (#2624).

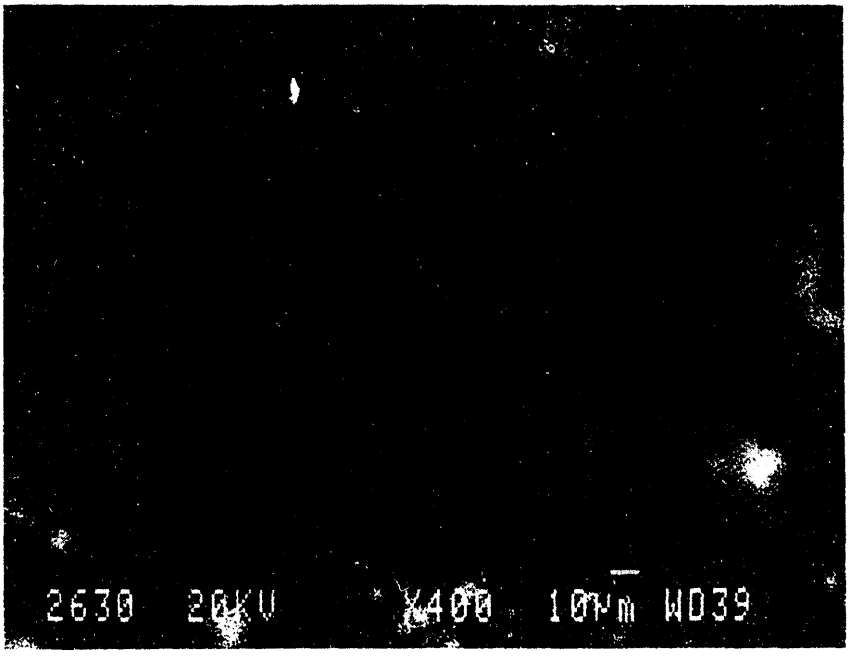

Figure A-24. Sample 1-11-T ROI #2 dot map of Cr (#2630).

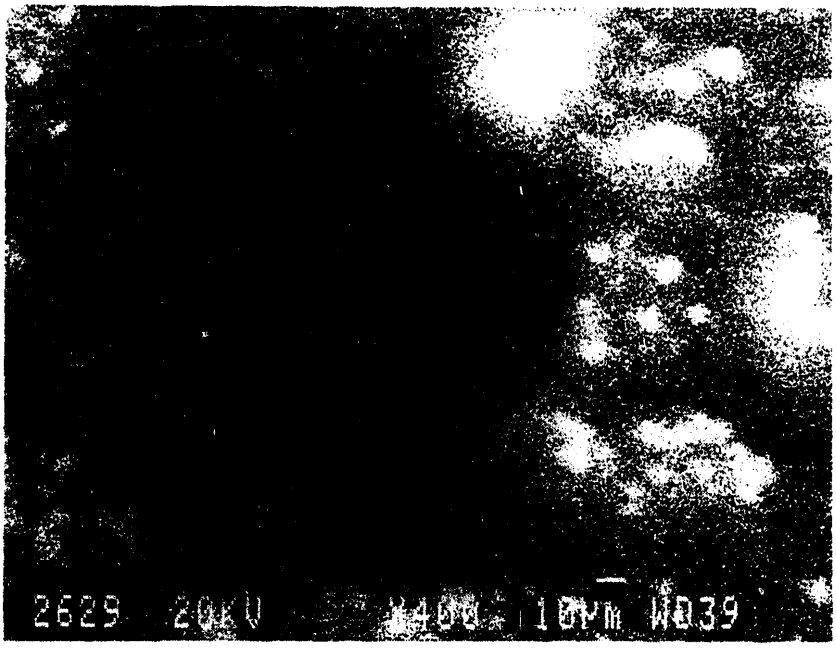

Figure A-25. Sample 1-11-T ROI #2 dot map of Fe (#2629).

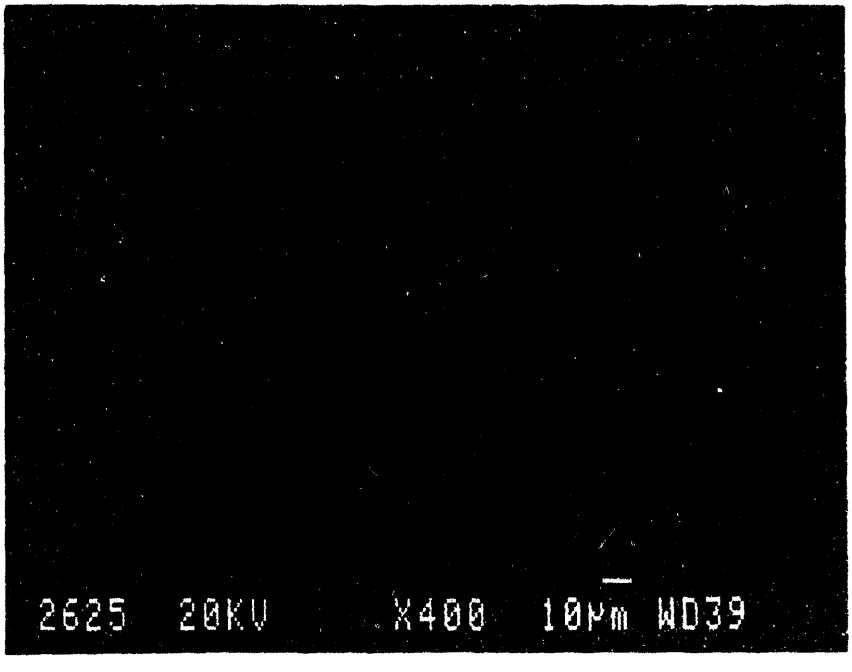

Figure A-26. Sample 1-11-T ROI #2 dot map of Mg (#2625).

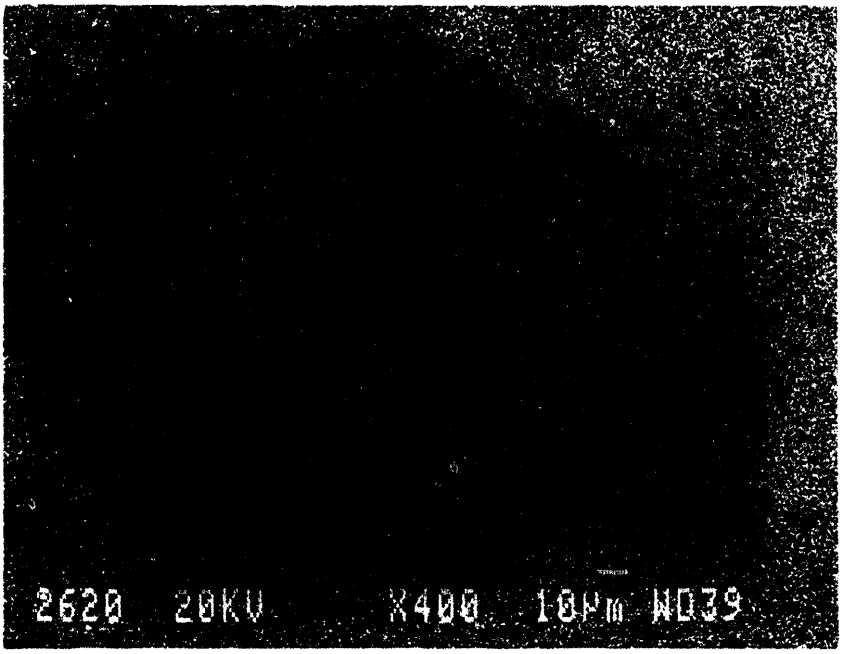

Figure A-27. Sample 1-11-T ROI #2 dot map of Nb (#2620).

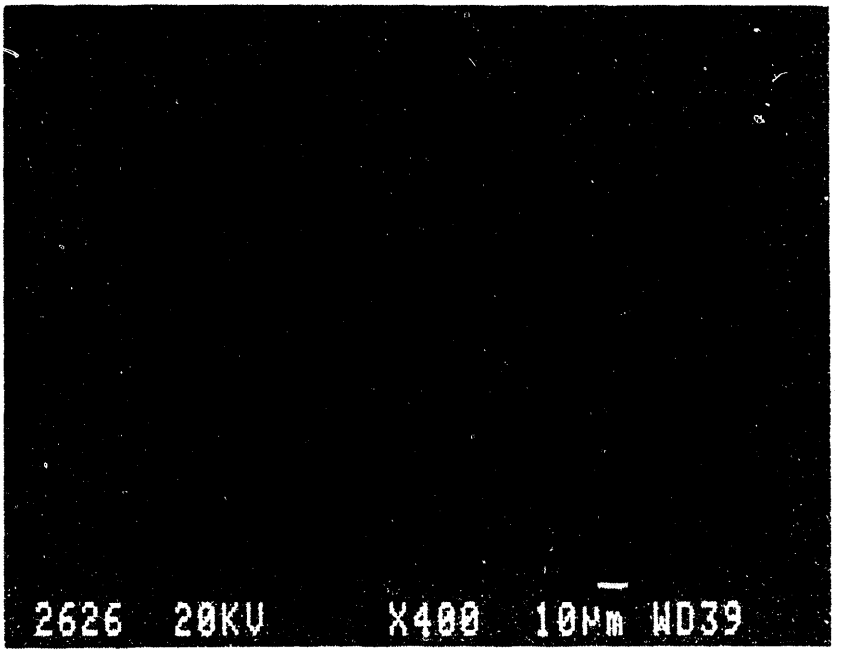

Figure A-28. Sample 1-11-T ROI #2 dot map of Ni (#2626).

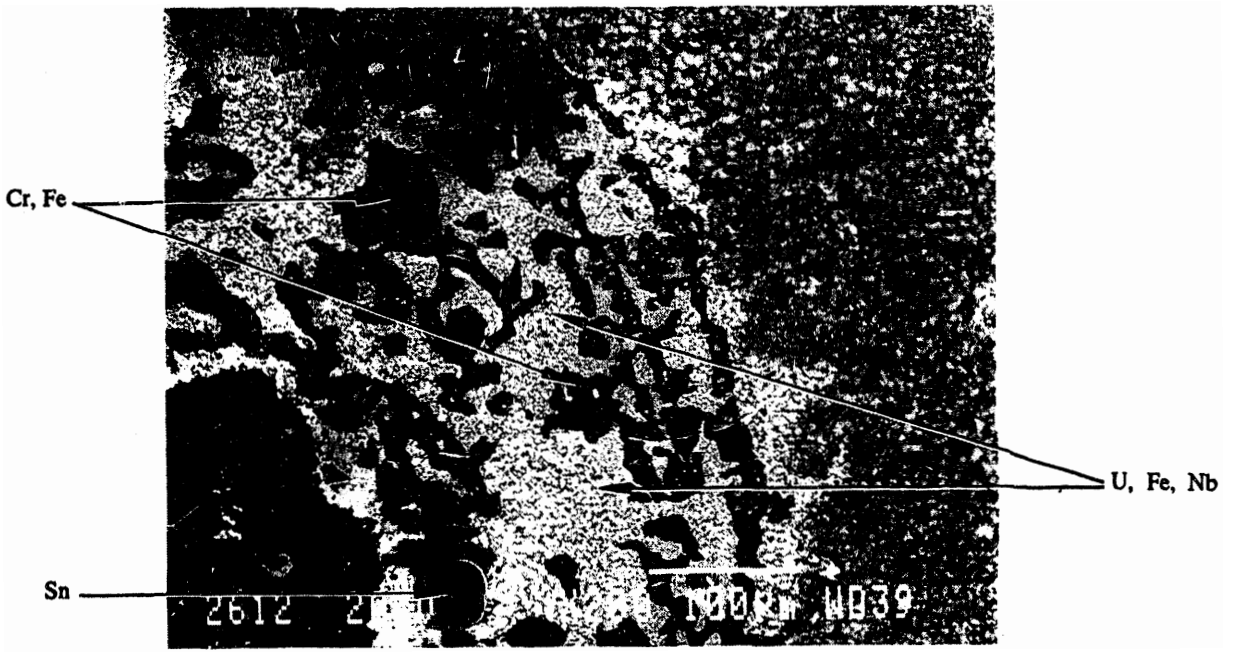

Figure A-29. Sample 1-11-T ROI #3 secondary electron image (#2612).

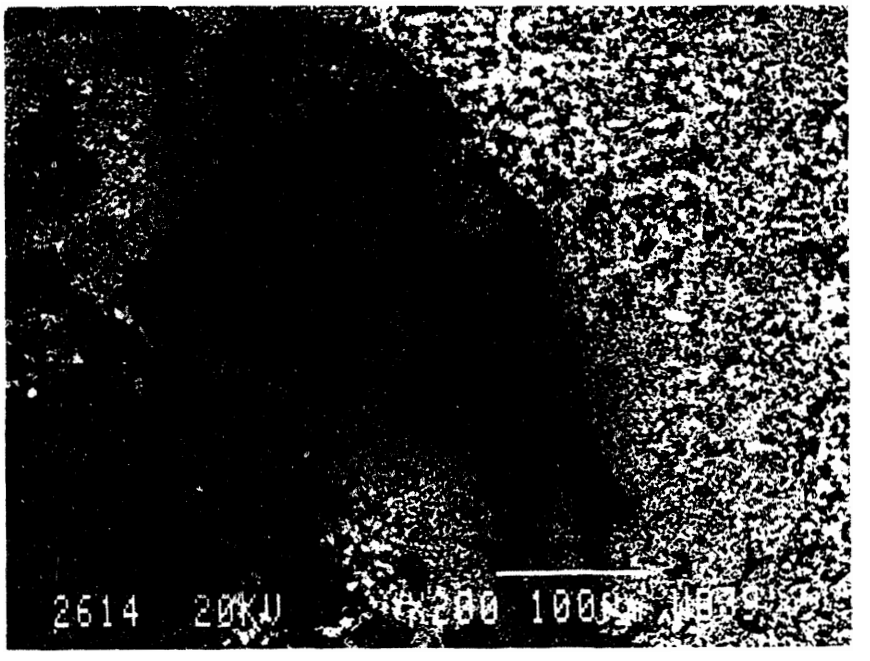

Figure A-30. Sample 1-11-T ROI #3 compositional (#2614).

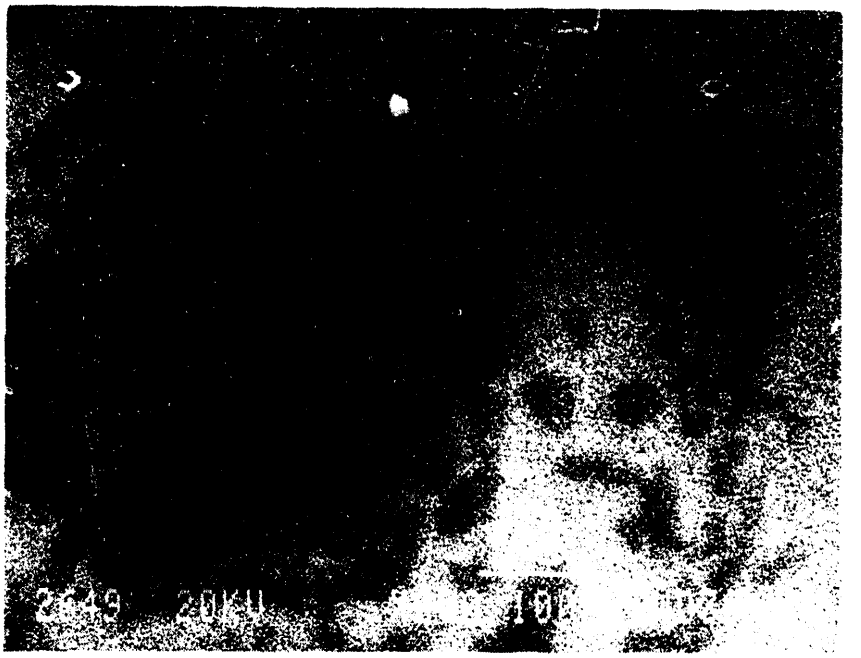

Figure A-31. Sample 1-11-T ROI #3 dot map of U (#2649).

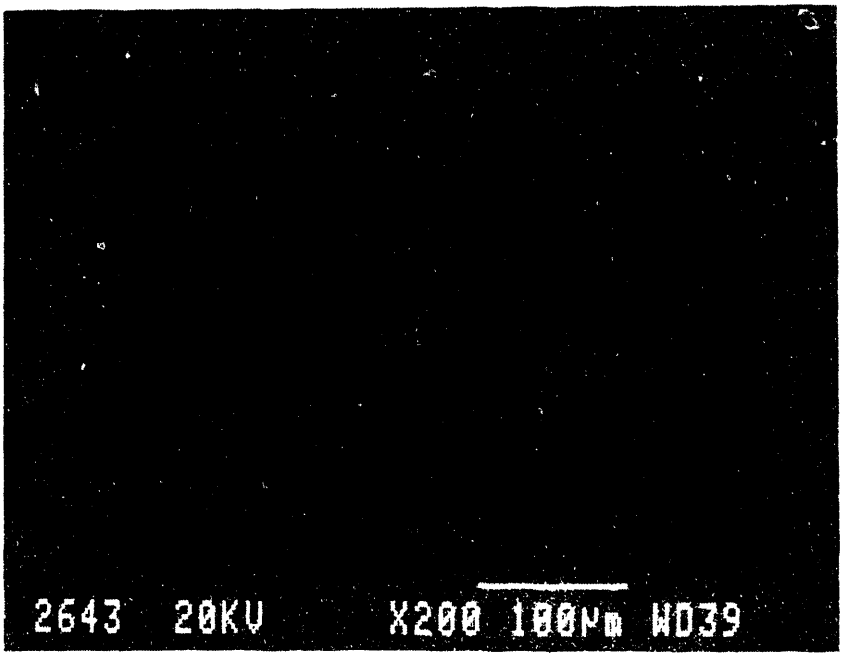

Figure A-32. Sample 1-11-T ROI #3 dot map of O (#2643).

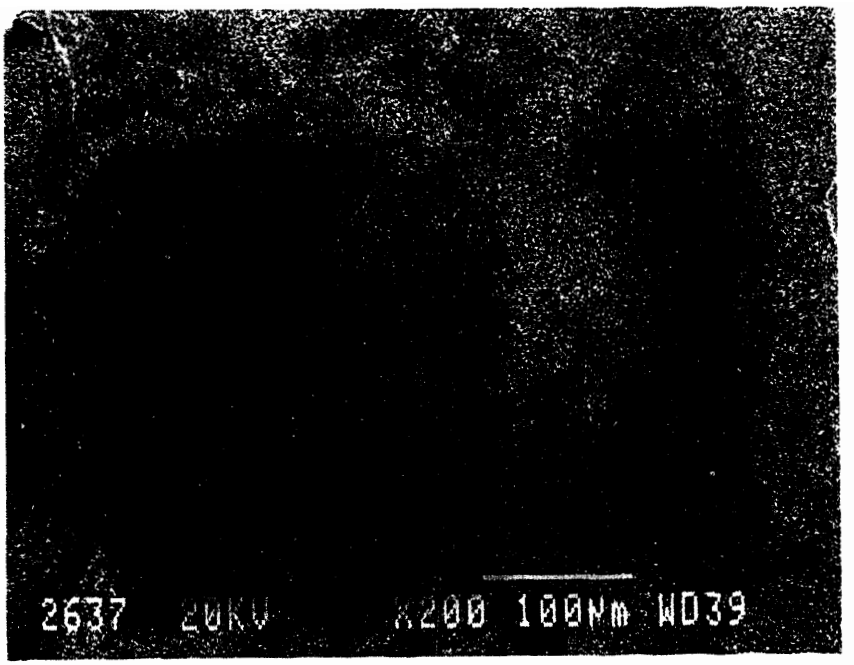

Figure A-33. Sample 1-11-T ROI #3 dot map of Zr (#2637).

Figure A-34. Sample 1-11-T ROI #3 dot map of Cr (#2645).

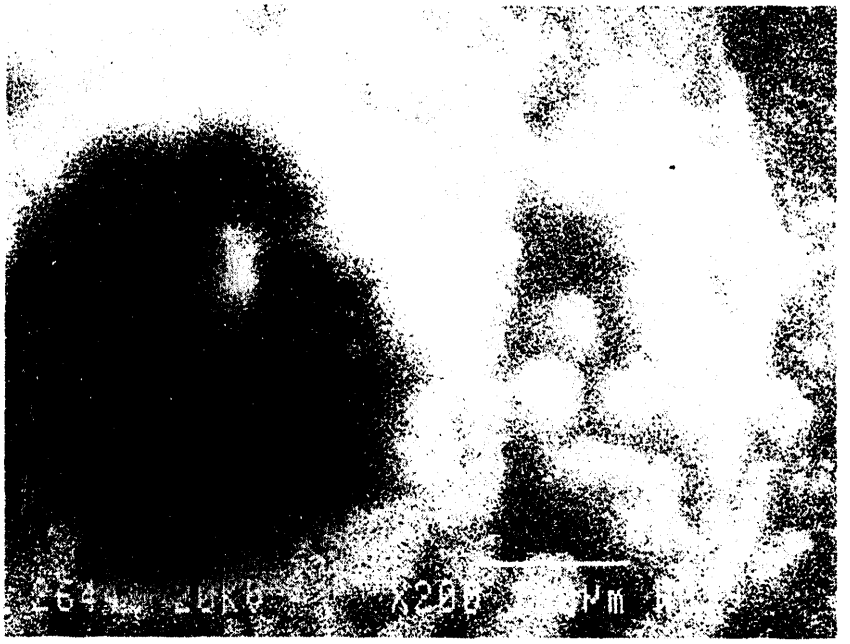

Figure A-35. Sample 1-11-T ROI #3 dot map of Fe (#2644).

Figure A-36. Sample 1-11-T ROI #3 dot map of K (#2647).

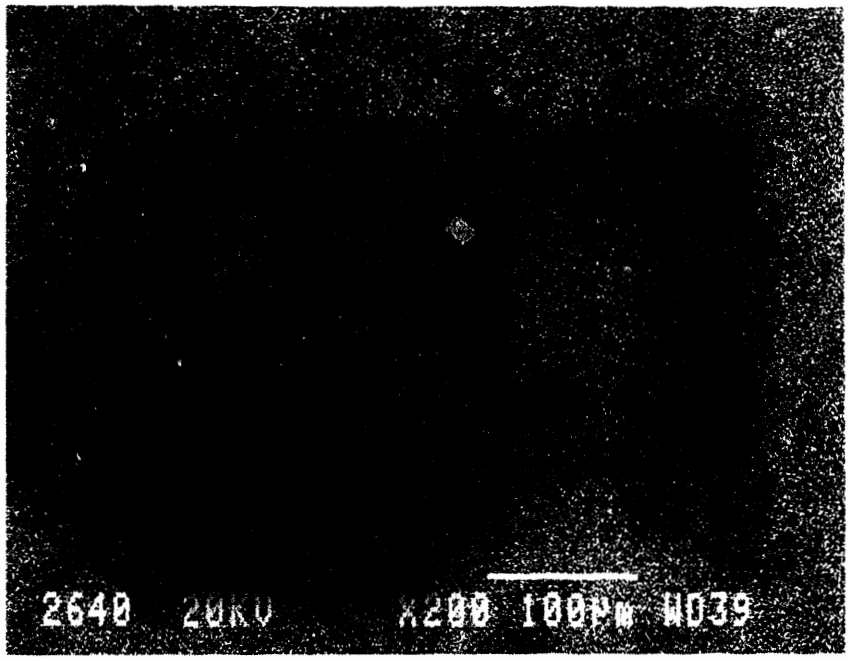

Figure A-37. Sample 1-11-T ROI #3 dot map of Mg (#2640).

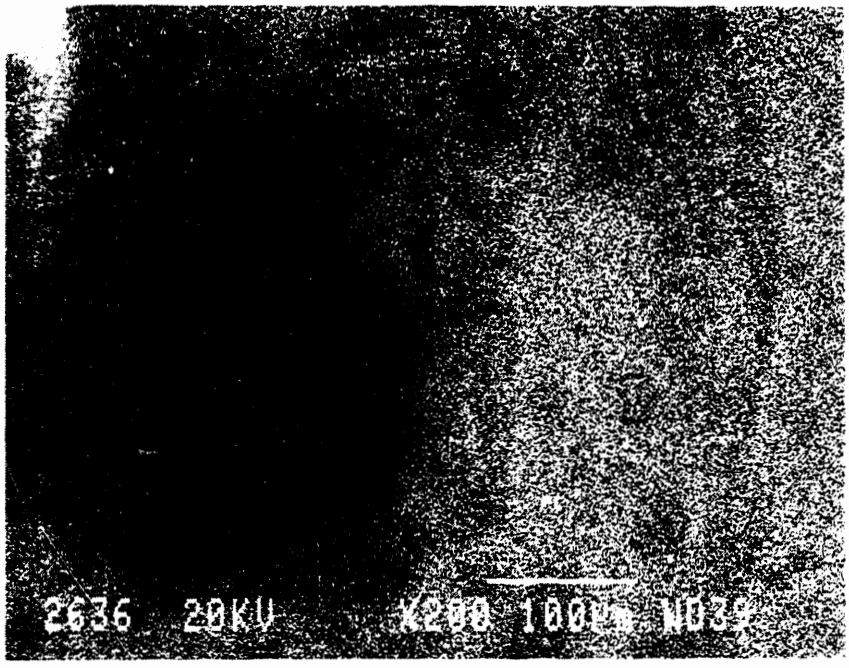

Figure A-38. Sample 1-11-T ROI #3 dot map of Nb (#2636).

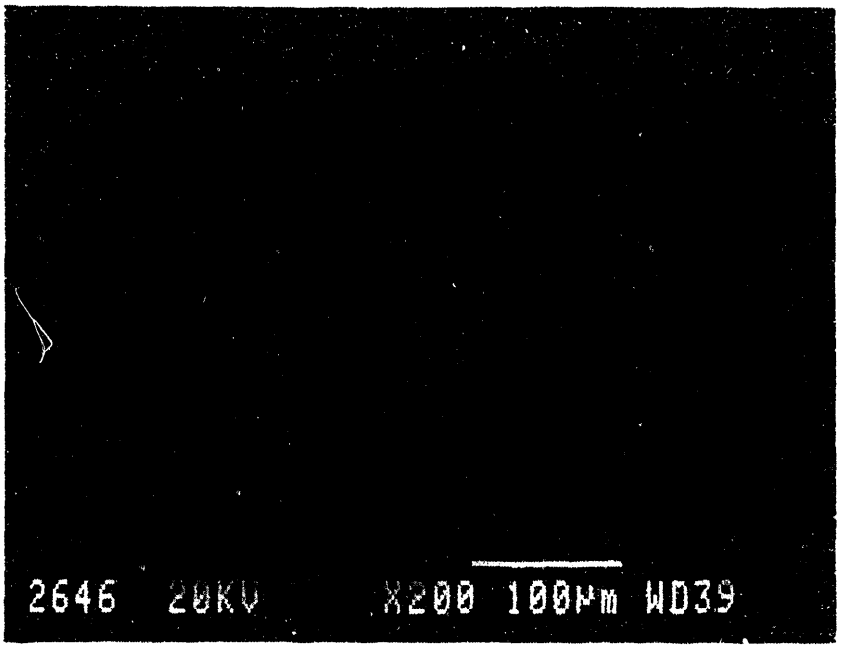

Figure A-39. Sample 1-11-T ROI #3 dot map of Sn (#2646).

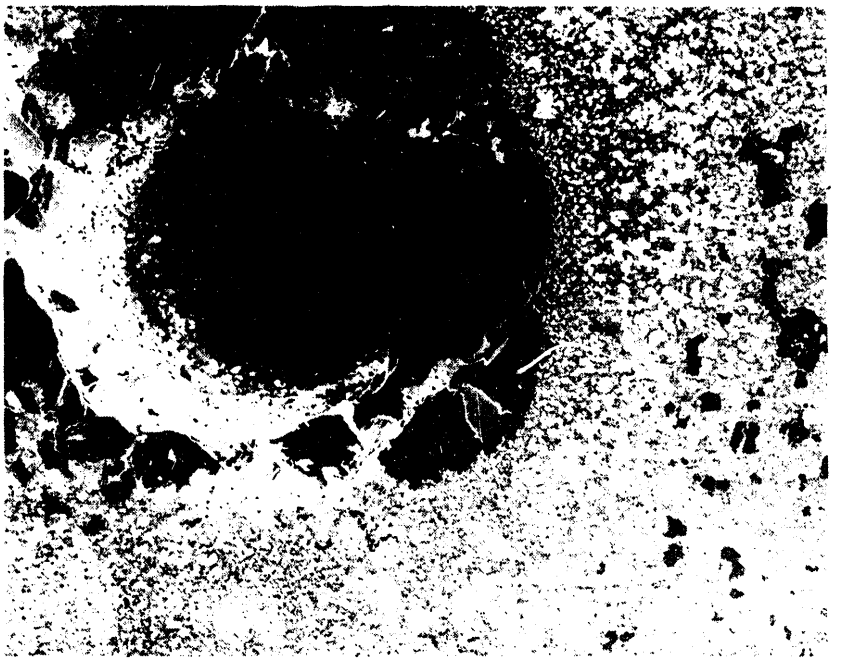

Figure A-40. Sample 1-11-T ROI #4 secondary electron image (#2615).

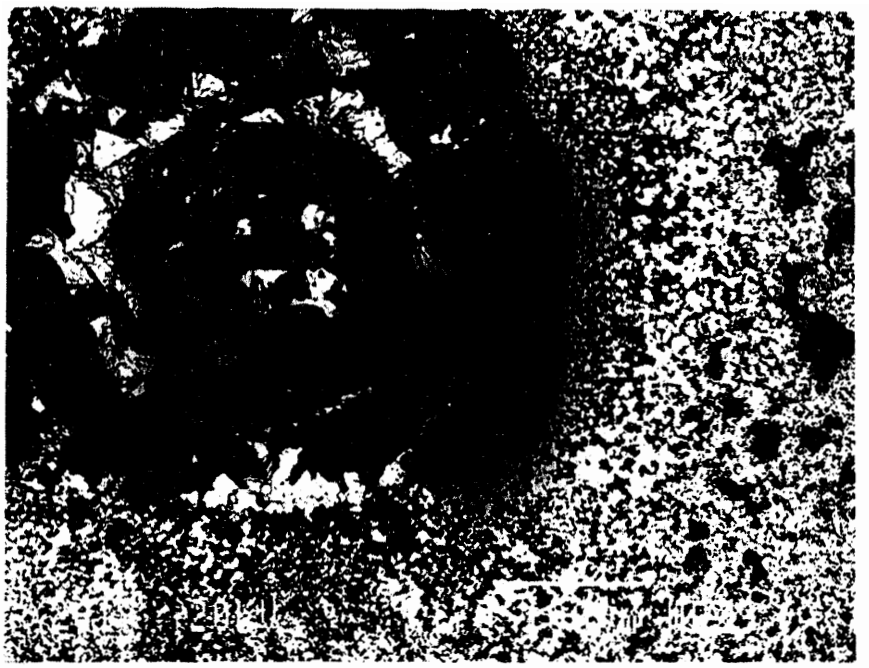

Figure A-41. Sample 1-11-T ROI #4 compositional (#2617).

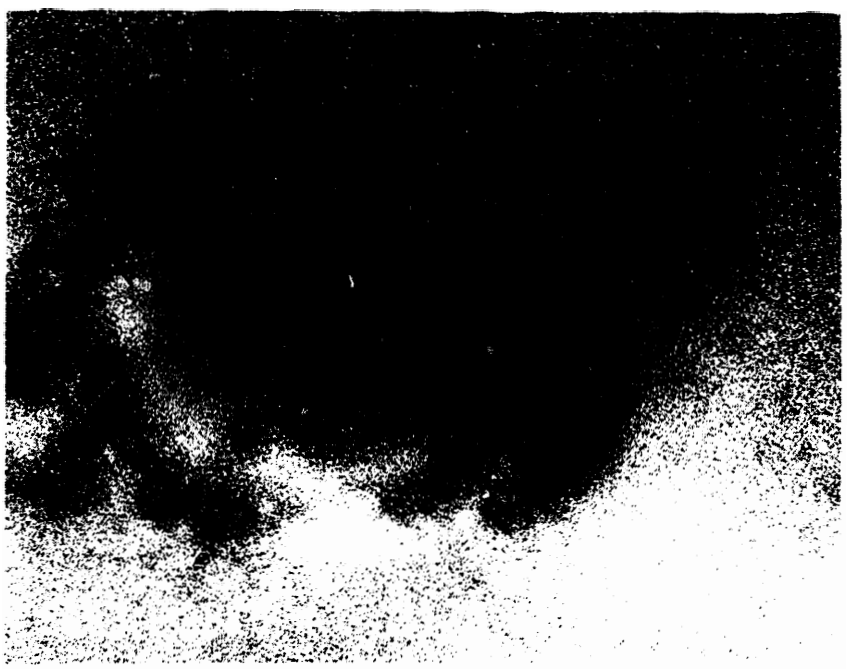

Figure A-42. Sample 1-11-T ROI #4 dot map of U (#2663).

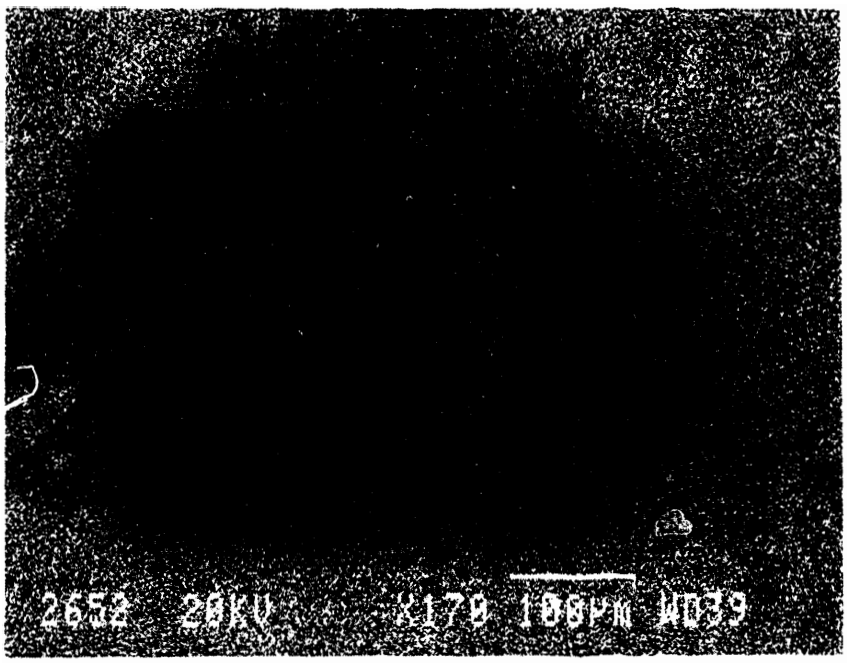

Figure A-43. Sample 1-11-T ROI #4 dot map of Zr (#2652).

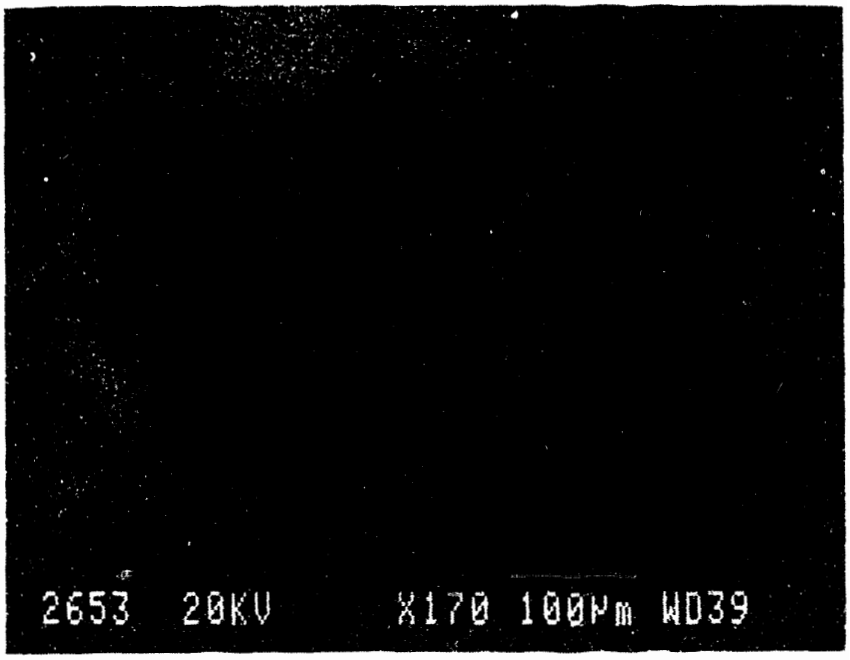

Figure A-44. Sample 1-11-T ROI #4 dot map of Al (#2653).

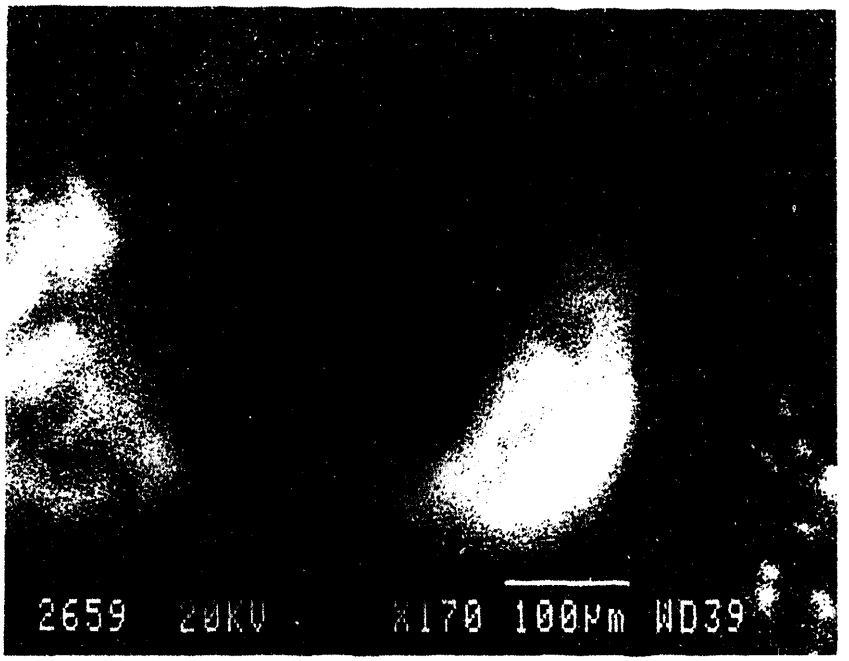

Figure A-45. Sample 1-11-T ROI #4 dot map of Cr (#2659).

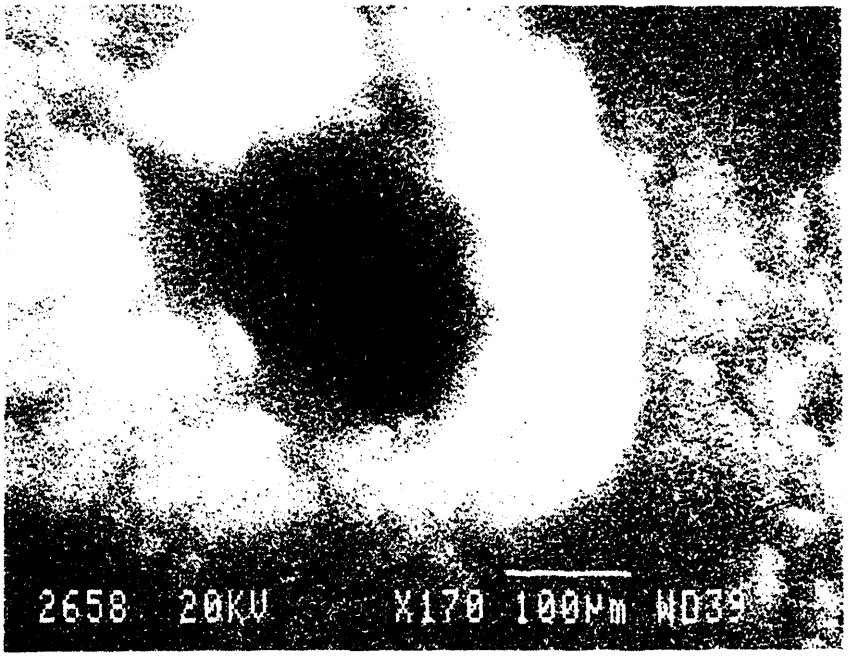

Figure A-46. Sample 1-11-T ROI #4 dot map of Fe (#2658).

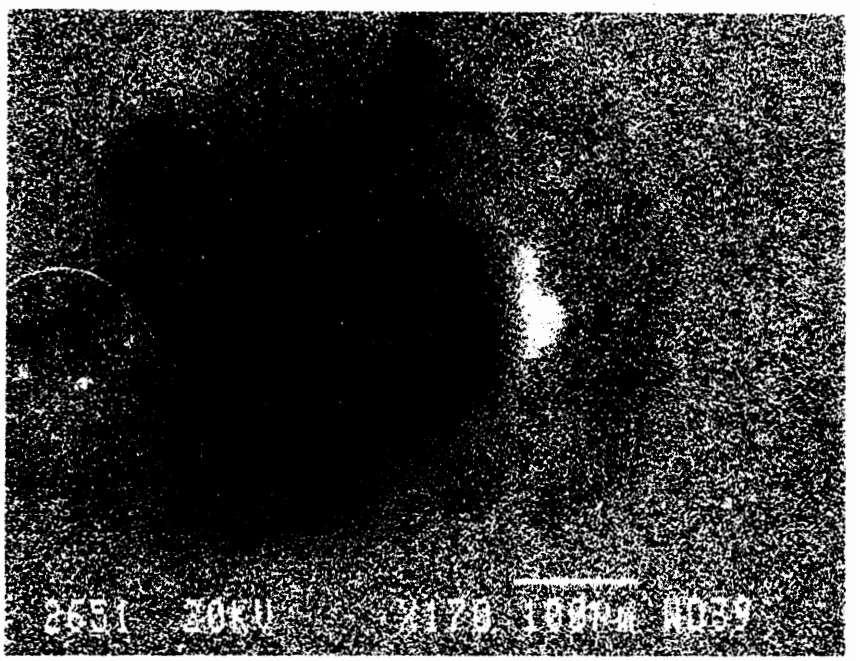

Figure A-47. Sample 1-11-T ROI #4 dot map of Nb (#2651).

Figure A-48. Sample 1-11-T ROI #5 secondary electron image (#2618).

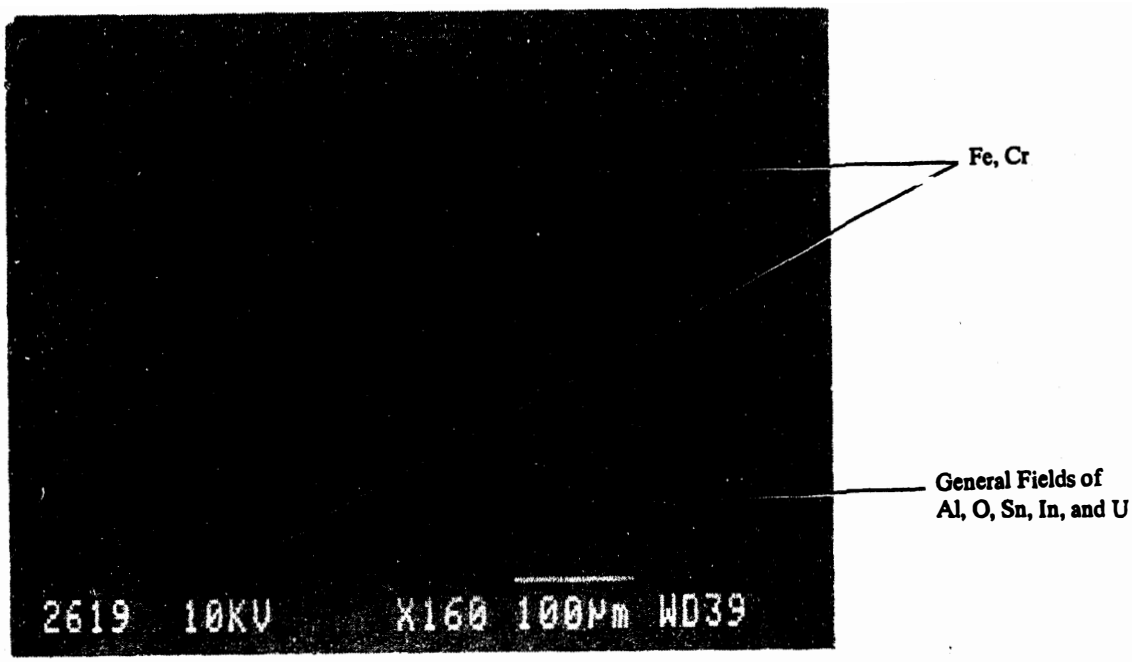

Figure A-49. Sample 1-11-T ROI #5 topographical (#2619).

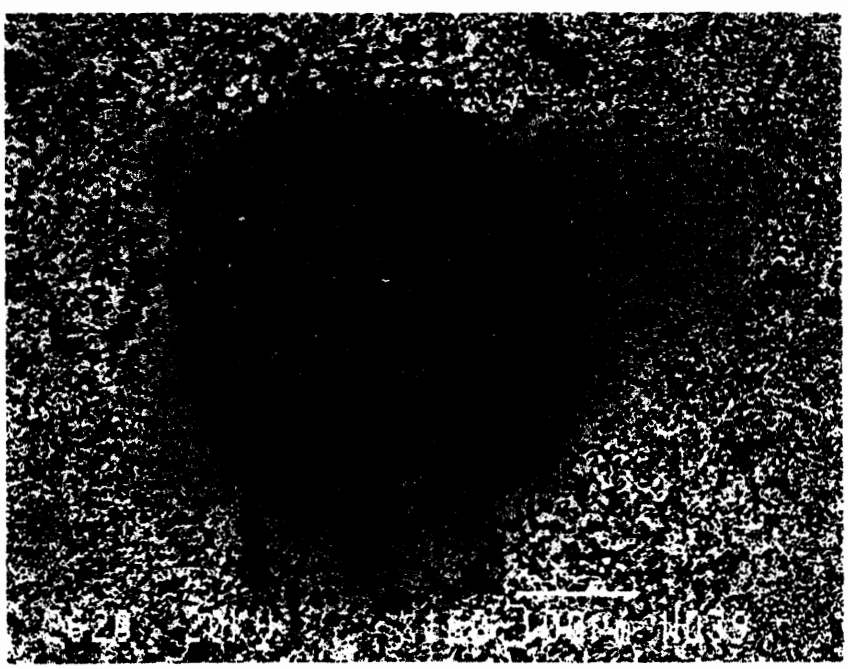

Figure A-50. Sample 1-11-T ROI #5 compositional (#2620).

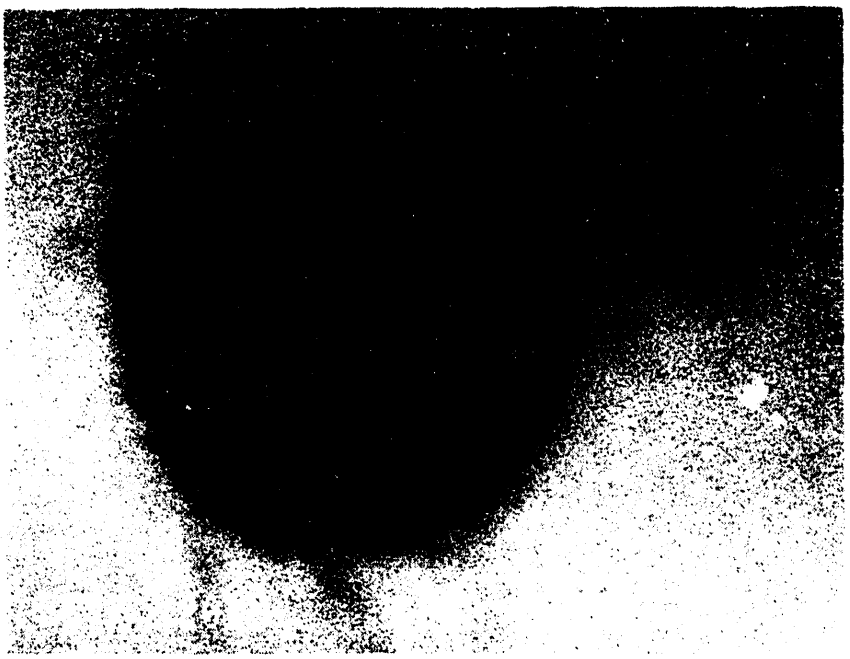

Figure A-51. Sample 1-11-T ROI #5 dot map of U (#2677).

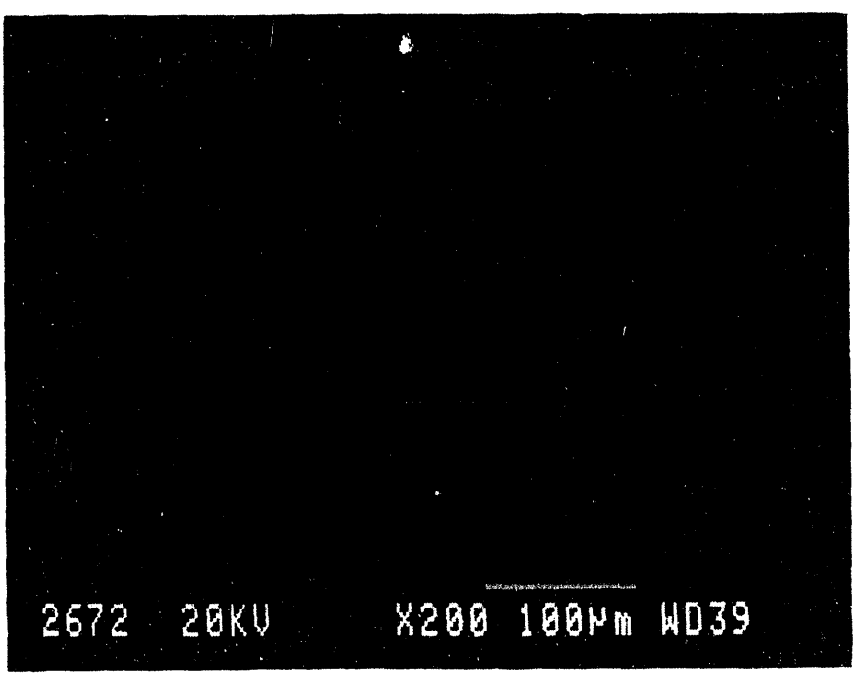

Figure A-52. Sample 1-11-T ROI #5 dot map of O (#2672).

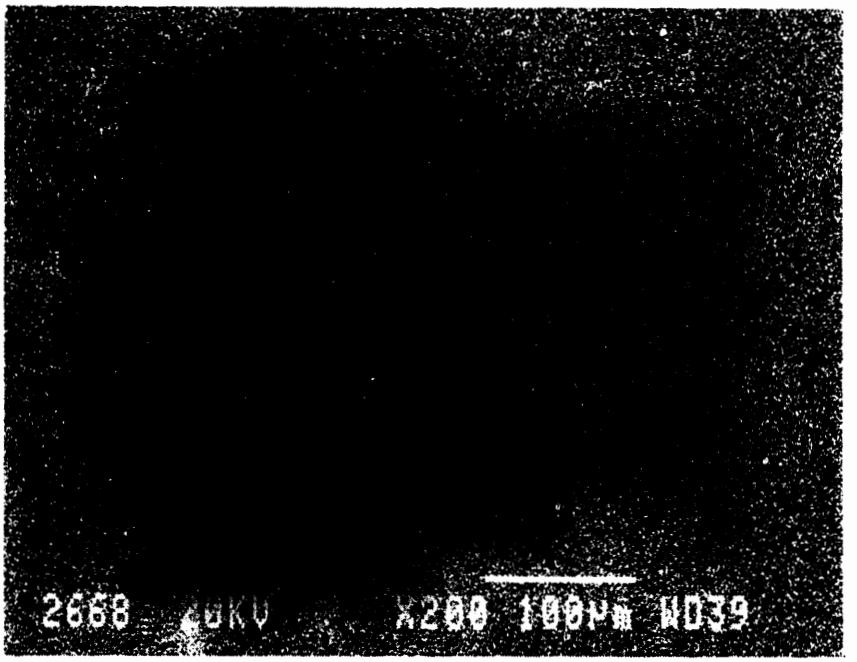

Figure A-53. Sample 1-11-T ROI #5 dot map of Al (#2668).

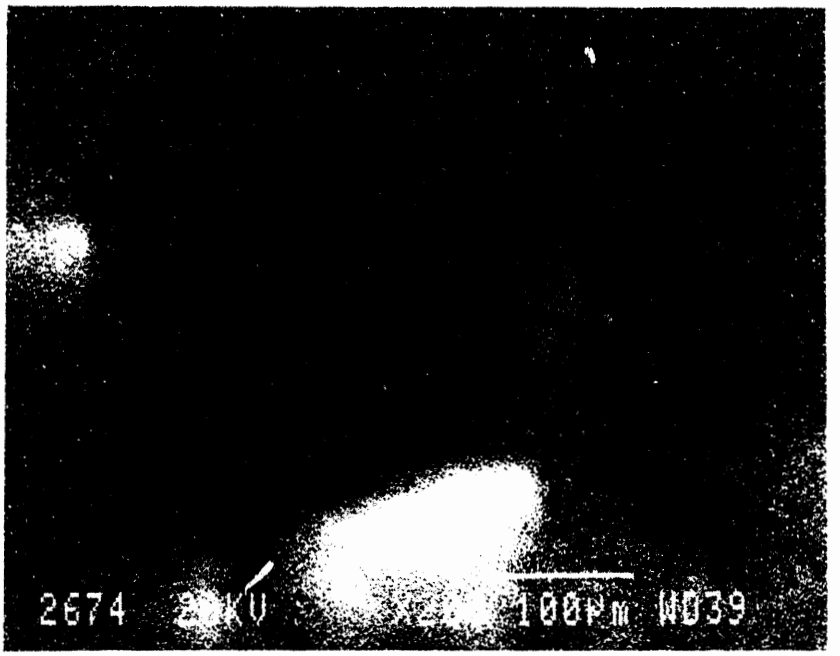

Figure A-54. Sample 1-11-T ROI #5 dot map of Cr (#2674).

Figure A-55. Sample 1-11-T ROI #5 dot map of Fe (#2673).

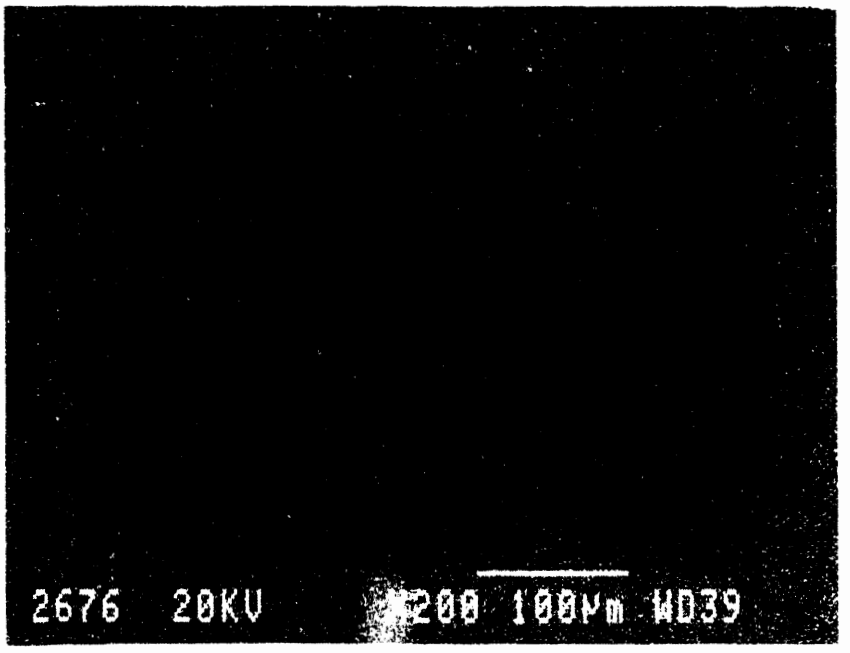

Figure A-56. Sample 1-11-T ROI #5 dot map of In (#2676).

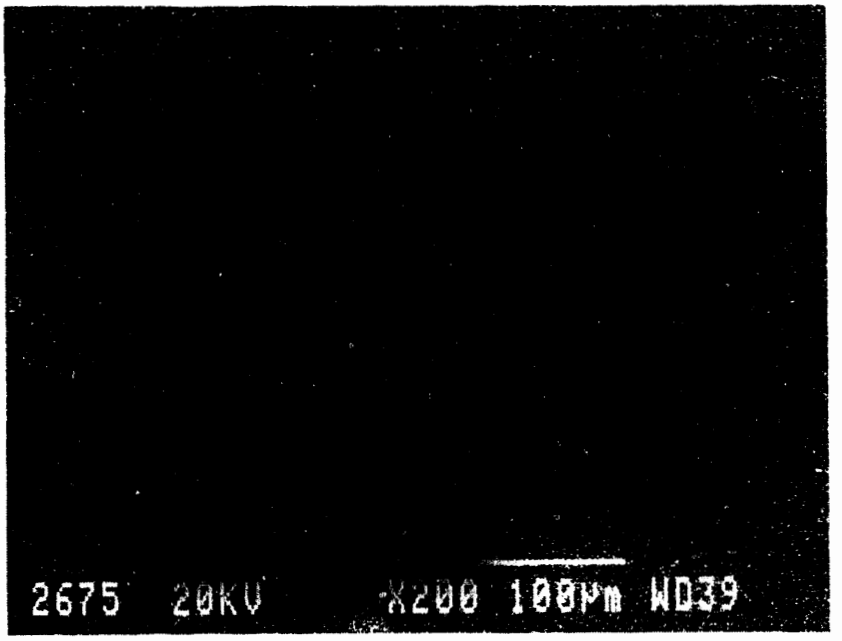

Figure A-57. Sample 1-11-T ROI #5 dot map of Sn (#2675).

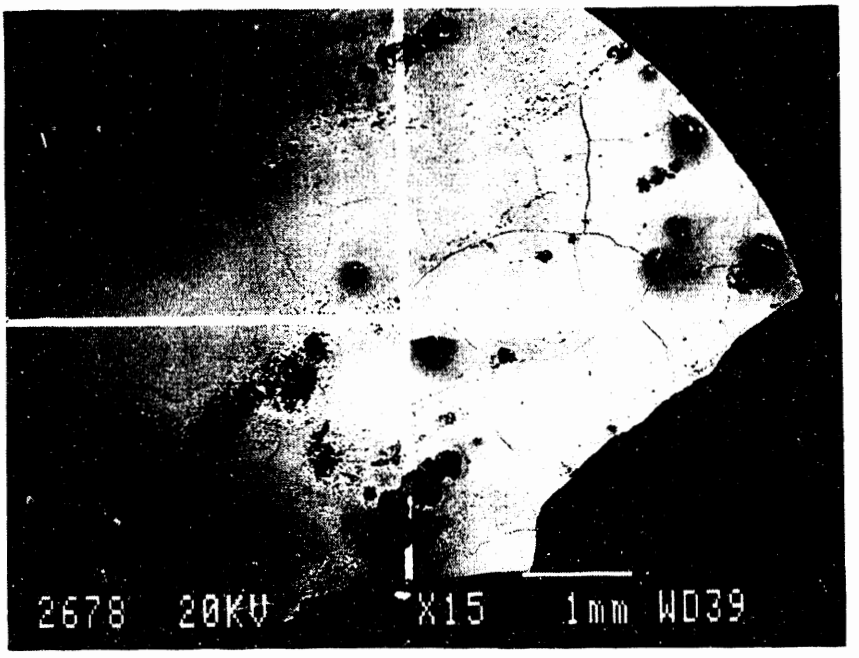

Figure A-58. Sample 1-9-A ROI #1 (area of interest) secondary electron image (#2678).

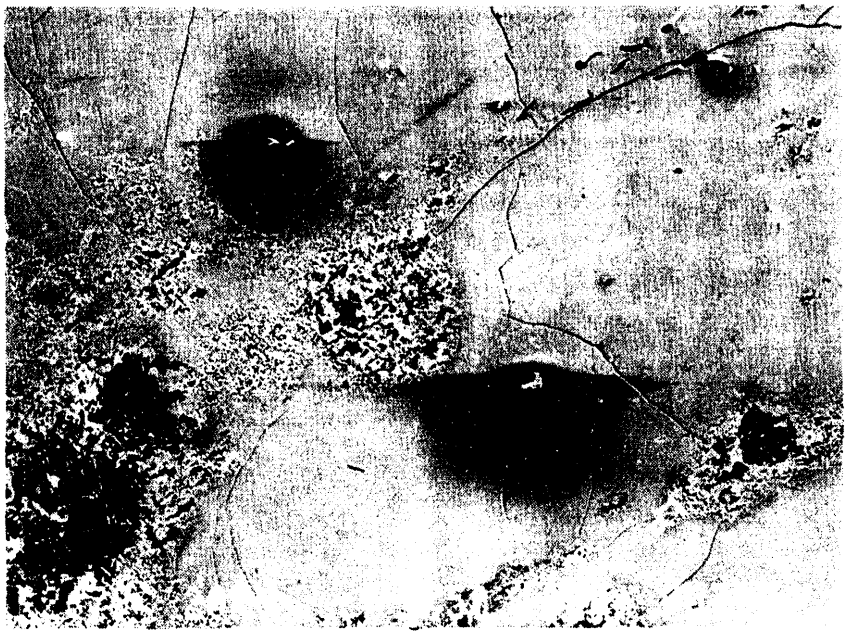

Figure A-59. Sample 1-9-A ROI #1 (reduced area of interest) secondary electron image (#2679).

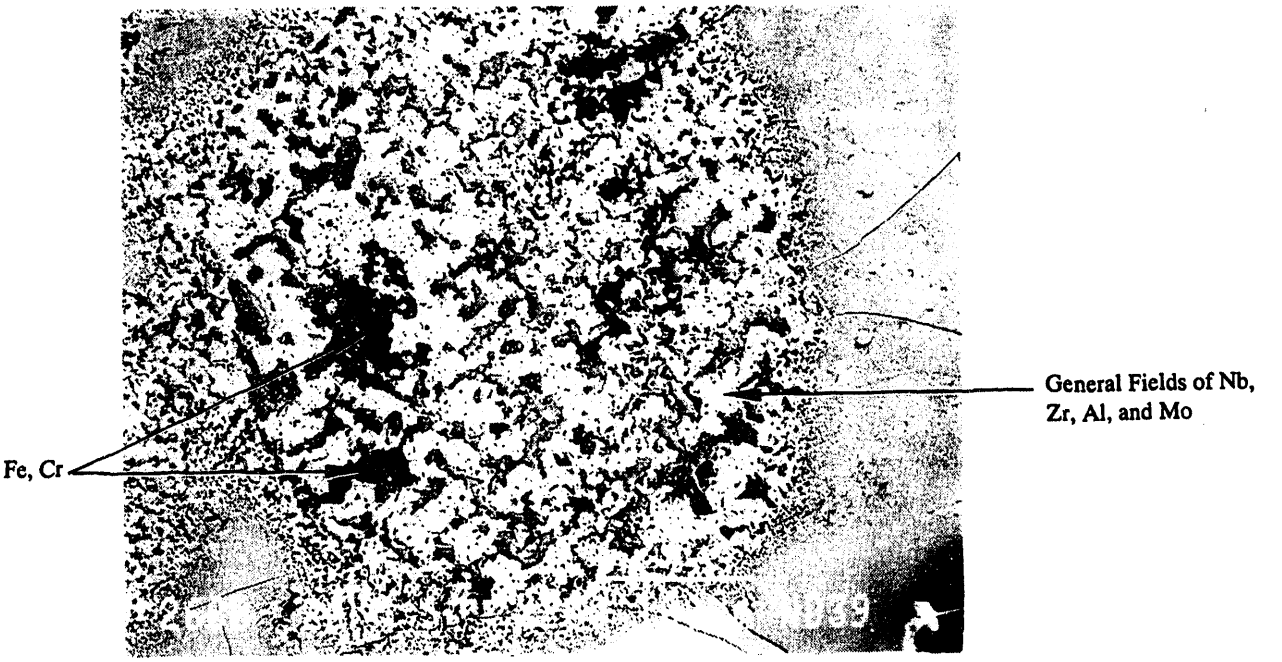

Figure A-60. Sample 1-9-A ROI #1 (further reduced area of interest) secondary electron image (#2680).

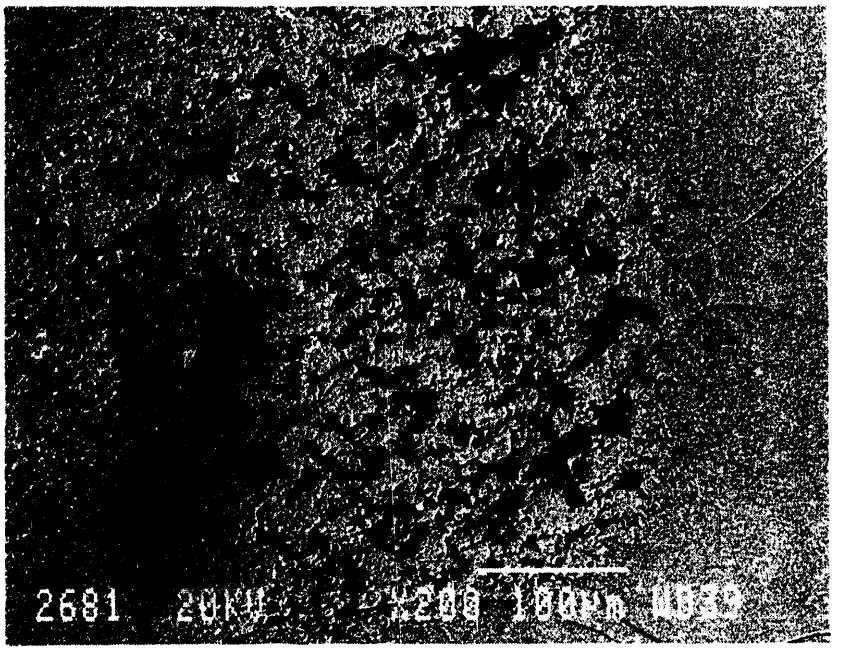

Figure A-61. Sample 1-9-A ROI #1 topographical (#2681).

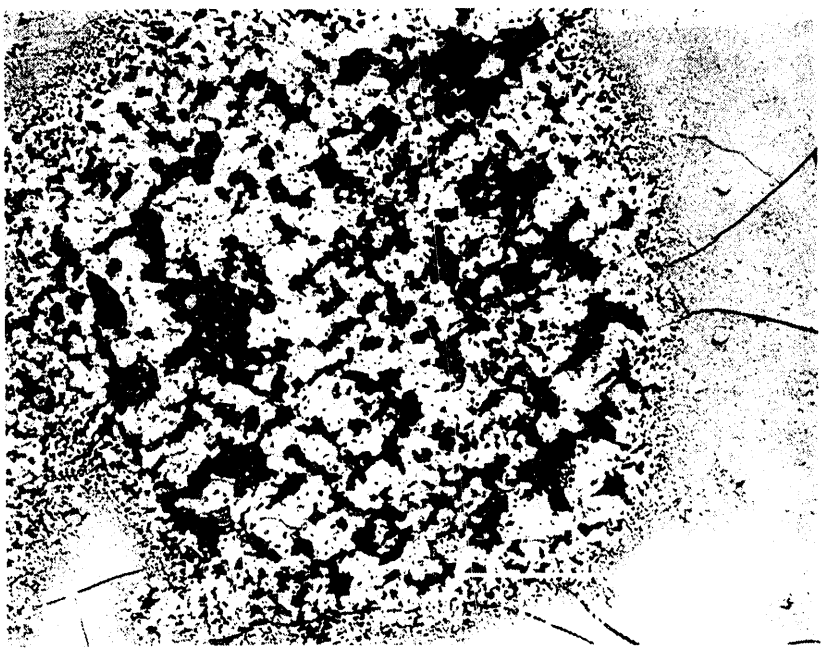

Figure A-62. Sample 1-9-A ROI #1 compositional (#2682).

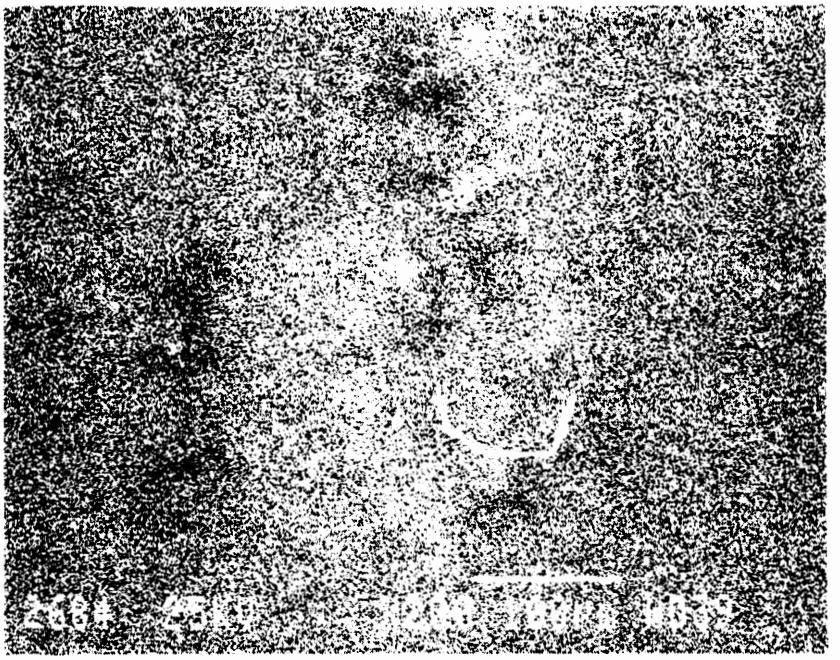

Figure A-63. Sample 1-9-A ROI #1 dot map of Zr (#2684).

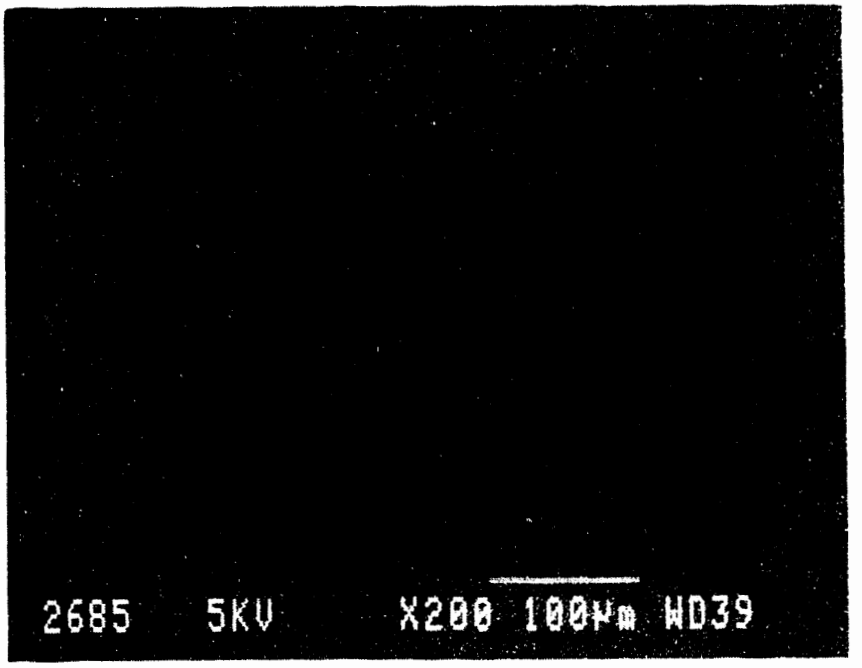

Figure A-64. Sample 1-9-A ROI #1 dot map of Al (#2685).

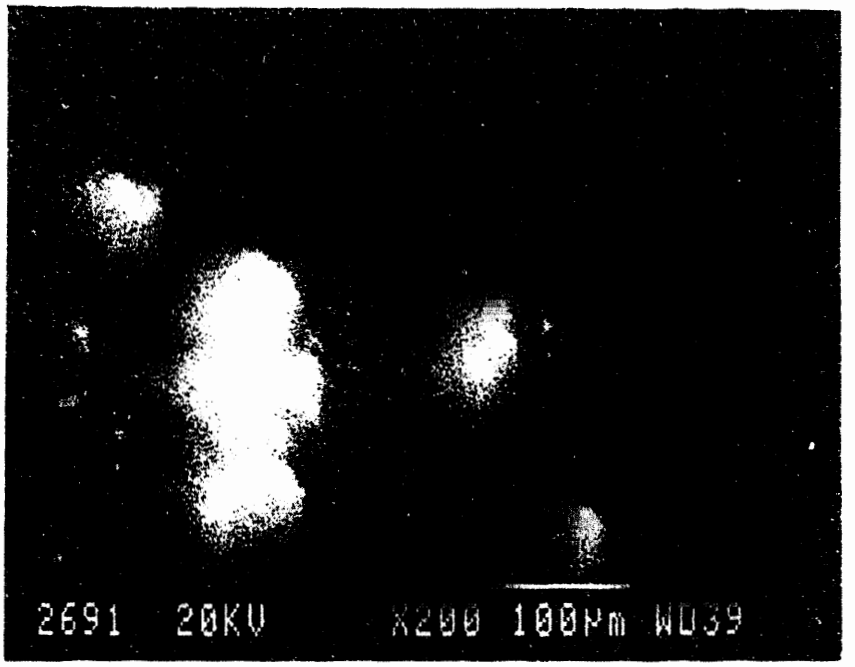

Figure A-65. Sample 1-9-A ROI #1 dot map of Cr (#2691).

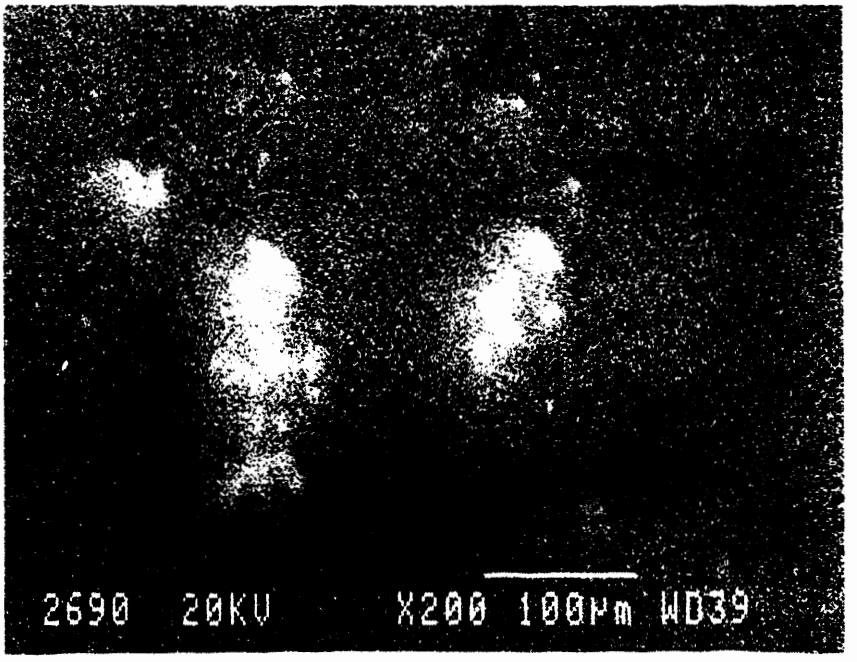

Figure A-66. Sample 1-9-A ROI #1 dot map of Fe (#2690).

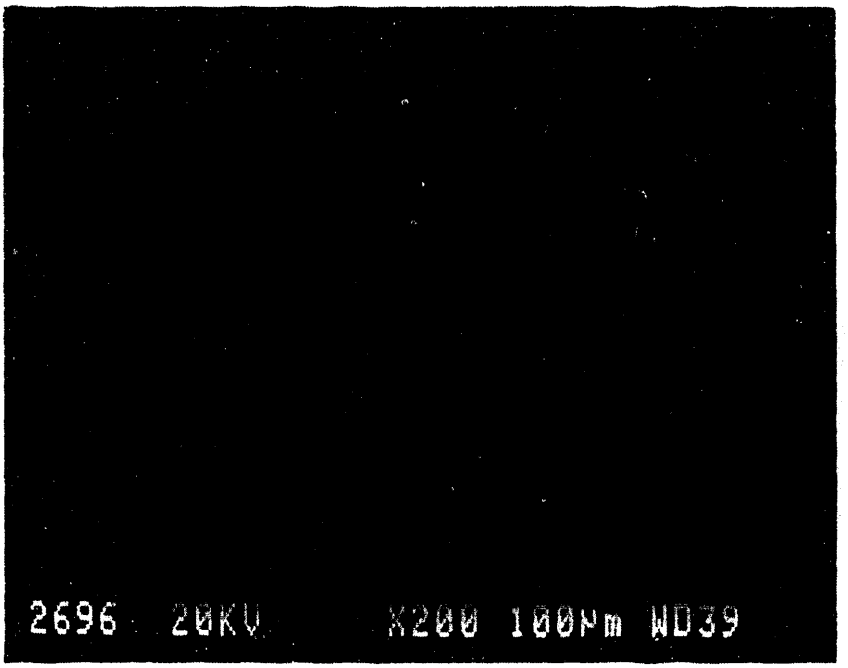

Figure A-67. Sample 1-9-A ROI #1 dot map of Mo (#2696).

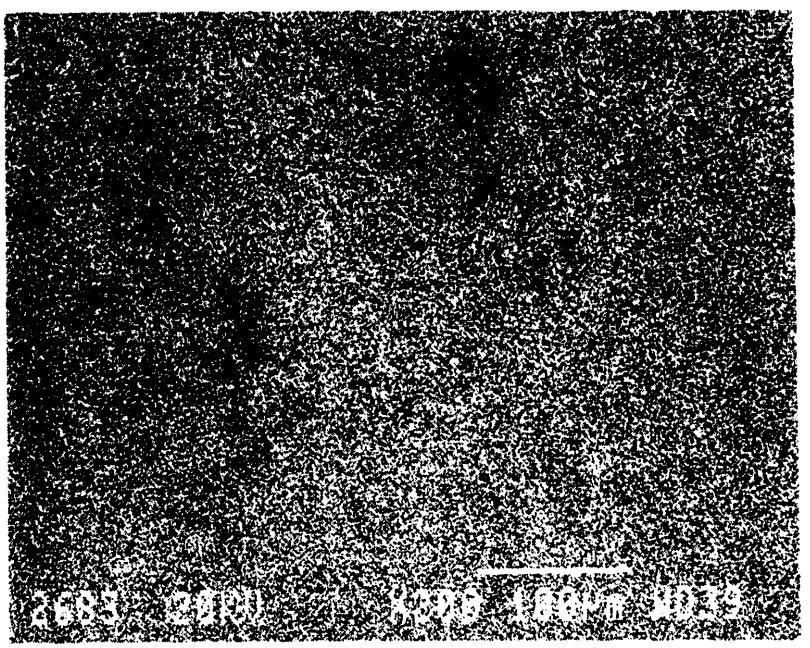

Figure A-68. Sample 1-9-A ROI #1 dot map of Nb (#2683).

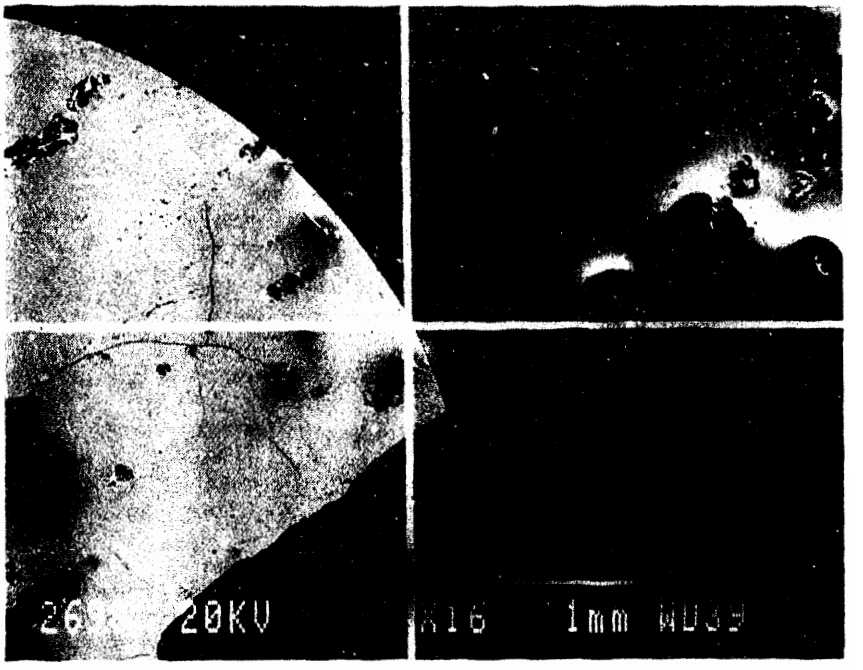

Figure A-69. Sample 1-9-A ROI #2 (area of interest) secondary electron image (#2697).

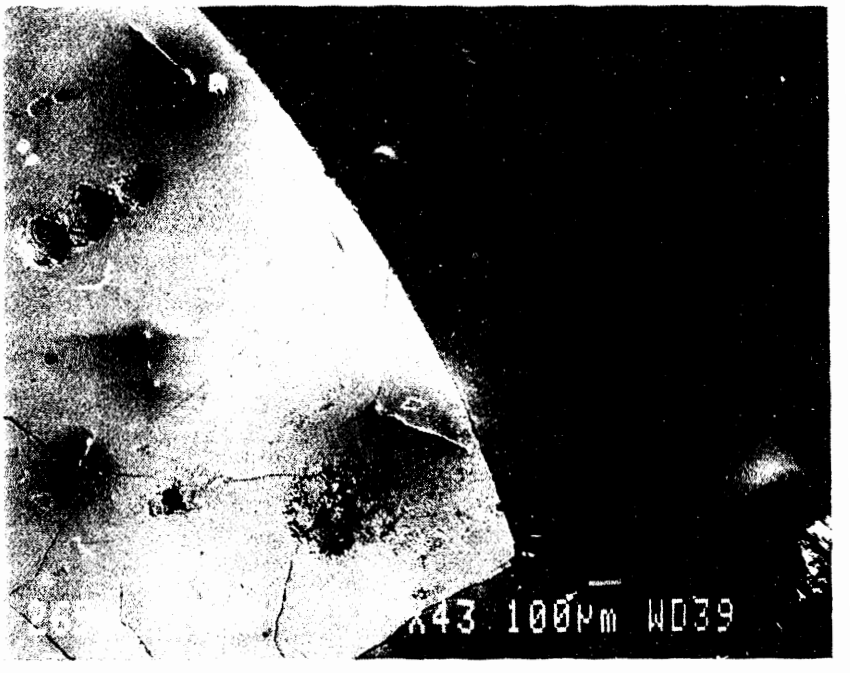

Figure A-70. Sample 1-9-A ROI #2 secondary electron image (#2698).

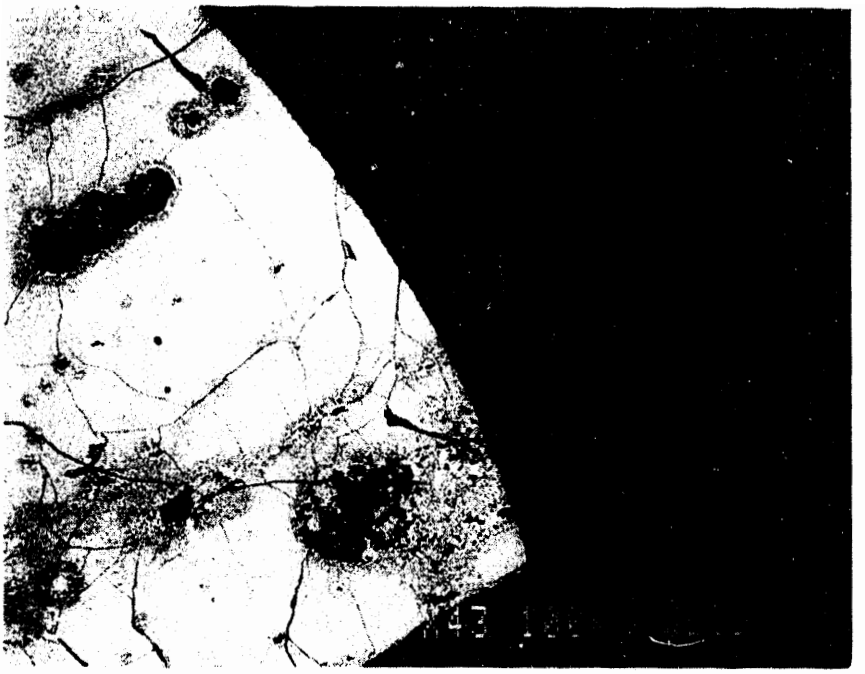

Figure A-71. Sample 1-9-A ROI #2 topographical (#2699).

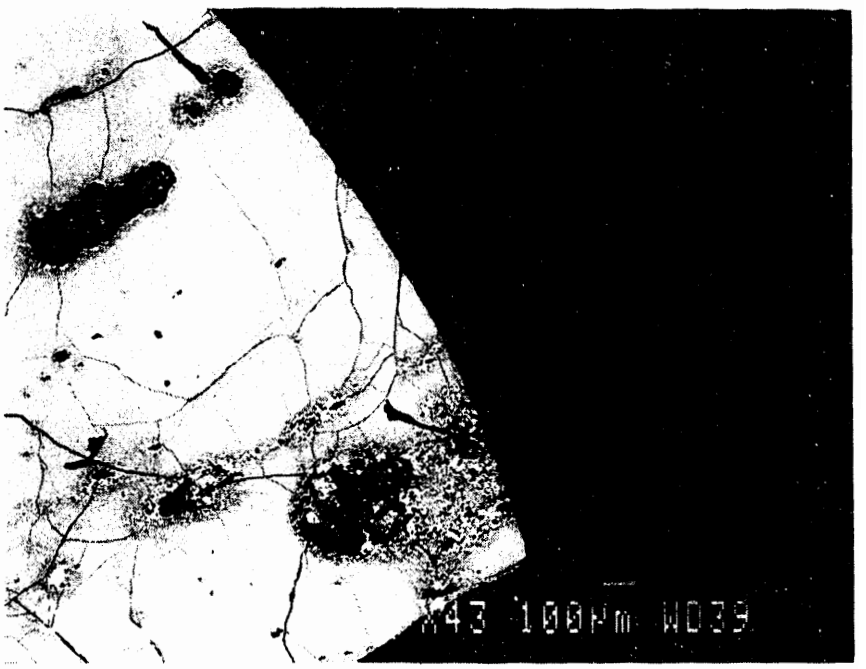

Figure A-72. Sample 1-9-A ROI #2 compositional (#2700).

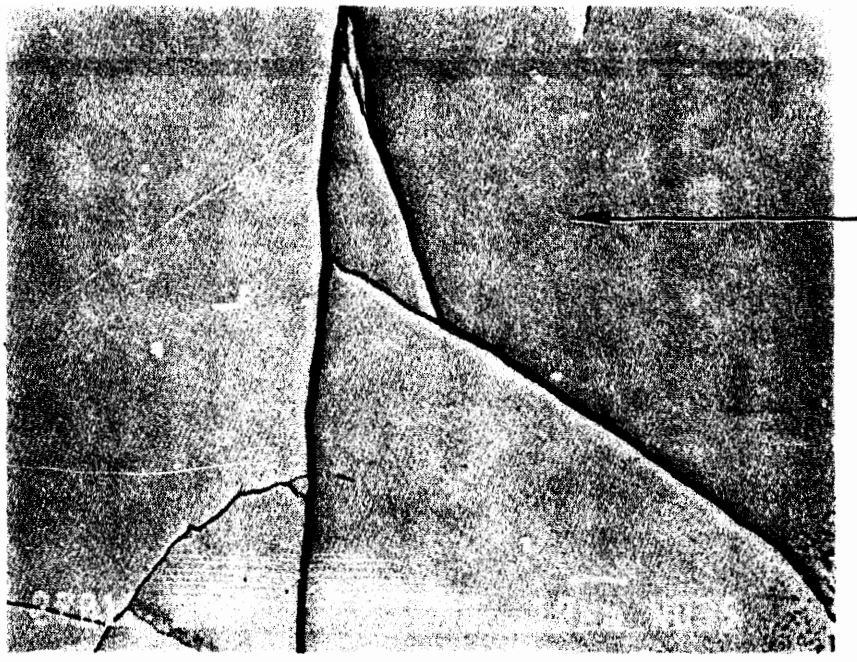

Figure A-73. Sample 1-9-A ROI #2 (reduced area of interest) secondary electron image (#2701).

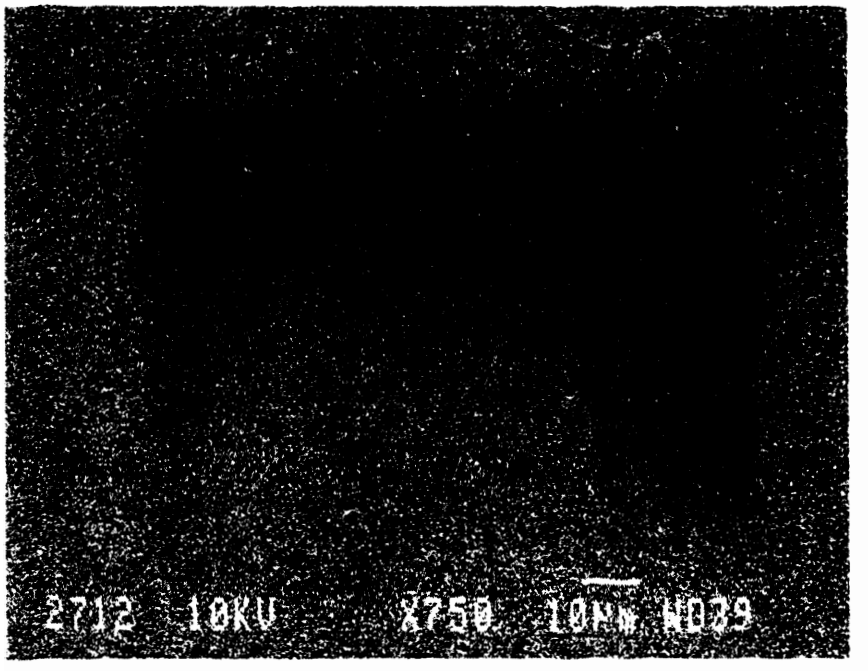

Figure A-74. Sample 1-9-A ROI #2 dot map of U (#2712).

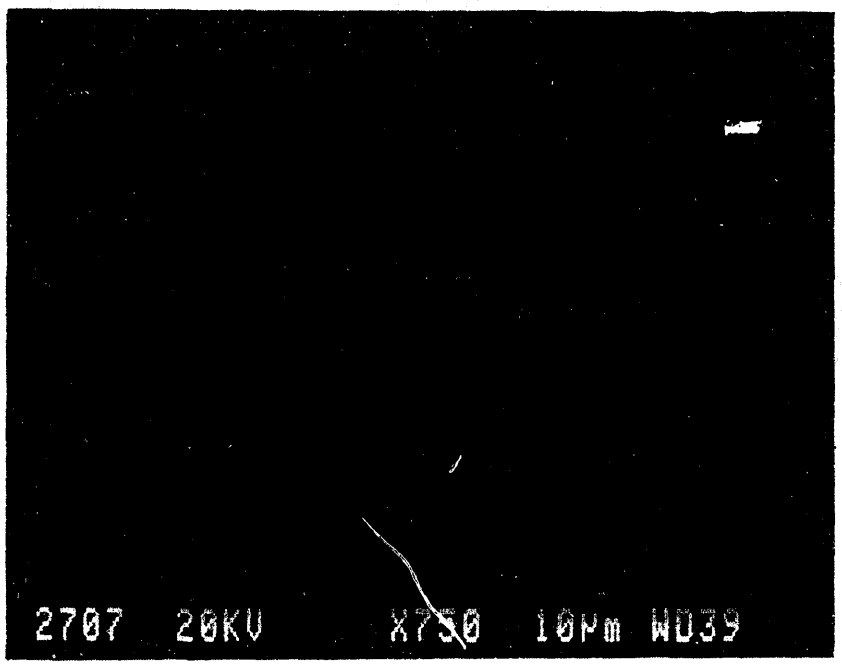

Figure A-75. Sample 1-9-A ROI #2 dot map of O (#2707).

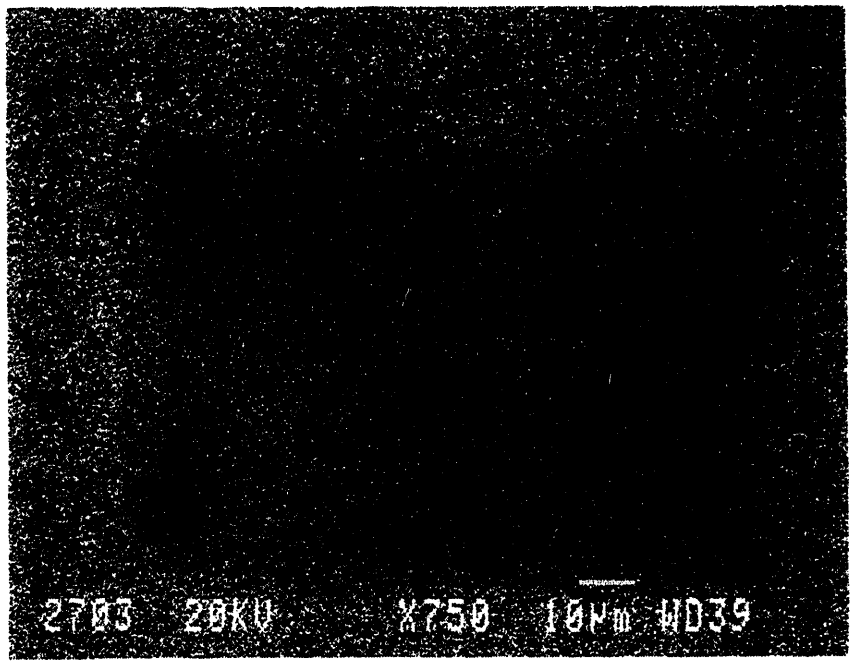

Figure A-76. Sample 1-9-A ROI #2 dot map of Zr (#2703).

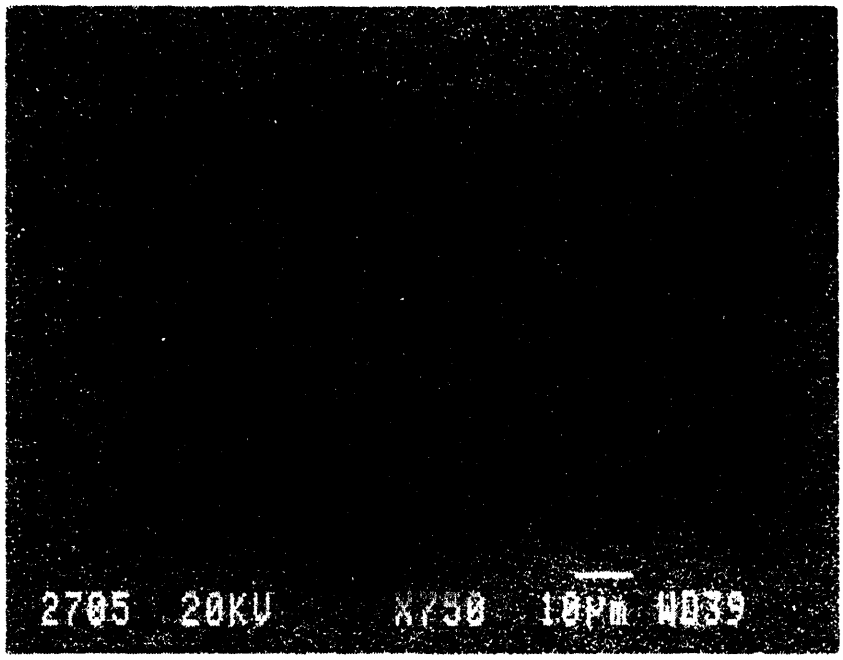

Figure A-77. Sample 1-9-A ROI #2 dot map of Ni (#2705).

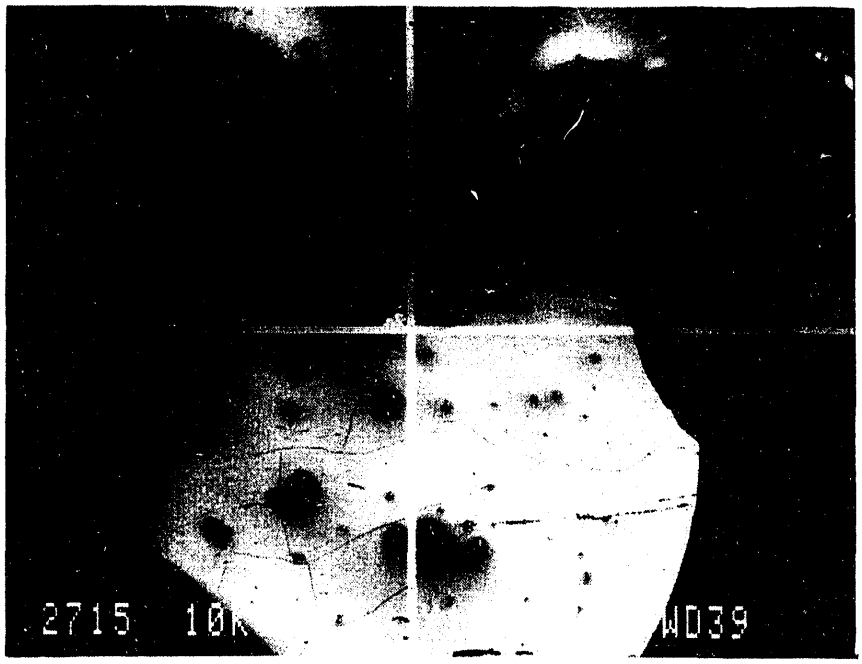

Figure A-78. Sample 1-9-B ROI #1 (area of interest) secondary electron image (#2715).

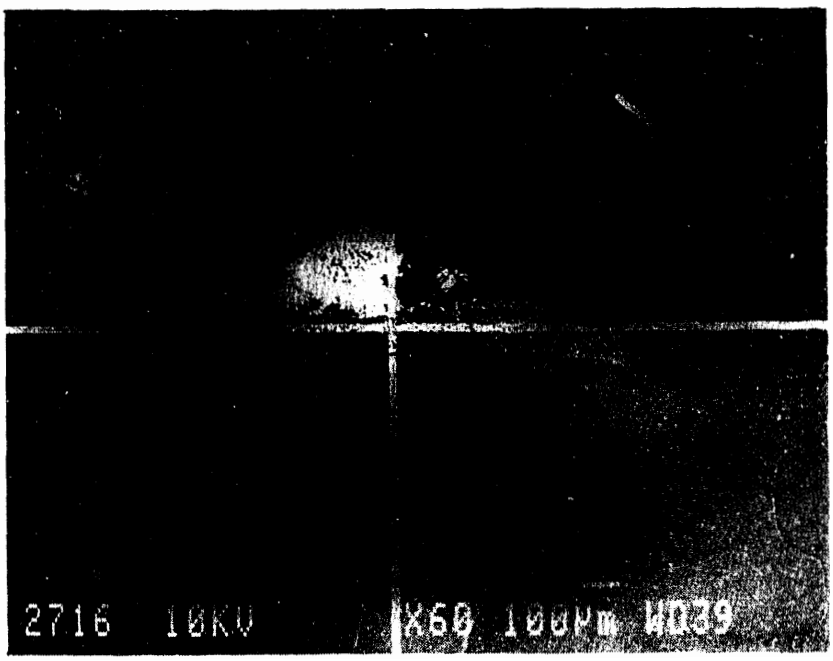

Figure A-79. Sample 1-9-B ROI #1 (reduced area of interest) secondary electron image (#2716).

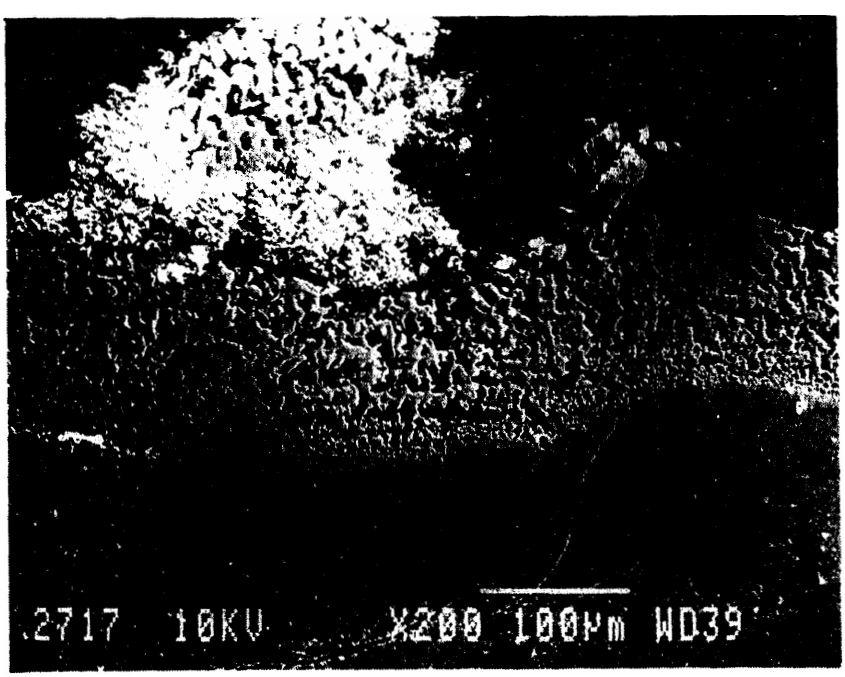

Figure A-80. Sample 1-9-B ROI #1 (further reduced area of interest) secondary electron image (#2717).

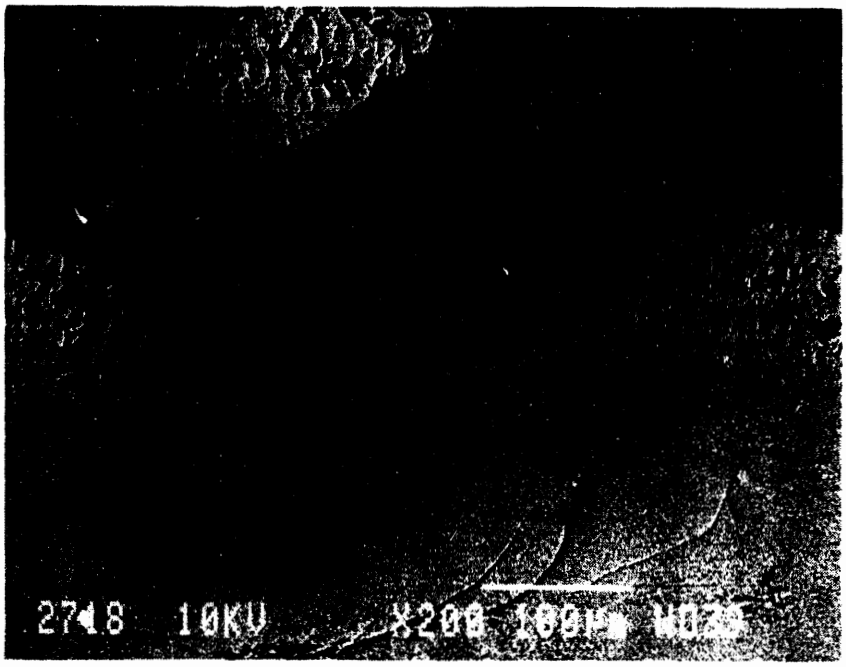

Figure A-81. Sample 1-9-B ROI #1 topographical (#2718).

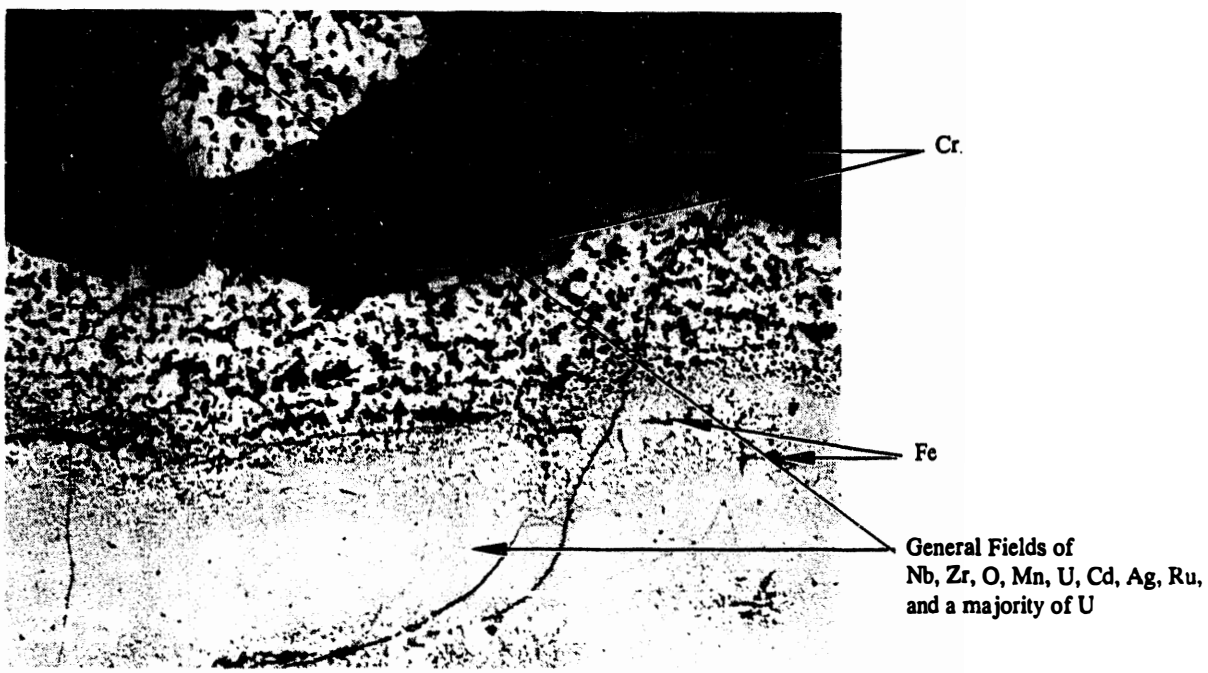

Figure A-82. Sample 1-9-B ROI #1 compositional (#2719).

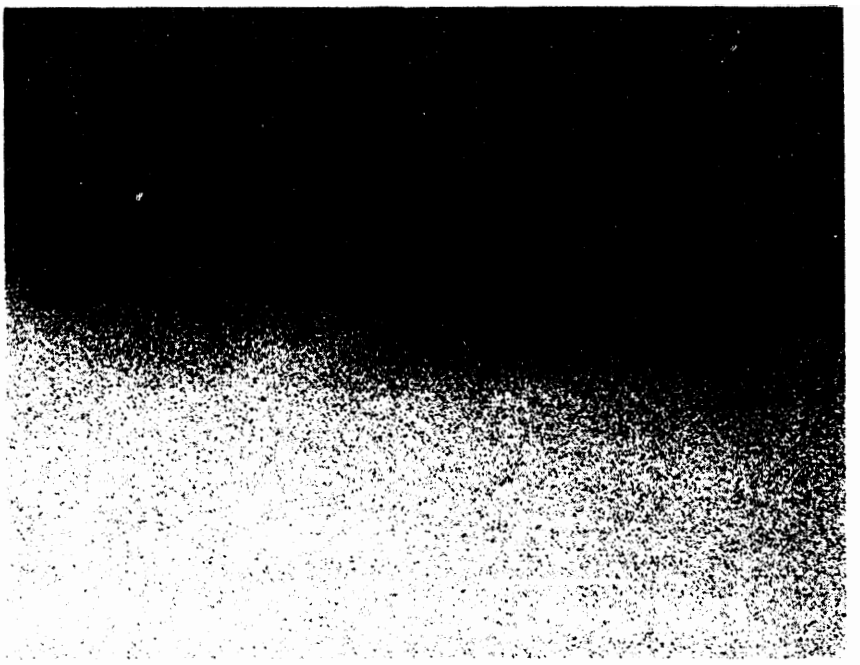

Figure A-83. Sample 1-9-B ROI #1 dot map of U (#2734).

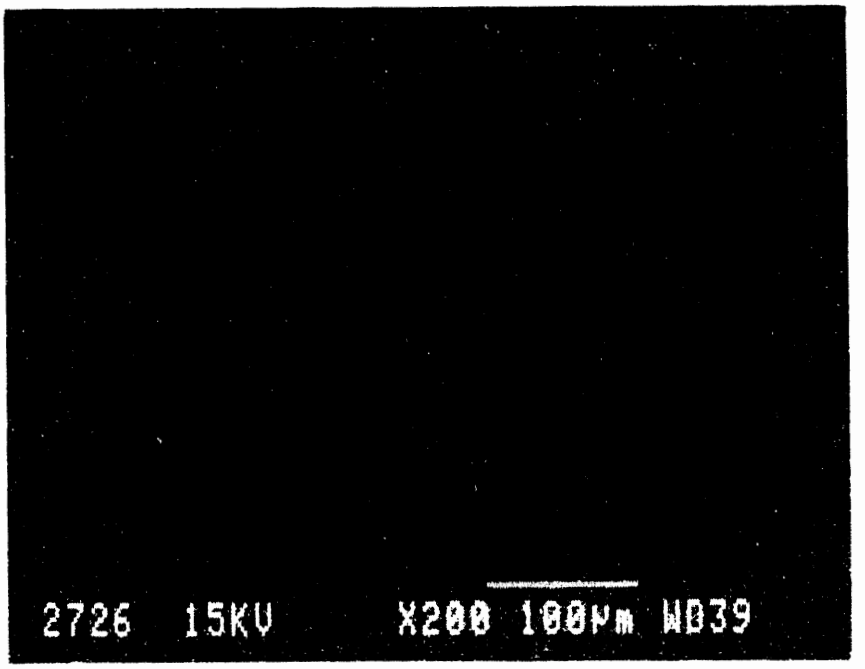

Figure A-84. Sample 1-9-B ROI #1 dot map of O (#2726).

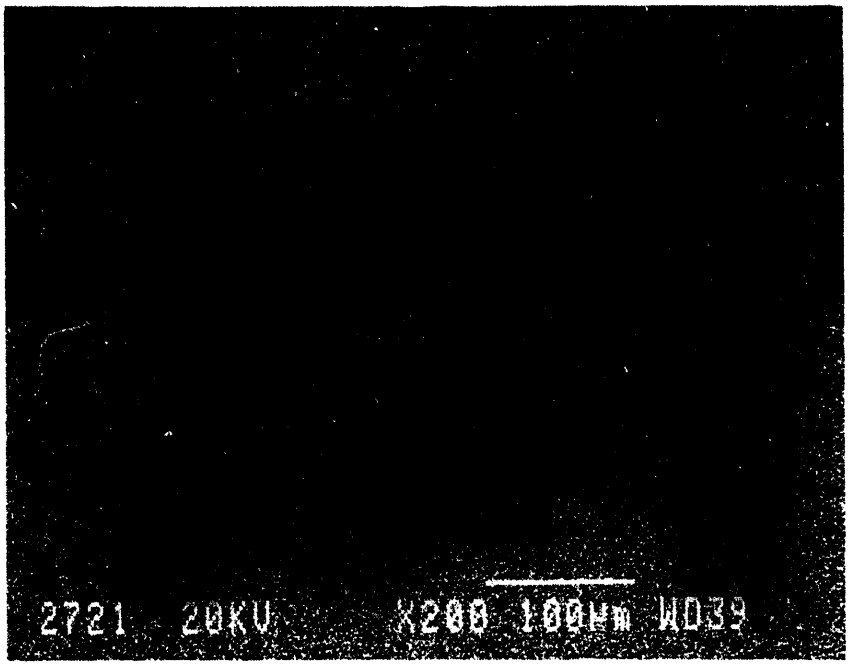

Figure A-85. Sample 1-9-B ROI #1 dot map of Zr (#2721).

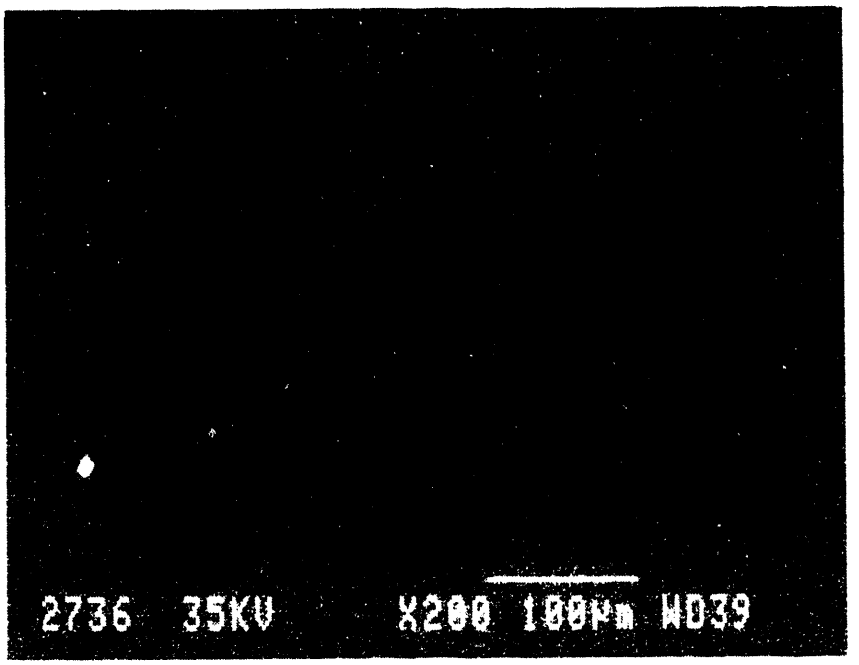

Figure A-86. Sample 1-9-B ROI #1 dot map of Ag (#2736).

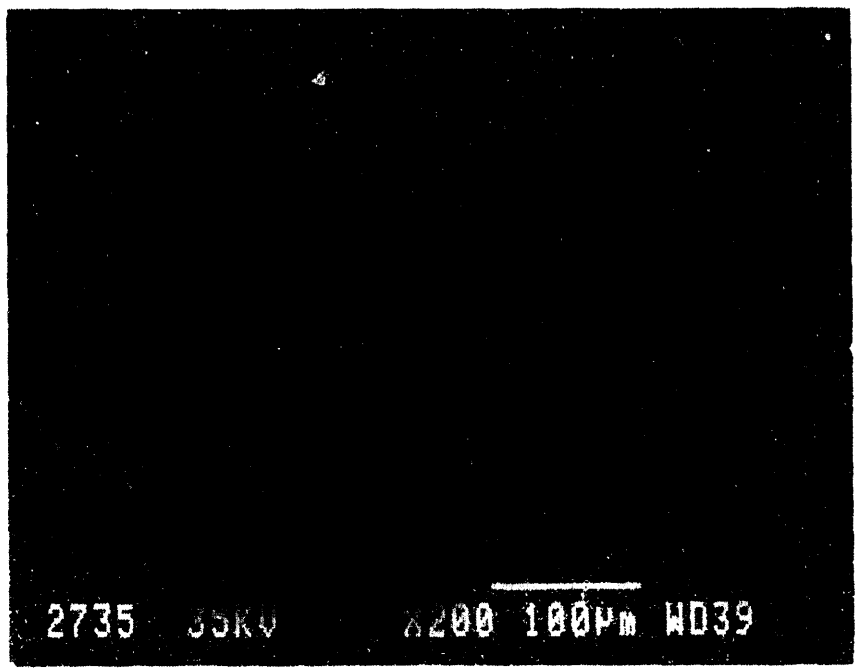

Figure A-87. Sample 1-9-B ROI #1 dot map of Cd (#2735).

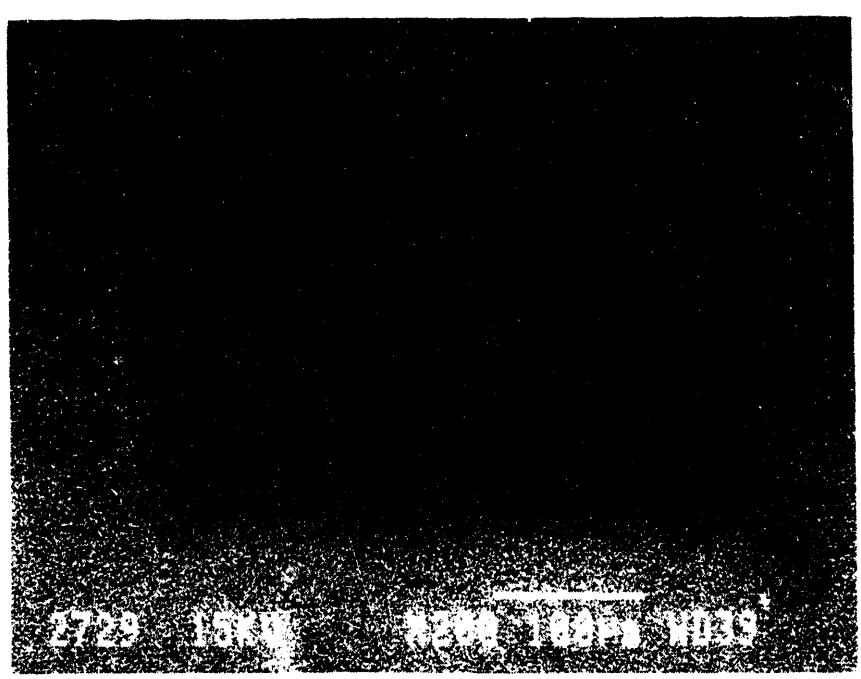

Figure A-88. Sample 1-9-B ROI #1 dot map of Cr (#2729).

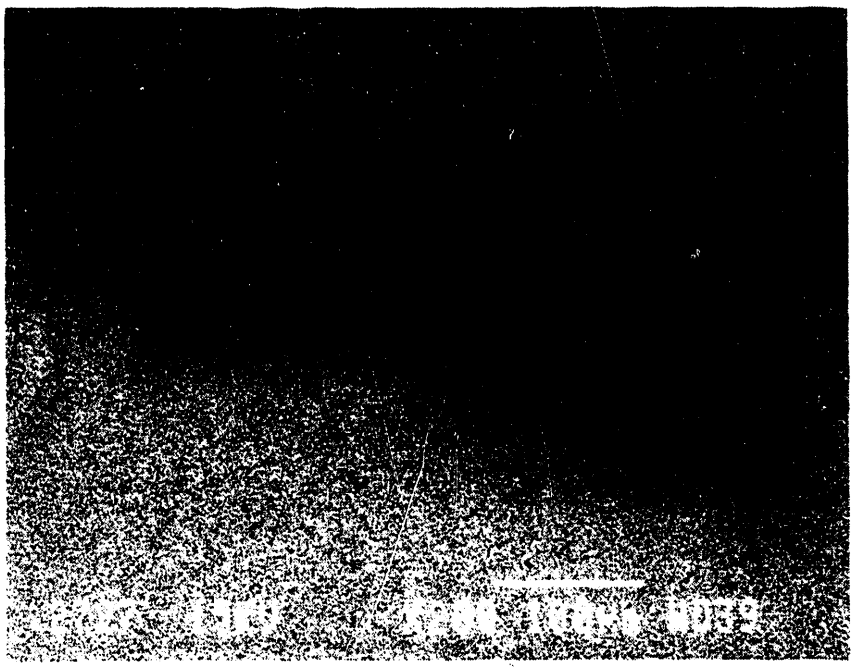

Figure A-89. Sample 1-9-B ROI #1 dot map of Fe (#2727).

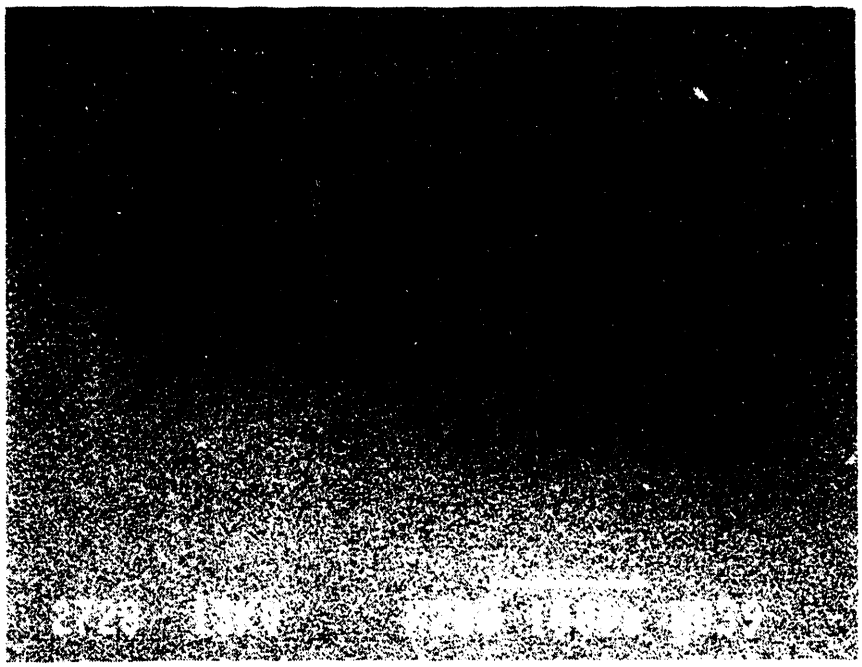

Figure A-90. Sample 1-9-B ROI #1 dot map of Mn (#2728).

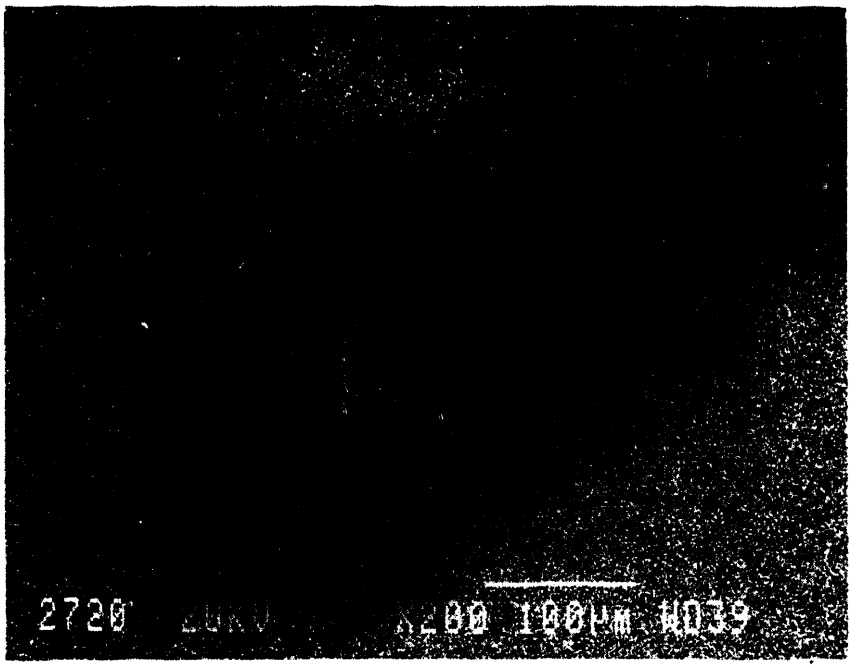

Figure A-91. Sample 1-9-B ROI #1 dot map of Nb (#2720).

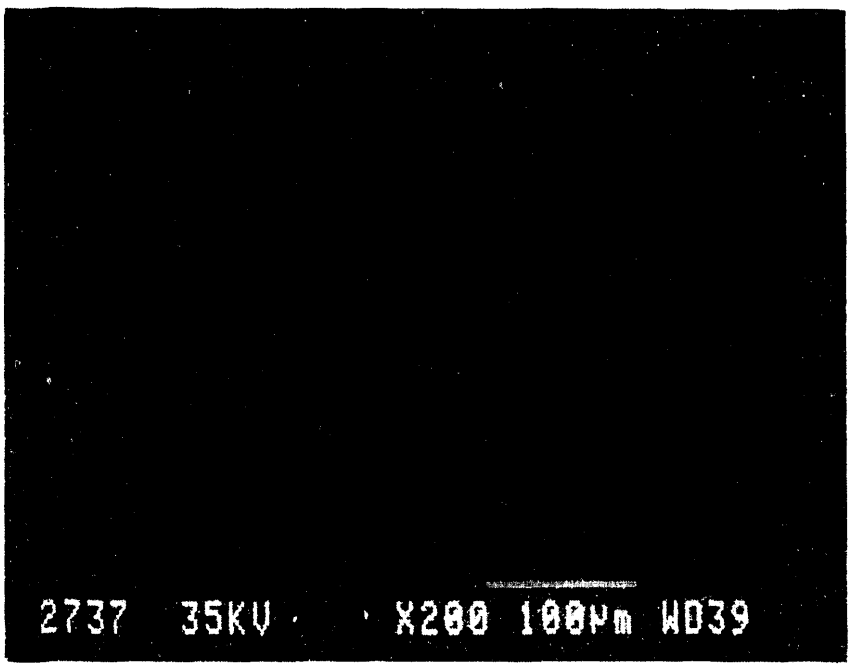

Figure A-92. Sample 1-9-B ROI #1 dot map of Ru (#2737).

Appendix B

Results from the Radiochemical Analysis of Samples

Table B-1. Average elemental concentration for each fractional companion sample (wt%).

Core Component/Element	Southeast Quadrant 1-9-A	Southeast Quadrant 1-9-B	Northwest Quadrant 1-11-A	Northwest Quadrant 1-11-B	Northwest Quadrant 1-11-C	Northeast Quadrant 1-12-A	Northeast Quadrant 1-12-C	Northeast Quadrant 1-12-D
Fuel								
U	7.32 E+01	7.14 E+01	6.51 E+01	7.32 E+01	7.42 E+01	7.36 E+01	6.66 E+01	6.44 E+01
Zr	1.43 E+01	1.40 E+01	1.10 E+01	1.30 E+01	1.31 E+01	1.39 E+01	1.64 E+01	1.53 E+01
Sn	--a	--a	--a	--a	--a	--a	--a	--a
Control Rod								
Ag	--a	--a	--a	--a	--a	--a	--a	--a
In	2.83 E-01b	--a	1.78 E-01b	--a	3.48 E-01b	--a	--a	--a
Cd	--a	--a	2.9 E-02b	--a	--a	8.1 E-02b	1.56 E-01b	1.57 E-01b
Burnable Poison Rod								
Al	--a	--a	--a	--a	--a	--a	--a	--a
B	--d	--d	--d	--d	--d	--d	--d	--d
Gd	--d	--d	--d	--d	--d	--d	--d	--d
Structural Material								
Cu	--d	--d	--d	--d	--d	--d	--d	--d
Cr	3.29 E-01c	3.25 E-01c	2.16 E-01c	3.48 E-01c	2.16 E-01c	4.64 E-01c	9.25 E-01c	1.84 E-01c
Fe	7.51 E-01	7.23 E-01	4.44 E-01	7.39 E-01	4.20 E-01	5.62 E-01	1.22 E+00	1.02 E+00
Mg	--a	--a	--a	--a	--a	--a	--a	--a
Mn	3.4 E-02b	2.7 E-02b	2.4 E-02b	3.1 E-02b	2.2 E-02b	2.2 E-02b	3.5 E-02b	--a
Mo	--a	--a	--a	--a	--a	--a	--a	--a
Nb	--a	--a	--a	--a	--a	--a	--a	--a
Ni	1.05 E-01b	9.4 E-02b	5.9 E-02b	1.07 E-01b	7.8 E-02b	8.1 E-02b	1.18 E-01b	1.13 E-01b
Si	--d	--d	--d	--d	--d	--d	--d	--d
Total wt% Of Sample	89.0	86.6	77.0	87.4	88.4	88.7	85.5	81.2

a. Below detectable concentrations.

b. The concentration is below the minimum reporting limit, but above the instrument detection limit.

c. Interelement interference correction factors were applied to compensate for uranium spectral interferences.

d. No analyses were performed for these elements.

Table B-2. TMI-2 companion sample gamma-scans of dissolution liquids.

SAMPLE ID#	RADIONUCLIDE ACTIVITY IN uCi/g +/- 1 STANDARD DEVIATION							
	27Co-57		27Co-60		51Sb-125		55Cs-134	
1-9-A	ND	+/- 0.000E+00	6.719E+00	+/- 1.189E-01	ND	+/- 0.000E+00	4.393E+00	+/- 1.902E-01
1-9-B	ND	+/- 0.000E+00	5.626E+00	+/- 1.285E-01	4.250E+00	+/- 6.792E-01	1.120E+01	+/- 2.643E-01
1-11-A	ND	+/- 0.000E+00	3.859E+00	+/- 8.104E-02	ND	+/- 0.000E+00	1.778E+00	+/- 1.789E-01
1-11-B	2.267E+03	+/- 5.305E+01	6.839E+00	+/- 7.660E-02	3.144E+00	+/- 2.572E-01	2.717E+00	+/- 1.269E-01
1-11-C	ND	+/- 0.000E+00	3.891E+00	+/- 8.249E-02	ND	+/- 0.000E+00	2.826E+00	+/- 1.648E-01
1-12-A	2.179E+03	+/- 2.876E+01	4.907E+00	+/- 1.394E-01	ND	+/- 0.000E+00	2.523E+01	+/- 5.601E-01
1-12-C	ND	+/- 0.000E+00	9.786E+00	+/- 1.419E-01	1.297E+01	+/- 1.314E+00	4.488E+01	+/- 5.565E-01
1-12-D	ND	+/- 0.000E+00	9.286E+00	+/- 1.913E-01	1.190E+01	+/- 2.667E+00	4.072E+01	+/- 5.538E-01
BLANK 1	ND	+/- 0.000E+00	ND	+/- 0.000E+00	ND	+/- 0.000E+00	ND	+/- 0.000E+00

SAMPLE ID#	RADIONUCLIDE ACTIVITY IN uCi/g +/- 1 STANDARD DEVIATION							
	55Cs-137		58Ce-144		63Eu-154		63Eu-155	
1-9-A	1.567E+02	+/- 5.798E-01	3.879E+02	+/- 3.611E+01	4.815E+01	+/- 3.082E-01	6.917E+01	+/- 6.433E-01
1-9-B	3.512E+02	+/- 3.091E+00	4.231E+02	+/- 4.299E+01	4.816E+01	+/- 3.660E-01	7.037E+01	+/- 1.766E+00
1-11-A	6.995E+01	+/- 2.728E-01	3.155E+02	+/- 2.619E+01	4.155E+01	+/- 2.867E-01	6.213E+01	+/- 1.292E+00
1-11-B	9.583E+01	+/- 4.408E-01	4.159E+02	+/- 2.886E+01	4.965E+01	+/- 2.135E-01	7.175E+01	+/- 1.557E+00
1-11-C	1.057E+02	+/- 7.716E-01	3.921E+02	+/- 2.670E+01	5.187E+01	+/- 2.749E-01	7.594E+01	+/- 1.002E+00
1-12-A	8.453E+02	+/- 6.340E+00	4.421E+02	+/- 8.873E+01	4.692E+01	+/- 5.302E-01	6.453E+01	+/- 9.486E-01
1-12-C	1.416E+03	+/- 8.921E+00	ND	+/- 0.000E+00	4.172E+01	+/- 3.421E-01	5.426E+01	+/- 1.183E+00
1-12-D	1.292E+03	+/- 6.589E+00	ND	+/- 0.000E+00	4.223E+01	+/- 3.927E-01	5.917E+01	+/- 6.805E-01
BLANK 1	ND	+/- 0.000E+00	ND	+/- 0.000E+00	ND	+/- 0.000E+00	ND	+/- 0.000E+00

Table B-3. TMI-2 companion sample strontium-90 analysis results of dissolution liquids.

SAMPLE ID#	LAB ID#	ACTIVITY +/- 1 STANDARD DEVIATION
1-9-A	T5	(3.22 +/- 0.18) E+03 uCi/g
1-9-B	T6	(2.57 +/- 0.15) E+03 uCi/g
1-11-A	T1	(2.29 +/- 0.13) E+03 uCi/g
1-11-A	T1R	(2.28 +/- 0.13) E+03 uCi/g
1-11-B	T4	(4.0 +/- 0.2) E+03 uCi/g
1-11-B	T4R	(3.9 +/- 0.2) E+03 uCi/g
1-11-C	T7	(2.07 +/- 0.13) E+03 uCi/g
1-12-A	T2	(5.9 +/- 0.3) E+03 uCi/g
1-12-C	T8	(1.89 +/- 0.11) E+03 uCi/g
1-12-D	T3	(8.4 +/- 0.5) E+03 uCi/g

CONTROL STD.	MEASURED ACTIVITY (D/S/G)	KNOWN ACTIVITY (D/S/G)	% RATIO
DAILY STD. 111	84.4	84.2	100.2%
DAILY STD. 115	80.5	84.2	95.6%
CHEMICAL STD.	81.6	84.2	96.9%

Table B-4. TMI-2 companion sample elemental analysis of dissolution liquids.

	URANIUM (U) (mg/g)	ZIRCONIUM (Zr) (mg/g)	ALUMINUM (Al) (microg/g)	CADMIUM (Cd) (microg/g)	CHROMIUM (Cr) (microg/g)
1-9-A	7.318E+02 +/- 9.147E-01	1.431E+02 +/- 1.789E-01	<8.161E+03 +/- 2.693E+01	<1.904E+02 +/- 6.284E-01	3.292E+03 +/- 1.086E+01
1-9-B	7.145E+02 +/- 8.931E-01	1.400E+02 +/- 1.750E-01	<1.246E+04 +/- 4.112E+01	<2.908E+02 +/- 9.595E-01	3.252E+03 +/- 1.073E+01
1-11-A	6.511E+02 +/- 8.138E-01	1.098E+02 +/- 1.373E-01	<4.596E+03 +/- 1.517E+01	2.880E+01 +/- 9.504E-02	2.160E+03 +/- 7.128E+00
1-11-B	7.324E+02 +/- 9.156E-01	1.297E+02 +/- 1.621E-01	<6.998E+03 +/- 2.309E+01	<1.633E+02 +/- 5.388E-01	3.476E+03 +/- 1.147E+01
1-11-C	7.419E+02 +/- 9.274E-01	1.313E+02 +/- 1.641E-01	<9.848E+03 +/- 3.250E+01	<2.298E+02 +/- 7.583E-01	2.163E+03 +/- 7.139E+00
1-12-A	7.364E+02 +/- 9.205E-01	1.392E+02 +/- 1.740E-01	<1.339E+04 +/- 4.418E+01	8.122E+01 +/- 2.680E-01	4.641E+03 +/- 1.532E+01
1-12-C	6.661E+02 +/- 8.326E-01	1.643E+02 +/- 2.053E-01	<1.940E+04 +/- 6.402E+01	1.565E+02 +/- 5.165E-01	9.248E+03 +/- 3.052E+01
1-12-D	6.444E+02 +/- 8.055E-01	1.535E+02 +/- 1.919E-01	<2.678E+04 +/- 8.836E+01	1.571E+02 +/- 5.184E-01	1.839E+03 +/- 6.068E+00
BLANK 1	<1.890E+01 +/- 2.363E-02	<1.350E+00 +/- 1.688E-03	<1.620E+03 +/- 5.346E+00	8.208E+00 +/- 2.709E-02	<1.080E+02 +/- 3.564E-01
CFA BLANK	<1.890E+01 +/- 2.363E-02	<1.350E+00 +/- 1.688E-03	<1.620E+03 +/- 5.346E+00	<3.780E+01 +/- 1.247E-01	<1.080E+02 +/- 3.564E-01

	INDIUM (In) (microg/g)	IRON (Fe) (microg/g)	MANGANESE (Mn) (microg/g)	MAGNESIUM (Mg) (microg/g)	MOLYBDENUM (Mo) (microg/g)
1-9-A	2.829E+03 +/- 9.336E+00	7.508E+03 +/- 2.478E+01	3.401E+02 +/- 1.122E+00	<3.401E+04 +/- 1.122E+02	<2.720E+03 +/- 8.977E+00
1-9-B	<1.765E+04 +/- 5.826E+01	7.228E+03 +/- 2.385E+01	2.708E+02 +/- 8.937E-01	<5.192E+04 +/- 1.713E+02	<4.154E+03 +/- 1.371E+01
1-11-A	1.777E+03 +/- 5.864E+00	4.443E+03 +/- 1.466E+01	2.359E+02 +/- 7.785E-01	<1.915E+04 +/- 6.319E+01	<1.532E+03 +/- 5.055E+00
1-11-B	<9.914E+03 +/- 3.271E+01	7.394E+03 +/- 2.440E+01	3.056E+02 +/- 1.008E+00	<2.916E+04 +/- 9.622E+01	<2.333E+03 +/- 7.698E+00
1-11-C	3.480E+03 +/- 1.148E+01	4.202E+03 +/- 1.387E+01	2.180E+02 +/- 7.193E-01	<4.103E+04 +/- 1.354E+02	<3.283E+03 +/- 1.083E+01
1-12-A	<1.897E+04 +/- 6.259E+01	5.623E+03 +/- 1.856E+01	2.191E+02 +/- 7.231E-01	<5.579E+04 +/- 1.841E+02	<4.463E+03 +/- 1.473E+01
1-12-C	<2.749E+04 +/- 9.070E+01	1.222E+04 +/- 4.034E+01	3.505E+02 +/- 1.157E+00	<8.084E+04 +/- 2.668E+02	<6.467E+03 +/- 2.134E+01
1-12-D	<3.793E+04 +/- 1.252E+02	1.018E+04 +/- 3.358E+01	<1.339E+03 +/- 4.418E+00	<1.116E+05 +/- 3.682E+02	<8.926E+03 +/- 2.945E+01
BLANK 1	<2.295E+03 +/- 7.574E+00	2.106E+02 +/- 6.950E-01	<8.100E+01 +/- 2.673E-01	<6.750E+03 +/- 2.228E+01	<5.400E+02 +/- 1.782E+00
CFA BLANK	<2.295E+03 +/- 7.574E+00	<6.750E+02 +/- 2.228E+00	<8.100E+01 +/- 2.673E-01	<6.750E+03 +/- 2.228E+01	<5.400E+02 +/- 1.782E+00

	NICKEL (Ni) (microg/g)	NIOBIUM (Nb) (microg/g)	SILVER (Ag) (microg/g)	TIN (Sn) (microg/g)
1-9-A	1.053E+03 +/- 3.474E+00	<3.401E+03 +/- 1.122E+01	<8.161E+02 +/- 2.693E+00	<2.176E+04 +/- 7.182E+01
1-9-B	9.388E+02 +/- 3.098E+00	<5.192E+03 +/- 1.713E+01	<1.246E+03 +/- 4.112E+00	<3.323E+04 +/- 1.097E+02
1-11-A	5.913E+02 +/- 1.951E+00	<1.915E+03 +/- 6.319E+00	<4.596E+02 +/- 1.517E+00	<1.226E+04 +/- 4.044E+01
1-11-B	1.071E+03 +/- 3.533E+00	<2.916E+03 +/- 9.622E+00	<6.998E+02 +/- 2.309E+00	<1.866E+04 +/- 6.158E+01
1-11-C	7.813E+02 +/- 2.578E+00	<4.103E+03 +/- 1.354E+01	<9.848E+02 +/- 3.250E+00	<2.626E+04 +/- 8.666E+01
1-12-A	8.078E+02 +/- 2.666E+00	<5.579E+03 +/- 1.841E+01	<1.339E+03 +/- 4.418E+00	<3.570E+04 +/- 1.178E+02
1-12-C	1.183E+03 +/- 3.905E+00	<8.084E+03 +/- 2.668E+01	<1.940E+03 +/- 6.402E+00	<5.174E+04 +/- 1.707E+02
1-12-D	1.134E+03 +/- 3.741E+00	<1.116E+04 +/- 3.682E+01	<2.678E+03 +/- 8.836E+00	<7.140E+04 +/- 2.356E+02
BLANK 1	<3.240E+02 +/- 1.069E+00	<6.750E+02 +/- 2.228E+00	<1.620E+02 +/- 5.346E-01	<4.320E+03 +/- 1.426E+01
CFA BLANK	<3.240E+02 +/- 1.069E+00	<6.750E+02 +/- 2.228E+00	<1.620E+02 +/- 5.346E-01	<4.320E+03 +/- 1.426E+01

Appendix C

TMI-2 Decay Heat at Short Times After the Accident

Appendix C

TMI-2 Decay Heat at Short Times After the Accident

Date: April 17, 1992

To: D. W. Akers

From: E. H. Ottewitte, MS 2114

Subject: TMI-2 DECAY HEAT AT SHORT TIMES AFTER THE ACCIDENT - EHO-07-92

Reference:

(a) B. G. Schnitzler and J. B. Briggs, TMI-2 Isotopic Inventory Calculations, EGG-PBS-6798 (no date given).

(b) E. Browne and R. B. Firestone, Table of Radioactive Isotopes, John Wiley, New York, 1986, pp. D-10 - D-26.

(c) T. R. England and W. B. Wilson, TMI-2 Decay Power: LASL Fission Product and Actinide Decay Power Calculations for the President's Commission at Three Mile Island, LA-8041-MS, October 1979.

Per your request I have calculated the subject information at times of 224 and 600 minutes after shutdown from the accident. The basis of this work was the reference (a) calculation of the core-averaged isotopic inventory (in moles) at shutdown, minus the contributions from highly-volatile noble gases, I and Cs.

The reference (a) values were first placed into Word Perfect format with the help of an optical scanner. For each isotope we then added half-lives and the average energy release by decay mode from reference (b). These 4000-5000 entries were then manually checked, followed by pattern checks for inconsistencies.

A final physics check judged which missing data were important. For four isotopes it was necessary to evaluate their decay-energy release ad hoc. Table 1 tabulates these values. Attachment A presents the resulting set in Word Perfect format.

Table 1. Ad hoc evaluated data for pertinent isotopes

Isotope	$t_{½}$	Moles	$\langle E_\gamma \rangle$(MeV)	$\langle E_\beta \rangle$(MeV)
^{112}Pd	21.04h	0.011	0.0185	0.11
^{141}La	3.9h	0.16	0.03	1.0
^{156}Sm	9.4h	0.0027	0.06	0.3
^{157}Eu	15h	0.003	0.4	0.3

The next step was to transfer the Word Perfect files into a LOTUS 1-2-3 spreadsheet. Here the inventories were adjusted for the two decay times and multiplied by appropriate conversion factors as follows:

$$[\text{moles}] \times [6.02\times10^{13} \text{ atoms/mole}] \times [1.602\times10^{-13} \text{ Ws/MeV}] \times [\lambda \text{ dis/atom s}]$$

$$\times [\text{MeV/dis}] / [8.16\times10^{7} \text{ g U}]$$

where

λ = decay constant for each isotope

8.16×10^{7} g U = the mass associated with 7673 moles ^{235}U, 335,100 Moles ^{238}U, and 216 moles ^{236}U

MeV/dis = the isotopic decay heat values obtained from reference (b).

The total results of the 1-2-3 calculations are rather voluminous. They include the breakdown in heating by gamma (non-local) release as well as by local deposition. Table 2 summarizes the contributions from all isotopes. The total result of 0.16 at 10 hours after shutdown compares favorably with a value of 0.21 watts per gram U calculated at LANL (c) with the CINDER code.

To remove the contributions from volatiles, Attachment B compiles the percentage contribution of each isotope to one decimal place for easier viewing. Table 3 tabulates the pertinent results and calculates the non-volatile percentages to be 80.3 and 85.6 at 224 minutes and 10 hours after shutdown, respectively.

Table 2. Summary results of 1-2-3 calculations

Decay Mode	Post Shutdown Heating Rate (W/g U)	
	after 224 minutes	after 10 hours
non-local gamma release	0.12	0.083
local release	0.11	0.079
total	0.23	0.16
non-volatile total	0.18	0.14

Table 3. Volatile isotope contributions to the total decay heat

Category	Isotope	% at 224 min	% at 10 hours
Actinides	Np-239	19.2	25.3
	Total Actinides	19.2	25.3
Volatile FP	Kr-85m	0.2	0.1
	Kr-87	0.4	0.
	Kr-88	2.1	0.6
	I-131	1.2	1.7
	I-132	2.9	0.6
	I-133	4.3	4.9
	Xe-133	0.8	1.2
	I-134	0.9	
	I-135	6.1	4.5
	Xe-135	0.4	0.4
	Cs-136	0.	0.1
	Cs-138	0.1	0.
	Total Vol. FP	19.4	14.1
Other FP	Sr-89	1.1	1.6
	Sr-91	4.7	4.3
	Y-91	1.4	1.9
	Y-91m	0.1	
	Sr-92	2.2	0.6
	Y-92	3.1	1.3
	Y-93	4.0	3.8
	Zr-95	2.1	3.0
	Nb-95	1.3	1.9
	Zr-97	5.5	6.1
	Nb-97	0.5	
	Nb-98m	0.7	
	Mo-99	2.8	3.7
	Tc-99m	0.3	0.2
	Ru-103	1.1	1.6
	Ru-105	0.9	0.5
	Rh-105	0.3	0.3
	Pd-109	0.1	0.1
	Sn-127	0.1	
	Sb-127	0.2	0.2
	Sb-128	0.1	0.1
	Tc-131m	0.4	0.5
	Tc-132	1.0	1.4
	Tc-133m	0.3	0.
	Tc-134	0.1	
	Ba-139	0.7	

	Ba-140	1.9	2.7
	La-140	10.6	13.5
	La-141	2.2	1.0
	Ce-141	0.8	1.1
	La-142	2.5	0.2
	Ce-143	2.6	3.2
	Pr-143	1.1	1.6
	Se-144	0.1	0.1
	Pr-145	1.2	0.8
	Nd-147	0.6	0.9
	Pm-148	0.2	0.3
	Nd-149	0.2	
	Pm-149	0.3	0.4
	Pm-151	0.2	0.3
	Sm-153	0.1	0.1
	Eu-156	0.1	0.
	Total Other FP	59.8	59.3
Grand Total		98.4	98.7
Normalized Non-Volatile%		80.3	85.7

Attachments:
As Stated

cc: Central Files, MS 3108
E. H. Ottewitte File

END

DATE
FILMED
5/9/94